COLD IONS OF IONOSPHERIC ORIGIN OBSERVED AT THE DAYSIDE MAGNETOPAUSE AND THEIR EFFECTS ON MAGNETIC RECONNECTION

By

Sun-Hee Lee

RECOMMENDED:

Dr. Qiu-Gang Zong

Dr. Antonius Otto

Dr. Chung-Sang Ng

Dr. Hui Zhang
Advisory Committee Chair

Dr. Curt Szuberla
Chair, Department of Physics

APPROVED:

Dr. Paul Layer
Dean, College of Natural Science and Mathematics

Dr. John Eichelberger
Dean of the Graduate School

14 July 2015
Date

COLD IONS OF IONOSPHERIC ORIGIN OBSERVED AT THE DAYSIDE MAGNETOPAUSE AND THEIR EFFECTS ON MAGNETIC RECONNECTION

A

DISSERTATION

Presented to the Faculty

of the University of Alaska Fairbanks

in Partial Fulfillment of the Requirements

for the Degree of

DOCTOR OF PHILOSOPHY

By

Sun-Hee Lee, B.S., M.S.

Fairbanks, Alaska

August 2015

Abstract

Magnetic reconnection at the dayside magnetopause is one of the most important mechanisms that efficiently transfers solar wind particles, momentum, and energy into the magnetosphere. Magnetic reconnection at the magnetopause is usually asymmetric since the plasma and magnetic field properties are quite different in the magnetosphere and the magnetosheath. Cold dense plasma, originating either directly from the ionosphere or from the plasmasphere, has often been observed at the adjacent magnetopause. These cold plasmas may affect reconnection since they modify the plasma properties on the magnetospheric side significantly.

This dissertation presents case and statistical studies of the characteristics of the cold ions observed at the dayside magnetopause by using Cluster spacecraft datasets. The plasmaspheric plumes have been distinguished from the ionospheric outflows using ion pitch angle distributions. The ionospheric outflows feature unidirectional or bidirectional field-aligned pitch angle distributions, whereas the plasmaspheric plumes are characterized by 90° pitch angle distributions. The occurrence rates of the plasmaspheric plumes and ionospheric outflows and their dependence on the solar wind/Interplanetary Magnetic Field (IMF) conditions have been investigated. It is found that the occurrence rate of plasmaspheric plume or ionospheric plasma strongly depends on the solar wind/IMF conditions. In particular, plasmaspheric plumes tend to occur during southward IMF while ionospheric outflows tends to occur during northward IMF. The occurrence rate of the plasmaspheric plumes is significantly higher on the duskside than that on the dawnside, indicating that the plasmaspheric plumes may lead to a dawn-dusk asymmetry of dayside reconnection.

Furthermore, this dissertation investigates the behavior of the cold dense plasma of ionospheric origin during magnetic reconnection at the dayside magnetopause. The motion of cold plasmaspheric ions entering the reconnection region differs from that of warmer magnetosheath and magnetospheric ions. In contrast to the warmer ions, which are probably accelerated by reconnection near the subsolar magnetopause, the colder ions are simply entrained by $\mathbf{E}\times\mathbf{B}$ drift at high latitudes on the recently reconnected magnetic field lines. This indicates that plasmaspheric ions can sometimes play a very limited role in magnetic reconnection process.

Finally, this dissertation examines a controlling factor that leads to the asymmetric reconnection geometry at the magnetopause. It is demonstrated that the separatrix and flow boundary angles are greater on the magnetosheath side than on the magnetospheric side of the magnetopause, probably due to the stronger density asymmetry rather than magnetic field asymmetry at this boundary.

Table of Contents

List of Figures

Page

List of Tables

Page

Acknowledgements

I would like to deeply thank to my advisor, Professor Zhang Hui. When I came to the Physics department at the University of Alaska Fairbanks as a Ph.D. student, I did not have any background in space physics. Dr. Zhang accepted me as her student and introduced me to the field. I could not have finished my Ph.D. study without her advice, care, and patience. She taught me how to write research papers, theses, responses to the reviewers' comments, and proposals. She encouraged me to attend many conferences and gave me chances to present my research results. Her constant support and guidance encouraged the completion of this thesis. I cannot thank her enough. I am sincerely proud to be her student.

In the preparation of this thesis, my committee members (Professor Qiu-Gang Zong, Professor Antonius Otto, and Professor Chung-Sang Ng) provided valuable comments and helpful suggestions for improving my thesis, as well as wrote reference letters for me to apply for post-doc positions. Many thanks to all. I would especially like to thank Dr. Zong for giving me helpful comments and his guidance on writing research papers and my thesis. My discussions with Dr. Zong have helped me to broaden my perspective and think more about the magnetosphere and ionosphere couplings. I also acknowledge the helpful suggestions and discussions on my research with Dr. David Sibeck.

I would like to thank my fellow students at the Geophysical Institute. Many thanks to all for their help, support, and friendship, with special mention of Min-shiu Hsieh, Christina Chu, Xuanye Ma, Mattew Copper, and Douglas Ogata. My life on the 7th floor at the Geophysical Institute would be boring without them. They made me happy and laugh, helping me forget my stresses and worries of studying when I talked with them.

I would like to thank people from the First Korean Presbyterian Church of Fairbanks, Pastors Joo-Hoon Kim and Woo-Sung Jeong, Pastors' wives, Elder Jin-Hee Lee, Elder Eun-Hee Choi, Elder and Deacon Chi, Deacon Soo-Ji Go, friends Sooyoun Chi, Kyungyoun Chi, Haewon Yang, Sang-Ho Lee, Dr. Taesun Kim, and Professor Yong-Won Kim, who pray for me, comfort and support me. They are my family in Christ. They helped make Fairbanks my home. Their prayer supported my studies and encouraged me to complete my Ph.D. study.

I would like to thank my Korean scientists Dr. Kyung-Joo Hwang, Dr. Eunhwa Kim, and Dr. Hyomin Kim, whom I met at the conferences. Thanks to all for sharing their researcher's life and encouraging me to keep studying and to have a courage to apply to post-doc positions, especially, Dr. Hwang, who helped me apply to the postdoctoral fellowship and encouraged me when I felt like a failure.

I would like to thank my family, my mother Sun-Ok Kim, my sister Seon-Young Lee, brother-in-law Hyeok-Jin Geon, Elder Jonghan Choi, Senior Deacon Sarah Jeon, Hyeokmin Choe, his family

Chang-Soo Choi and Bok-Ja Kim, my relatives in South Korea, and JBF for their love, support, and prayer.

Chapter 1
Introduction to the Solar-Terrestrial Environments

1.1 Solar Wind and Interplanetary Magnetic Field

The Sun, which is located at the center of the solar system, is the primary source of energy for the Earth. It is the driver of the disturbances in the near-Earth space environment and the interplanetary space. The Sun is composed of 90% hydrogen (H), 10% helium (He), and 0.1% heavier elements (C, N, O) [*Kivelson and Russell*, 1995]. The hydrogen in the Sun is used as a fuel and converted to helium through nuclear fusion, which is the Sun's energy source. A huge amount of energy is generated from the Sun through this nuclear reaction and expelled into the interplanetary space.

The Sun radiates a continuous and high-speed flow of ionized gas, or plasma, known as the solar wind. This was suggested by *Biermann* [1951] based on the studies of comet tails. The solar wind consists mainly of electrons and protons with small amount of ionized helium and heavy ions. The near-Earth space environment is constantly influenced by the solar wind. The properties of the solar wind, such as speed and temperature, change as the solar wind flows in the interplanetary space.

The great pressure difference between the the Sun's corona and the interstellar space overcomes the Sun's gravity and drives the solar wind plasma outward. The fluid theory for the equilibrium state of the coronal plasma in the gravitational field of the Sun was used to understand solar wind formation. The fluid model starts with the equations for conservation of mass and momentum in a fluid, assuming that solar wind is a fully ionized plasma. The solar corona is assumed to be steady-state, spherically symmetric and isothermal. This model also ignores the magnetic effects [*Kivelson and Russell*, 1995]. *Parker* [1958] predicted the existence of the solar wind by considering solutions with non-zero flow speeds. He suggested that the solar wind is subsonic at the base of the corona and is then accelerated to supersonic speed at a critical point. The critical point (or sonic point) is located at around 4–6 solar radii. The flow speed increases up to 40 solar radii (0.2 AU) and becomes nearly constant at larger distances [*Cairns*, 1999].

The solar wind flows radially away from the Sun. The Sun rotates once approximately every 27 days. The solar wind source region is fixed on the rotating Sun. This rotation of the source region generates sequential arrows of solar wind, which is sketched in Figure 1.1(a). The succession of fluid flows radially in a different angular direction. There are two types of solar wind known as "slow" solar wind ($\approx$ 350 km/s) and "fast" solar wind ($\approx$ 650 km/s). Fast solar wind overtakes the slower wind and generates a co-rotating interaction region (also a magnetic scattering region) where the plasma is compressed, as shown in Figure 1.1(b).

Table 1.1. Observed (left) and derived (right) physical properties of the solar wind at 1 AU [*Kivelson and Russell*, 1995]

Proton density	6.6 cm^{-3}	Gas pressure ($p_{gas} = nk(T_p + T_e)$)	30 pPa (pico pascals)
Electron density	7.1 cm^{-3}	Magnetic pressure ($p_{mag} = B^2/2\mu_0$)	19 pPa
He^{2+}	0.25 cm^{-3}	Proton gyroradius	80 km
Flow speed	450 km/s	Proton-proton collision time	4×10^6 s
Proton temperature	1.2×10^5 K	Electron-proton collision time	3×10^5 s
Electron temperature	1.4×10^5 K	Time for wind to flow from corona to 1 AU	$\sim$4 days (3.5×10^5 s)
Magnetic field	7 nT (nano tesla)	Alfvén speed	$\sim$40 km/s

The solar magnetic field, which is called the interplanetary magnetic field (IMF), is carried along with the radial outflow of the solar wind. As a result of the superposition of the motion of outflow and rotation of the Sun, the magnetic field gets twisted and is forced into a spiral configuration. This spiral shape is known as the Parker Spiral. The magnetic field is directed outward from one of the Sun's magnetic dipole and inward in the other. The different field directions create a thin layer near the Sun's magnetic equatorial plane which is called the Heliospheric current sheet (the neutral current sheet). The Heliospheric current sheet becomes wavy as the Sun rotates (see Figure 1.1(c)). The Parker spiral is indicated by the yellow arrows in Figure 1.1(c). The magnetic field makes an angle of $\approx 45°$ to a line drawn from the Sun at one astronomical unit (1 AU, the distance from the Earth to the Sun) for a 400 km/s solar wind speed [*Kivelson and Russell*, 1995] (see Figure 1.1(d)). The Sun's magnetic field has several roles: It stores and releases the magnetic energy; it may exert a force and thus accelerate the plasma; and it may drive waves or instabilities. Variations in the IMF and the solar wind affect conditions in the near-Earth space environment and produce modulations in the geomagnetic activity. The orientation of the IMF is an important factor in the solar wind-magnetosphere coupling.

Table 1.1 shows the average properties of solar wind at 1 AU [*Kivelson and Russell*, 1995]. The number densities of the proton, electron, and helium (He^{2+}) are typically 6.6 cm^{-3}, 7.1 cm^{-3}, and 0.25 cm^{-3} at 1 AU, respectively. The average flow speed is about 450 km/s. The proton and electron temperature are about 1.2×10^5 K and 1.4×10^5 K. The embedded magnetic field varies but has an average value of 7 nT at 1 AU [*Kivelson and Russell*, 1995].

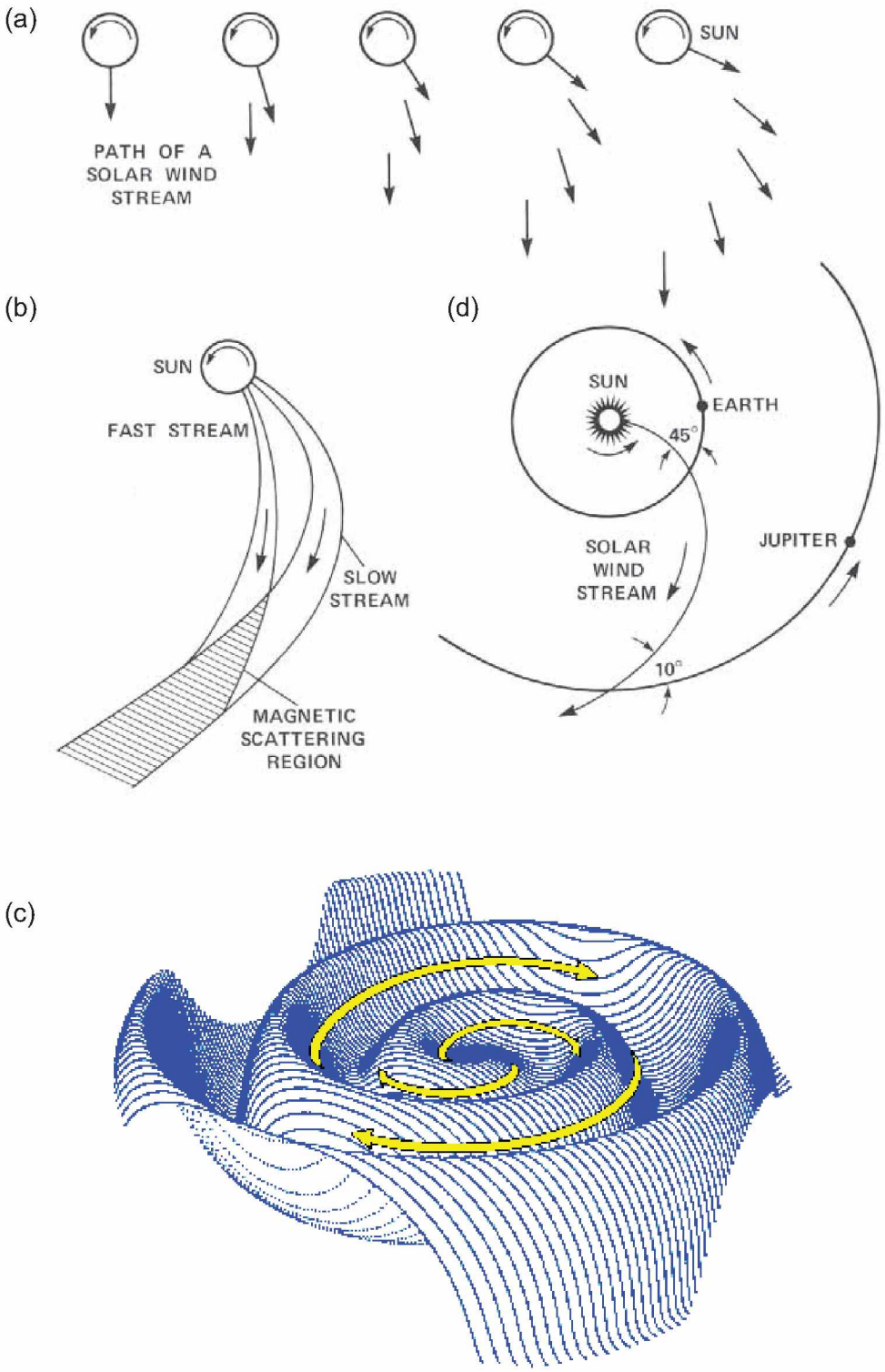

Figure 1.1. (a) A succession of the solar wind flow emitted at constant speed from the rotating Sun, (b) geometry of the interaction between fast solar wind and slower solar wind, (c) a graphic image of the Parker spiral (Image courtesy J. Jokipii, University of Arizona), (d) the IMF makes a 45° (80°) angle with the radial direction at the orbit of the Earth (Jupiter). (Figures 1.1(a), (b) and (d) are from http://history.nasa.gov/SP-349/p96.jpg)

1.2 MHD Discontinuities and Shocks

When the supersonic solar wind flow encounters a magnetized obstacle, such as the Earth, a bow shock and a magnetopause, which are thin boundaries separating adjacent regions, are formed. A large-scale plasma boundary can be defined by discontinuous macroscopic parameters (such as field, density, velocity, etc.) in space. The field and plasma parameters across the discontinuity satisfy certain conditions (called jump conditions) which can be derived using ideal magnetohydrodynamics (MHD) equations. MHD studies the dynamics of electrically conducting fluids in the presence of electromagnetic fields. The plasma is treated as a conducting fluid instead of individual particles. The plasma is assumed to be in thermal equilibrium therefore can be described by a Maxwellian distribution function. The ideal MHD equations can be written in the form of conservation of mass, momentum, and energy equations and Maxwell's equations.

Continuity equation:

$$\frac{\partial \rho}{\partial t} + \nabla \cdot (\rho \mathbf{u}) = 0 \tag{1.1}$$

Momentum equation:

$$\rho \frac{\partial \mathbf{u}}{\partial t} + \rho(\mathbf{u} \cdot \nabla)\mathbf{u} = -\nabla p - \nabla \left(\frac{B^2}{2\mu_0} \right) + (\mathbf{B} \cdot \nabla)\frac{\mathbf{B}}{\mu_0} \tag{1.2}$$

Energy equation:

$$\frac{\partial w_{total}}{\partial t} = -\nabla \cdot \left[\left(\frac{1}{2}\rho u^2 + \frac{\gamma p}{\gamma - 1} + \frac{1}{\mu_0} B^2 \right) \mathbf{u} - \frac{\mathbf{u} \cdot \mathbf{B}}{\mu_0} \mathbf{B} \right] \tag{1.3}$$

Maxwell's equations:

$$\frac{\partial B}{\partial t} = \nabla \times (\mathbf{u} \times \mathbf{B}) \tag{1.4}$$

$$\nabla \cdot \mathbf{B} = 0 \tag{1.5}$$

In these equations, ρ is the mass density, $\mathbf{u}$ is the bulk flow velocity, p is thermal pressure, $\mathbf{B}$ is the magnetic field vector, μ_0 is magnetic permeability of free space, γ is the specific heat ratio, and w_{total} is the total energy density, which can be written as

$$w_{total} = \frac{1}{2}\rho u^2 + \frac{p}{\gamma - 1} + \frac{1}{2\mu_0} B^2 \tag{1.6}$$

Assuming that a plasma flow is in steady-state which implies to be time invariant, all time derivatives are zero so that the set of ideal MHD equations becomes simpler, and can be rewritten as

Continuity equation:

$$\nabla \cdot (\rho \mathbf{u}) = 0 \tag{1.7}$$

Momentum equation:

$$\rho(\mathbf{u}\cdot\nabla)\mathbf{u}+\nabla p+\nabla\left(\frac{B^2}{2\mu_0}\right)+(\mathbf{B}\cdot\nabla)\frac{\mathbf{B}}{\mu_0}=0 \tag{1.8}$$

Energy equation:

$$\nabla\cdot\left[\left(\frac{1}{2}\rho u^2+\frac{\gamma p}{\gamma-1}+\frac{1}{\mu_0}B^2\right)\mathbf{u}-\frac{\mathbf{u}\cdot\mathbf{B}}{\mu_0}\mathbf{B}\right]=0 \tag{1.9}$$

Maxwell's equations:

$$\nabla\times(\mathbf{u}\times\mathbf{B})=0 \tag{1.10}$$

$$\nabla\cdot\mathbf{B}=0 \tag{1.11}$$

If the boundary is one-dimensional, i.e., there are variations only along the boundary normal direction (n-axis), then equations 1.7–1.11 can be rewritten as

Continuity equation:

$$[\rho u_n]=0 \tag{1.12}$$

Momentum equation:

$$\left[\rho u_n\mathbf{u}+\left(p+\frac{B^2}{2\mu_0}\right)\mathbf{n}-\frac{1}{\mu_0}B_n\mathbf{B}\right]=0 \tag{1.13}$$

Energy equation:

$$\left[\rho u_n\left(\frac{1}{2}u^2+\frac{\gamma}{\gamma-1}\frac{p}{\rho}\right)+u_n\frac{B^2}{\mu_0}-\mathbf{u}\cdot\mathbf{B}\frac{B_n}{\mu_0}\right]=0 \tag{1.14}$$

Maxwell's equations:

$$[u_n\mathbf{B}_t-B_n\mathbf{u}_t]=0 \tag{1.15}$$

$$[B_n]=0 \tag{1.16}$$

Where the notation [] is the difference between the values of the quantity on the two sides of the discontinuity, subscripts n and t indicate the normal and the tangential components, respectively [*Kivelson and Russell*, 1995]. These conversion relations are known as the Rankine-Hugoniot conditions (shock-jump conditions) that describe the relations between the upstream and downstream plasma parameters. The solutions of Rankine-Hugoniot relations provide the descriptions of a number of different types of MHD discontinuities and shocks.

Two specific parameters can be used to differentiate between different types of MHD discontinuities and shocks: the normal velocity component (u_n) and the density jump condition across the boundary (ρ). When $[u_n] = 0$, there is no flow of plasma across the discontinuity, and when $[\rho] = 0$, mass density is constant. This classification categorizes discontinuities and shocks into four groups: trivial discontinuity, rotational discontinuity, contact discontinuity, and MHD shocks, as shown in Table 1.2 [*Gurnett and Bhattacharjee*, 2005]. The tangential discontinuity occurs when

Table 1.2. Categorization of MHD discontinuities and shocks [*Gurnett and Bhattacharjee*, 2005]

	$u_n = 0$	$u_n \neq 0$
$[\rho] = 0$	Trivial	Rotational discontinuity
$[\rho] \neq 0$	Contact discontinuity	Shocks

Table 1.3. Possible Types of Discontinuities and Shocks in Ideal MHD [*Kivelson and Russell*, 1995]

Tangential discontinuity $u_n = 0$, $B_n = 0$	Flow and magnetic field are tangential to the boundary. Total pressure is the same on both sides.
Rotational discontinuity $u_n = B_n/(\mu_0\rho)^{\frac{1}{2}}$ (Walén relation)	Field and flow change their directions, but not magnitude (in isotropic plasma). u_n and B_n are not zero.
Contact discontinuity $u_n = 0$, $B_n \neq 0$	Flow is tangential to the boundary. The thermal pressure is continuous.
Shocks $u_n \neq 0$	There is a flow across the discontinuity. There is a density and temperature jump across the discontinuity.
Parallel shock $B_t = 0$	$\theta_{Bn} = 0°$, magnetic field does not change at shock.
Perpendicular shock $B_n = 0$	$\theta_{Bn} = 90°$ Plasma density and magnetic field strength increase.
Oblique shocks $B_t \neq 0$, $B_n \neq 0$	$0° < \theta_{Bn} < 90°$ **Fast shock**: Magnetic field strength and plasma pressure increase; magnetic field bends away from the shock normal. **Slow shock**: Magnetic field strength decreases; plasma pressure increases; magnetic field bends towards the shock normal.

$B_n = 0$ and $u_n = 0$, which is a special case of the contact discontinuity.

Shock waves are characterized by a non-zero flow and a density jump across the discontinuity. Shocks can be further classified by their local geometry using θ_{Bn}, which is the angle between the magnetic field and the shock normal upstream [*Kallenrode*, 2004]. The Earth's bow shock, other planetary bow shocks, and most traveling interplanetary shocks in the solar wind are fast shocks. Table 1.3 shows the classification of MHD discontinuities and shocks and their characteristics based on the behavior of the u_n and B_n.

1.3 Earth's Magnetosphere

The Earth's magnetosphere is shaped when the continuous flow of solar wind interacts with the Earth's dipolar magnetic field. The magnetized solar wind plasma sweeps around the Earth's magnetic field, forming a bullet shaped magnetic cavity. The shape of the Earth's magnetosphere is distorted and its size varies depending on the solar wind conditions. The solar wind exerts pressure on the dayside Earth's magnetosphere and stretches the magnetic field on the nightside,

forming the magnetotail. The Earth's magnetosphere contains the following key parts: the bow shock, magnetosheath, magnetopause, magnetotail, polar cusps, plasmasphere and radiation belts (see Figure 1.2). Some of them will be discussed in this section. The Earth's magnetosphere is filled with several large scale current systems (gray arrows) shown in Figure 1.3. These electric currents are the results of the complex interaction between the Earth's magnetic field and the solar wind. In this section, I will briefly review the dayside magnetopause current and the cross-tail current.

1.3.1 The Bow Shock

The Earth's bow shock is a collisionless standing shock, which is formed when the solar wind traveling at superfast speed encounters the Earth. The shock wave slows down the solar wind, which is then diverted around the Earth's magnetic field due to the frozen in magnetic field. The location, shape, and size of the bow shock vary depending on solar wind/IMF conditions. *Farris and Russell* [1994] provided a bow shock model in which the bow shock standoff distance is governed by the Mach number and the size and shape of the magnetopause.

The average distance to the most sunward tip of the bow shock is approximately 15 R_E and the average distance to the bow shock in the dawn-dusk side is about 25 R_E, though there is a dawn-dusk asymmetry [*Fairfield*, 1971]. The bow shock on the dayside has a fairly elliptical body shape with an extended tail region on the nightside.

1.3.2 The Magnetopause

The magnetosheath is the transition layer between the bow shock and the magnetopause. The solar wind is slowed down in the magnetosheath, where kinetic energy is converted to thermal and magnetic energy, thus the plasma in this region is hotter, denser and slower than the solar wind.

The magnetopause is a boundary which separates the shocked solar wind in the magnetosheath from the terrestrial magnetic field and plasma (magnetospheric region). The magnetopause can be represented as either a tangential or rotational discontinuity. When the IMF is northward directed, a larger part of the dayside magnetopause is likely a tangential discontinuity ($u_n = 0$ and $B_n = 0$, see table 1.3). The coupling between the solar wind and the terrestrial magnetic fields is small, since the solar wind plasma and magnetic field cannot penetrate into the Earth's magnetosphere. This is called a closed terrestrial magnetosphere. When the IMF points southward, the magnetopause can be approximated as a rotational discontinuity ($u_n \neq 0$ and $B_n \neq 0$). For southward IMF, there is a flux of plasma across the magnetopause which allows the penetration of solar wind into the Earth's magnetosphere. In these conditions, the magnetosphere is called an open magnetosphere [*Gurnett and Bhattacharjee*, 2005]. Observations of the magnetopause thickness show that it varies from 1 to 20 ion gyroradii (100–2000 km).

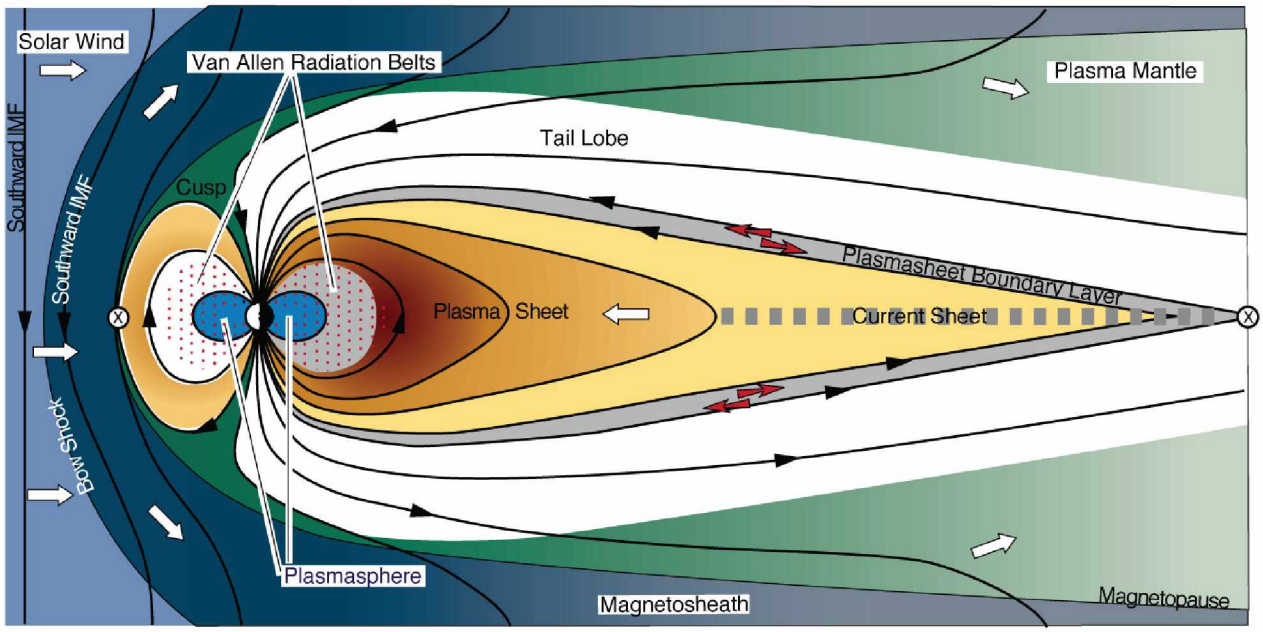

Figure 1.2. Sketch of the Earth's magnetosphere in the noon-midnight meridian. (This figure is from http://space.rice.edu/IMAGE/livefrom/sunearth.html.)

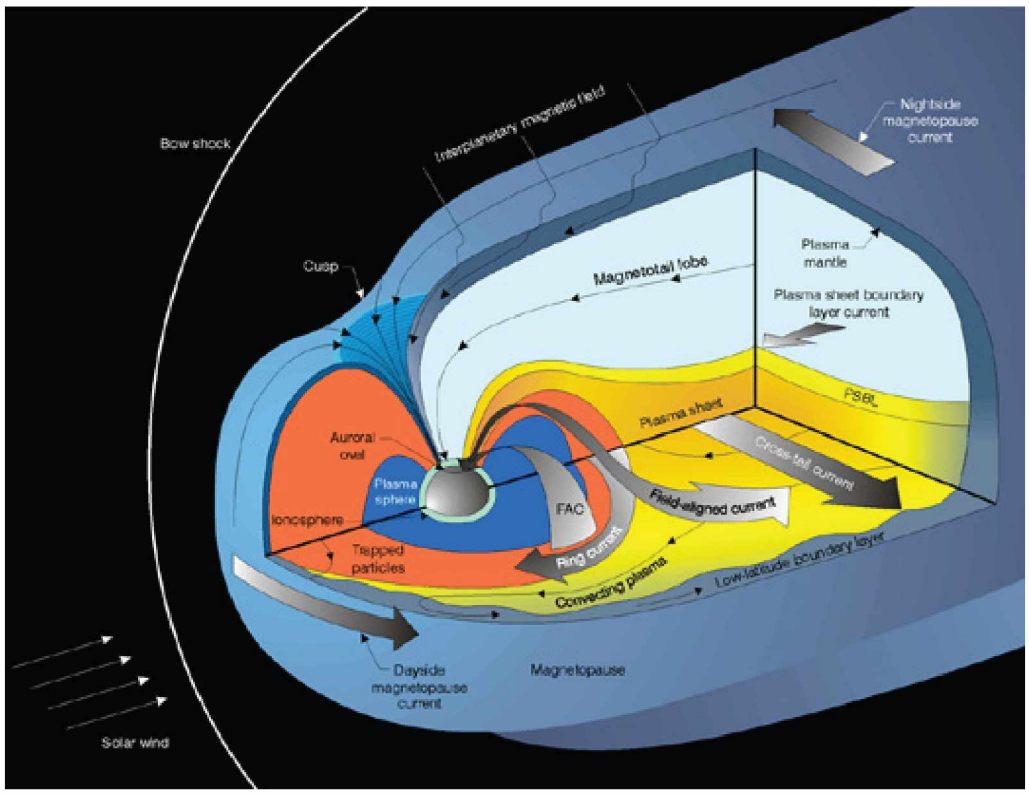

Figure 1.3. Main current systems in and around the Earth's magnetosphere [*Baumjohann and Treumann*, 1996].

The location of the magnetopause is defined as an equilibrium between the total pressure (dynamic, thermal and magnetic pressure) of the solar wind (subscript, *sw*) and the total pressure of the magnetosphere (subscript, *sp*),

$$\rho_{sw} v_{sw}^2 cos^2\theta + p_{sw} + \frac{B_{sw}^2}{2\mu_0} = p_{sp} + \frac{B_{sp}^2}{2\mu_0} \tag{1.17}$$

where θ is the angle between the solar wind and the normal direction on the magnetopause. Inside the magnetopause, the total pressure is dominated by the Earth's magnetic pressure and thus the thermal pressure can be ignored. Outside the magnetopause, the solar wind dynamic pressure contribution dominates.

$$\rho_{sw} v_{sw}^2 cos^2\theta = \frac{B_{sphere}^2}{2\mu_0} \tag{1.18}$$

The component of solar wind dynamic pressure normal to the magnetopause is balanced by the magnetic pressure inside the magnetopause.

$$n_{sw} m v^2 cos^2\theta = \frac{B_{sphere}^2}{2\mu_0} \tag{1.19}$$

The stand-off distance of the magnetopause (R_{mp}) can be calculated by using the image dipole model of the Earth's magnetic field.

$$B_{sphere} = \frac{B_0 R_E^3}{R_{mp}^3} \times 2 \tag{1.20}$$

$$n_{sw} m v_{sw}^2 cos^2\theta = (\frac{2B_0 R_E^3}{R_{mp}^3})^2 / 2\mu_0 = \frac{2B_0^2 R_E^6}{\mu_0 R_{mp}^6} \tag{1.21}$$

$$R_{mp} = (\frac{2B_0^2}{\mu_0 n m v_{sw}^2 cos^2\theta})^{\frac{1}{6}} R_E \tag{1.22}$$

When n = 5 cm^{-3}, v_{sw} = 400 km/s, B_0 = 3×10^4 nT, and θ = 0, the stand-off distance of the magnetopause (R_{mp}) is about $\sim$ 10 R$_E$ [*Gombosi*, 1998]. The stand-off distance varies from around 4.5 R$_E$ to 20 R$_E$ in the meridional directions [*Fairfield*, 1971]. The stand-off distance, the size, and the shape of the magnetopause depend on the solar wind/IMF conditions.

Ferraro [1952] proposed a simple model of the magnetopause current based on charged particle dynamics (Figure 1.4). When the solar wind encounters the Earth's magnetic field, solar wind particles are turned around by the Lorentz force ($\mathbf{F} = m\frac{d\mathbf{v}}{dt} = q(\mathbf{E} + \mathbf{v} \times \mathbf{B})$). Since Lorentz force depends on the charge, protons and electrons gyrate in opposite directions around the magnetic field. Protons gyrate in a left-handed sense, whereas electrons gyrate in a right-handed sense. The

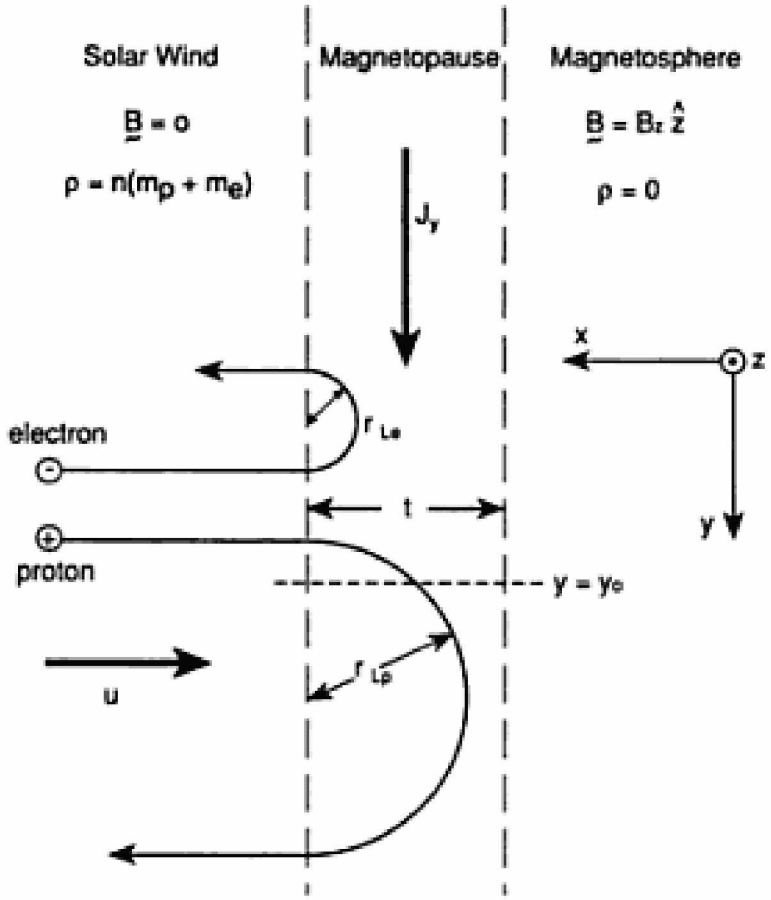

Figure 1.4. A sketch illustrating the formation of the magnetopause current [after *Ferraro*, 1952].

ions penetrate deeper into the magnetopause than electrons, since the ion inertial length (r_{Lp}) is much longer than the electron inertial length (r_{Le}). Thus the thickness of the current sheet depends on the ion gyroradius (Larmor radius, $r_g = \frac{mv_\perp}{|q|\mathbf{B}}$). The relative motion of electrons and ions forms the magnetopause current ($\mathbf{J_y}$) which flows downward in Figure 1.4 [after *Ferraro*, 1952]. The Chapman-Ferraro current [*Ferraro*, 1952] is the magnetopause current flowing from dawn to dusk in the equatorial plane.

1.3.3 The Magnetospheric Boundary Layers

The magnetospheric boundary layers are regions of the magnetosphere just inside the magnetopause and are influenced by the magnetosheath plasma. There are three types of boundary layers distributed over the magnetopause: the low latitude boundary layer (LLBL), the polar cusps, and the plasma mantle. The LLBL is the dayside boundary region located earthward of the magnetopause and extends from dayside to nightside along the flank (Figure 1.5, green region). This region contains a mixture of the magnetosheath and the magnetospheric plasma. The LLBL is found both

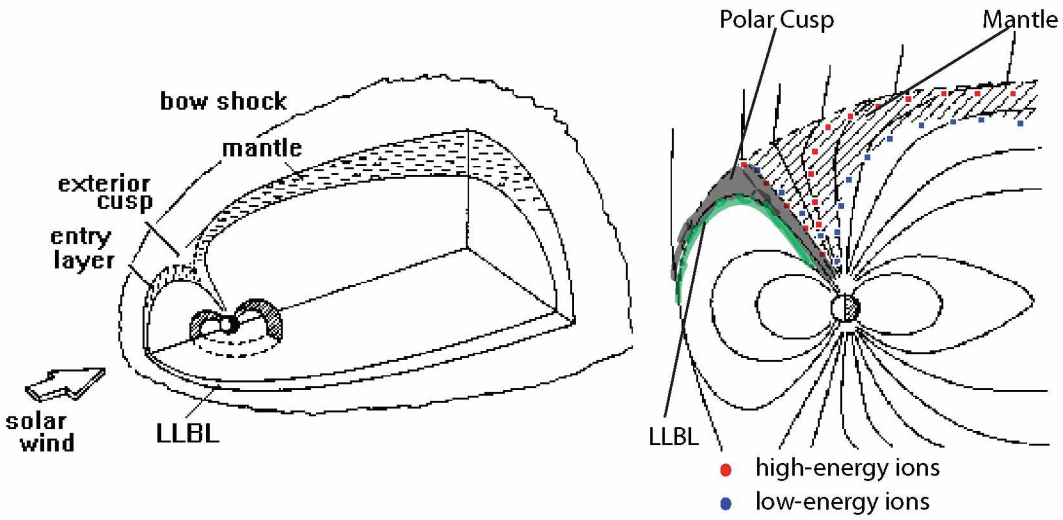

Figure 1.5. Schematic sketch of the magnetospheric boundary layer (left) such as the cusp, the plasma mantle, and low latitude boundary layer (LLBL) and zoom-in the left figure. (This figure is from http://magbase.rssi.ru/REFMAN/SPPHTEXT/blayer.html.)

on open and closed field lines over most of the dayside magnetopause.

Chapman and Ferraro [1931] proposed the existence of the regions of null magnetic field in both the northern and southern hemispheres, known as the polar cusp. It was first observed from the ISIS 2 mission in 1971 [*Heikkila and Winningham*, 1971]. The cusp is a funnel-shaped region located in the high-latitude of both hemispheres, which is marked by the gray shading in Figure 1.5 (right). The location of the polar cusp varies depending on the solar wind/IMF conditions, especially solar wind dynamic pressure and IMF direction. *Zhou et al.* [2000] found that the cusp is generally located somewhere 70°–80° in invariant latitude. The solar wind plasma can directly penetrate into the Earth's magnetosphere along open field lines emanating from the polar cusp region. Therefore, it contains both magnetospheric and magnetosheath plasma since the magnetic field lines in the cusp connect to all regions of the magnetosphere. *Sibeck et al.* [1999] showed that the cusp region is independent of the IMF direction and continuously open to the solar wind plasma. The dayside auroral precipitation occurs in this region.

The plasma mantle is the extending region poleward of the cusp region which covers much of the high-latitude magnetosphere as shown in Figure 1.5 (cross section). The high-energy ions (red dots) convect further across the magnetic field lines, whereas low-energy ions (blue dots) go deeper into the magnetosphere since the low-energy ions take a longer time to mirror from the ionosphere

to the magnetosphere. The plasma density in this region varies from 0.01 to 1 cm^{-3}, temperature is about 100 eV, and the tailward flow velocities 100–200 km/s [*Rosenbauer et al.*, 1975]. The density and energy of the magnetosheath plasma often decrease in the mantle as moving inward from the magnetosheath towards the magnetosphere, known as a gradual transition region. This region is thicker during southward IMF than during northward IMF.

1.3.4 The Magnetotail

The Earth's magnetotail is formed by extending the magnetic field from the cusp to hundreds of Earth radii on the nightside. It consists of the plasma sheet, a region of closed field lines located around tail mid plane, and the tail lobe originating from high latitude open field lines at the polar cap. The plasma sheet maps down to the auroral oval in the nightside. The polar cap region has open field lines that sweep over the nightside and closed inside the tail and close to the Earth. This region is located at the higher latitudes over $\sim 70^{\circ}$ [*Weimer et al.*, 1992]. The magnetotail is the region of storage and release magnetic energy.

In the magnetotail, there is a cross-tail current which flows from dawn to dusk across the plasma sheet. The cross-tail current separates the southern and northern lobes. It closes through the magnetopause current. Part of the tail current closes via field-aligned current which flows parallel to the magnetic field into the ionosphere. This provides a coupling between the magnetosphere and the ionosphere.

1.3.5 The Plasmasphere

Plasma in the Earth's magnetosphere comes from two major sources: solar wind and the ionosphere. Figure 1.6 shows a schematic diagram of the low-energy ions, including sources, outflow rates, densities, and percentages of the time that the populations dominate outside the ionosphere and plasmasphere. It shows that the low-energy ions (less than tens of eV) contribute most of the volume of the Earth's magnetosphere at least 50–70 % of the time [*André and Cully*, 2012].

The plasmasphere, an extension of the mid-latitude ionosphere, is a region located in the dipolar portion of the Earth's magnetosphere. It is populated by cold (few eV) and dense (10^2–10^4 cm^{-3}) plasma existing on closed field lines and is co-rotating with the Earth. The plasmaspheric particle motion is given by combining the corotation potential and the convection potential. Figure 1.7 shows low-energy particle drifts in the equatorial magnetosphere. The solid lines depict the corotational particle motion. The dashed lines are the convecting particle drift paths. On the dawnside, the corotation and convection electric fields point in the same direction and the plasma drifts sunward. On the duskside, however, the corotation and convection electric fields point in the opposite direction which generates the bulge in the closed drift region, as shown in Figure 1.7. There is one

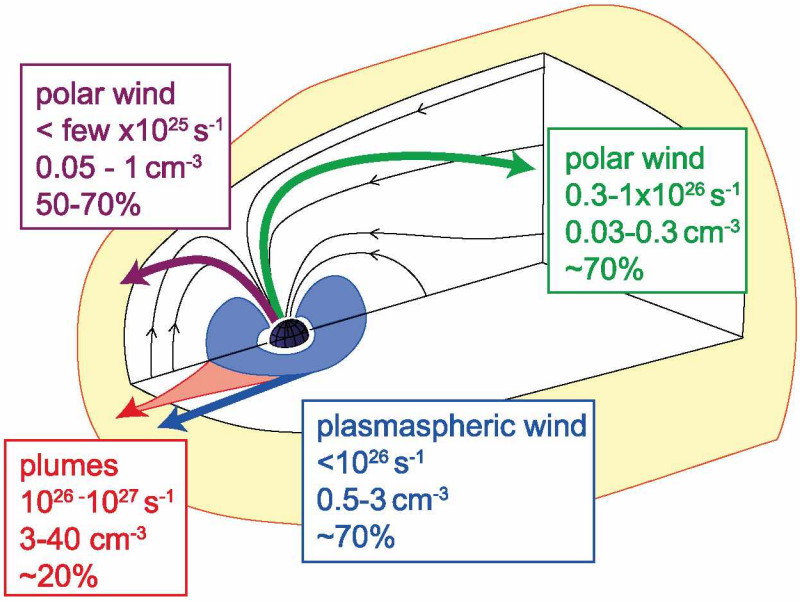

Figure 1.6. Low-energy populations of the ionospheric and plasmaspheric origins, order of magnitude outflow rates and densities, and percentage of the time that the low-energy ions dominate in the magnetosphere [*André and Cully*, 2012].

point (stagnation point) on the duskside where the electric field or the drift velocity is zero. The boundary of the trapped plasmaspheric population is called the plasmapause, which is typically found between 3 and 6 R_E. The plasmasphere shrinks in size for strong sunward convection electric field. Observations show that the size of the plasmasphere varies with geomagnetic activity, for example, the smaller size of the plasmasphere is observed during times of higher geomagnetic activity. Under steady state conditions, when the strength of sunward convection suddenly increases, particles that originally located on the outermost closed drift region suddenly find themselves on open convective paths and they move towards the dayside magnetopause [*Grebowsky*, 1970]. This is called the plasmaspheric plume. There is a limitation of the basic assumption in view of the outward motion of plasmaspheric ions. The particle drift paths caused by the superposed corotation and convection electric fields require a steady state condition. However, significant sunward convection may occur after the substorm (especially, after the onset of substorm expansion), which is a non-steady phenomenon. In addition, injection of higher energy particles into the inner magnetosphere is not considered in this simple model.

Figure 1.8(a) shows the Earth's plasmasphere on 24 May 2000 by the IMAGE extreme ultraviolet (EUV) imager [*Sandel et al.*, 2003]. As shown in Figure 1.8(a), the plume extends sunward from the eroding nightside plasmasphere. The plasmaspheric plumes are large-scale density structures that are connected to the main body of the plasmasphere and extended to the outer magnetosphere. Figure 1.8(b) shows observations of the cold and dense plasmaspheric plume using simultaneous

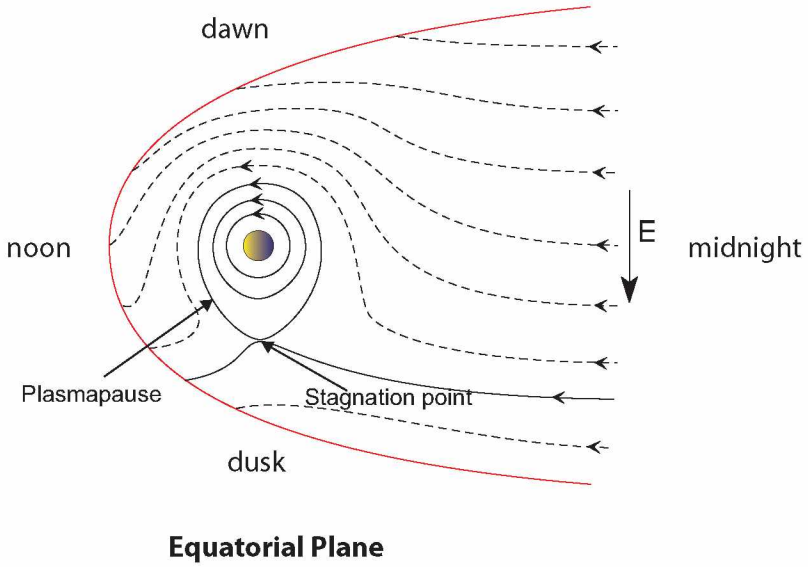

Figure 1.7. The sketch illustrates the low-energy particle drifts in the equatorial plane of the magnetosphere. The dashed lines depict sunward convective flow (or $\mathbf{E}\times\mathbf{B}$ drift), perpendicular both to the Earth's magnetic field and to the dawn-to-dusk electric field ($\mathbf{E}$) in the equatorial plane. The thick solid lines depict corotating plasma flow. Plasmapause is the boundary separating the convective and corotational flow [*Kavanagh et al.*, 1968].

ground-based total electron content (TEC) maps and measurements from the THEMIS spacecraft [*Walsh et al.*, 2014]. *Walsh et al.* [2014] showed that when a coronal mass ejection (CME) impacted the Earth's magnetosphere on 17 January 2013, the storm-enhanced density (SED) plume was extended sunward as streaming out from the inner magnetosphere to the magnetopause.

1.4 The Ionosphere

Low-energy plasma of ionospheric origin with energies below tens of eV is a significant source of magnetospheric plasma population. The Earth's ionosphere is a region of the Earth's upper atmosphere that is formed by interaction between the Earth's atmospheric neutral gases and ionizing solar ultra-violet (UV) radiation and precipitating magnetospheric plasma. It extends approximately from 70 km to 1500 km in altitude. The ionosphere consists of the four different layers (D, E, F_1 and F_2 layers) which are defined by density profiles of the dayside ionosphere. The D layer is located below 90 km altitude, the E layer is located between 90 km and 130 km, the F_1 layer from 130 km to 200 km, and the F_2 layer extends above 200 km altitude. The electron density peaks in the F_2 layer at about 250 km. O_2^+ and NO^+ ions are major species in the E layer and their densities peak at about 110 km. O^+ ions dominate above 200 km. The composition of the ionosphere is controlled by the structure, composition, and temperature of the thermosphere and also influenced by geomagnetic activity.

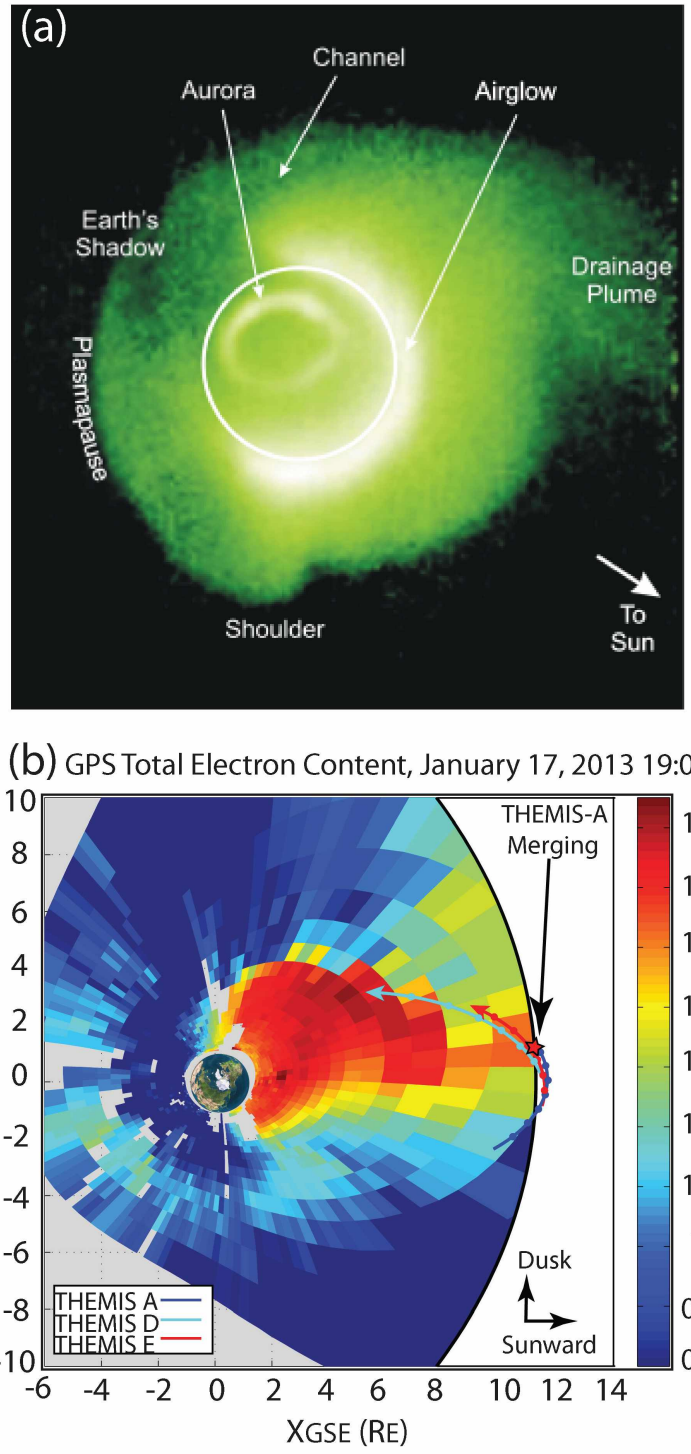

Figure 1.8. (a) The image of plasmasphere observed on 24 May 2000 by EUV, showing that the plasmaspheric erosion from the nightside plasmasphere causes a dayside plume [*Sandel et al.*, 2003]. (b) Total electron content (TEC) measurements projected onto the equatorial plane showing that the extended storm-enhanced density (SED) plume with trajectories of the THEMIS spacecraft on 17 January 2013 [*Walsh et al.*, 2014].

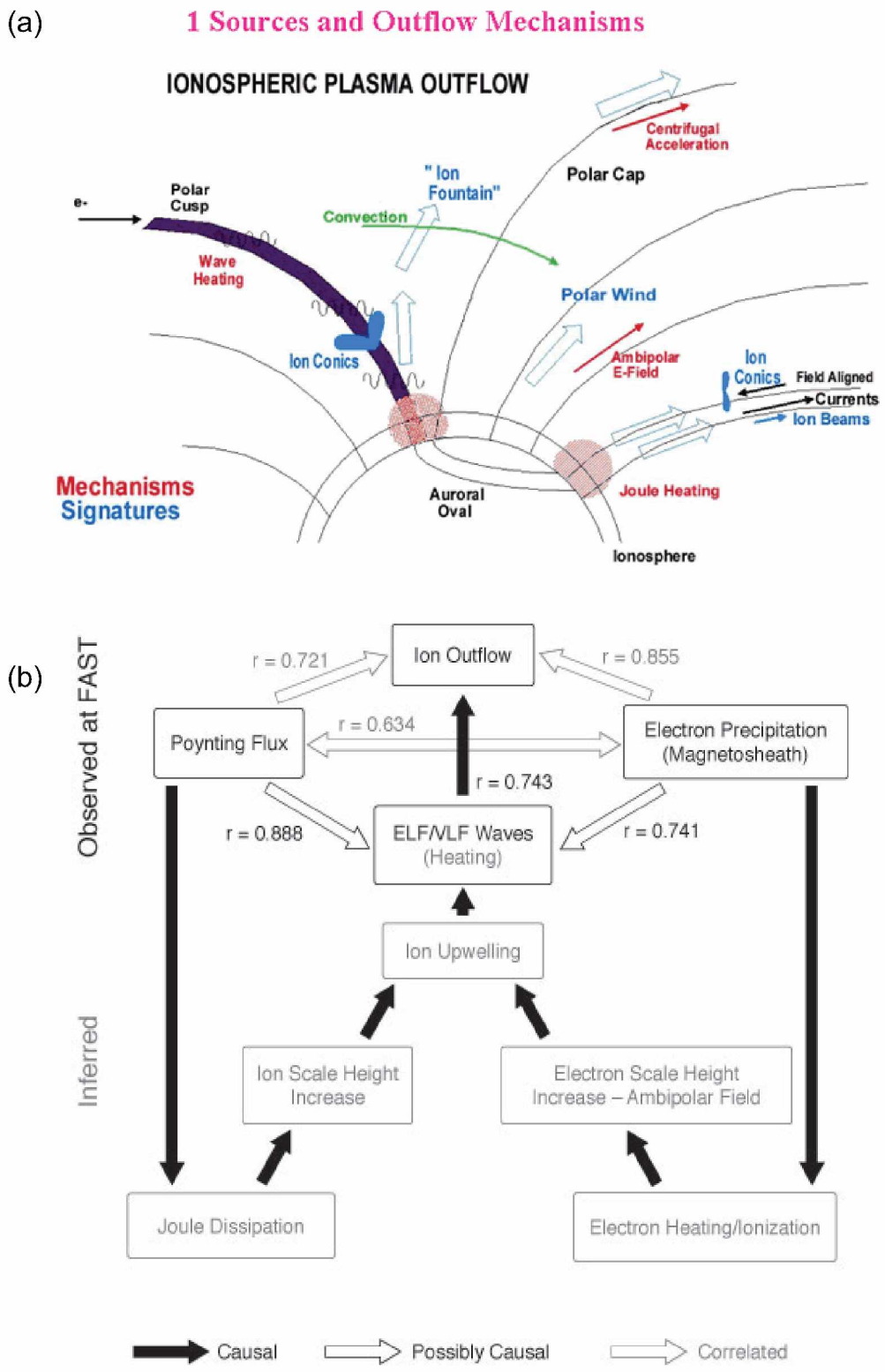

Figure 1.9. (a) Schematic diagram of plasma signatures (blue) and outflow mechanisms (red) in the polar magnetosphere of the Earth [*Sandel et al.*, 2003], (b) flow chart showing the mechanisms for generating ionospheric outflows [*Strangeway et al.*, 2005]. r is the corresponding correlation coefficient.

Particle precipitation and electromagnetic magnetospheric energy inputs to the ionosphere can heat the ionosphere and cause ions to flow outward from the ionosphere. This process is called the ionospheric outflow. There are several different mechanisms for the ionospheric outflow in the high-latitude ionosphere. These mechanisms can be sorted into two categories: bulk ion flows and suprathermal ion outflows [*Yau and André*, 1997]. The bulk ion flow comes from the topside auroral and polar cap ionosphere and include the polar wind and auroral bulk ion up-flow. The ion flows in this category acquire a bulk flow velocity. The bulk ion flows have energies up to a few eV. The polar wind can be generated by an ambient plasma pressure gradient and ambipolar electric field, primarily along the open field lines in the polar ionosphere at lower altitudes. The light thermal electrons are not as strongly bound by gravity as ions and can diffuse upward to higher altitudes than ions. This generates a transient upward pointing electric field. The ions can be accelerated upward in order to achieve quasi-neutrality. Auroral bulk ion up-flow is dominated by O^+ ions. Auroral bulk ion up-flow is driven by soft electron precipitation and convection-driven Joule heating. The frictional heating of ionospheric ions in collisional regions below 300 km drives enhanced both perpendicular and parallel ion temperatures. This increases the upward pressure gradient. The ions can flow to the higher altitudes to balance this gradient [*Yau and André*, 1997].

The second category of the suprathermal ion outflows includes ion beams, ion conics, transversely accelerated ions, and upwelling ions. This category involves ion energization process where only a fraction of the ions is accelerated to higher energies. Both ion beams and conics are dominated by H^+ and O^+ ions with the energy range from 10 eV to a few keV, which are a common phenomenon above 1 R_E altitude. Both parallel electric field and magnetic folding play an important role in the formation of ion beams at high altitudes. The ion beams have a peak flux along the upward magnetic field direction. In contrast, ion conics have a peak flux at an angle to the field direction. The ion conics are caused by the downward Poynting flux, soft electron number flux, and extremely low frequency (ELF) wave amplitude. Transversely accelerated ions are correlated with the resonant energization by broadband low-frequency waves in the ion gyrofrequency range and waves near the lower hybrid frequency. The transversely accelerated ions have a peak flux perpendicular to the magnetic field ($\sim$90° pitch angle). Upwelling ions are generated by both parallel (upward) and perpendicular energization and have energies from one to tens of eV [*Yau and André*, 1997].

Figure 1.9 shows (a) plasma signatures (blue labels) and (b) energization mechanisms (red labels) for the Earth's ionospheric outflows in the polar regions. The ionospheric source regions can be classified into four categories: the auroral zone, the cleft ion fountain, the polar cap energetic outflow, and the polar wind [*Chappell et al.*, 1987]. The auroral zone is a source of a relatively energetic magnetospheric plasma (10 eV to 10 keV). The ion outflow populations are caused by

the energization of ions both parallel and perpendicular to the magnetic field in auroral electron precipitation regions. The low-energy (< 100 eV) H^+ and O^+ ions were originated from the dayside polar cusp region, and this source has been coined as the dayside ion fountain [*Lockwood et al.*, 1985]. The intermediate energy population (10–100 eV) from polar arcs within the open magnetic field region, called the polar cap, is the polar cap outflow. The polar wind is a source of the unique low-energy (a few eV) outflow from all latitude above 51° invariant latitude, overlapping with both the auroral zone and polar cap regions [*Chappell et al.*, 1987].

Two main mechanisms for generating ionospheric outflows are shown in Figure 1.9(b). Poynting flux (left hand side), which is the flow of electromagnetic energy, results in ion frictional heating, which increases the ion scale height. Electron precipitation (right hand side) heats ionospheric electrons and therefore increases the scale height through the ambipolar electric field. The upper portion of Figure 1.9(b) shows the observations measured by Fast Auroral Snapshot Explorer (FAST) at altitudes of 350–4175 km and the lower half of the diagram is the inferred processes that can be seen to occur at lower altitudes [*Strangeway et al.*, 2005].

Fuselier et al. [1989] observed O^+ population in the dayside subsolar low latitude boundary layer from the AMPTE/Charge Composition Explorer (AMPTE/CCE). The O^+ population is a dense and field-aligned flow, which suggests that it directly comes from the high-latitude ionosphere to reach the dayside boundary layer.

Chapter 2
Introduction to Dynamic Processes in the Solar-Terrestrial System

2.1 Magnetic Reconnection

There are several mechanisms for the transfer of mass, momentum and energy from the solar wind to the terrestrial magnetosphere: magnetic reconnection, Kelvin-Helmholtz instability, diffusion, finite larmor radius effect, impulsive penetration and direct entry via cusp. The dominating mechanism for the transfer of plasma across the magnetopause is the magnetic reconnection. Reconnection occurs not only at the Earth's magnetopause, but also in the magnetosheath, the magnetotail, the solar wind and at other planets [*Borg et al.*, 2005; *Gosling et al.*, 2007; *Retinò et al.*, 2007]. I will briefly review the basic concept of the magnetic reconnection, reconnection models (both MHD reconnection model and kinetic treatments), and characteristics of reconnection process at the magnetopause and in the magnetotail in this chapter.

The basic concept of magnetic reconnection at the dayside magnetopause has been proposed by *Dungey* [1961]. Magnetic reconnection is a process in which the magnetic topology is rearranged as illustrated in Figure 2.1. Antiparallel magnetic field lines are frozen into the plasma at $\mathbf{t} < 0$. This magnetic topology exists in thin current sheet such as at the Earth's magnetopause and in the magnetotail neutral current sheet. When two oppositely directed magnetic field lines move toward the current sheet together with inflowing plasma from both sides, these opposing field lines cross-link ($\mathbf{t} = 0$). This results in the X-type reconnection configuration. The magnetic field is zero at the center of the X-point (the magnetic neutral point). The field lines on both sides are cut into halves and the half-field line from one side is reconnected with that from the other side at the X-point. This reconnection process also allows a mixture of plasma from both sides of the current sheet. The newly reconnected field lines straighten out and move away from the neutral point ($\mathbf{t} > 0$). The magnetic energy stored in the original oppositely directed fields is converted into kinetic energy, thermal energy, and particle acceleration through the reconnection process.

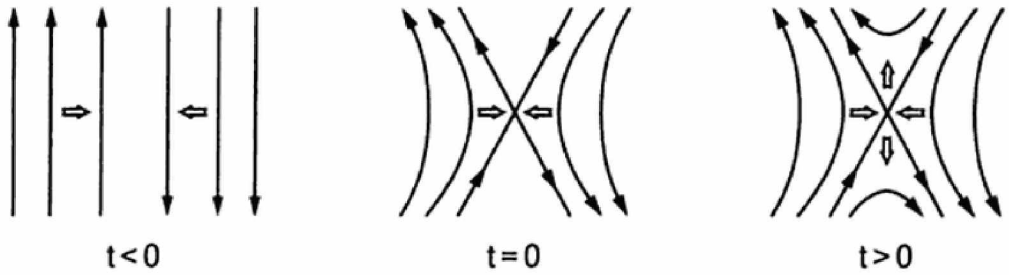

Figure 2.1. Schematic of the evolution of a 2-D magnetic reconnection configuration [*Baumjohann and Treumann*, 1996].

2.1.1 MHD Reconnection Models

The earlier magnetic reconnection models have used a magnetohydrodynamic (MHD) description. The MHD reconnection models assume that the resistivity breaks down the frozen-in condition, which is a necessary condition for the magnetic reconnection to occur. The resistive MHD equations can be rearranged in the form of the magnetic induction equation (or dynamo equation) that gives information of the time evolution of the magnetic field. In a simple electrically conducting fluid, the general induction equation for the magnetic field is written as

$$\frac{\partial \mathbf{B}}{\partial t} = \nabla \times (\mathbf{u} \times \mathbf{B}) + \frac{1}{\mu_0 \sigma} \nabla^2 \mathbf{B} \tag{2.1}$$

which is obtained from Ohm's law,

$$\mathbf{E} + \mathbf{u} \times \mathbf{B} = \eta \mathbf{j} \tag{2.2}$$

and Faraday's law,

$$\frac{\partial \mathbf{B}}{\partial t} = -\nabla \times \mathbf{E} \tag{2.3}$$

where $\mathbf{j}$ is the electrical current density, η is the magnetic viscosity ($\eta = \frac{1}{\sigma \mu_0}$), σ is the electrical conductivity, μ_0 is the magnetic permeability in free space, $\mathbf{u}$ is the average plasma velocity perpendicular to the magnetic field, $\mathbf{E}$ is the electric field, and $\mathbf{B}$ is the magnetic field. The first term on the right-hand side of equation 2.1 is called the convection term, which indicates that the magnetic field is induced and constantly maintained by convection in the plasma fluid, thus frozen-in. The second term on the right-hand side of equation 2.1 involves the plasma conductivity (σ), is called the diffusion term. If the plasma conductivity (σ) is finite the magnetic field can be changed by diffusion.

The relative importance of the two terms, convection and diffusion, on the right-hand side of the induction equation 2.1 can be investigated by the ratio between the convective and diffusive terms. This ratio can be rewritten as the characteristic speed u and length scale L of the configuration of the fluid by assuming $\nabla \approx 1/L$.

$$\frac{\mid \nabla \times (u \times B) \mid}{\mid \frac{1}{\mu_0 \sigma} \nabla^2 B \mid} \approx \frac{uB/L}{\frac{1}{\mu_0 \sigma} \frac{B}{L^2}} \tag{2.4}$$

This leads to the definition of the Magnetic Reynolds Number (R_m),

$$R_m = \mu_0 \sigma u L \tag{2.5}$$

In most regions of space plasma, the Magnetic Reynolds number is very large ($R_m \gg 1$), such as the solar wind, and therefore the magnetic field can be considered to be frozen-in to the fluid. The

Magnetic Reynolds number approaches unity.

$$\mu_0 \sigma u L = 1 \tag{2.6}$$

The length scale L, which is defined as the current sheet thickness, is determined by a balance between diffusion and convection at the edges of the current sheet. The current sheet thickness can be written as

$$L = \frac{1}{\mu_0 \sigma u} \tag{2.7}$$

However, the frozen-in condition sometimes breaks down in small localized regions to allow magnetic reconnection to occur. If the length scales are sufficiently small, the conductivity is low so that diffusion becomes important. Thus, reconnection can occur and rearrange the magnetic topology.

Sweet [1958] and *Parker* [1957] first proposed the stationary two-dimensional magnetic reconnection model shown in Figure 2.2(a). In their model there is a rectangular box with $2L$ long and 2δ wide, where $L \gg \delta$ (which is a diffusion region), that is shown shaded. The length of the diffusion region is of macroscopic scale and the width is estimated by the local resistivity. For simplicity, the inflow and outflow regions are identified by subscripts *in* and *out*, respectively. As stationary condition requires constant electric fields E inside and outside the current layer, the rate of flux change is given by

$$v_{in} B_{in} = v_{out} B_{out} = E \tag{2.8}$$

The flow is assumed to be incompressible ($\nabla \cdot \mathbf{v} = 0$), that is, $\rho_{in} = \rho_{out} = \rho$, then mass flux is conserved.

$$v_{in} L = v_{out} \delta \tag{2.9}$$

The electromagnetic energy inflowing into the diffusion regions is converted into the kinetic energy gained by the outflowing plasma. The Poynting flux provides the electromagnetic energy inflow rate per unit area.

$$| \mathbf{S} | = | \mathbf{E} \times \mathbf{H} | = \frac{EB}{\mu_0} = \frac{v_{in} B^2}{\mu_0} \tag{2.10}$$

The rate of kinetic energy gain per unit area in the incident flow is obtained from the changing the mass flowing in per unit area per unit time.

$$\Delta \mathbf{W} = \frac{1}{2} \rho v_{in} (v_{out}^2 - v_{in}^2) \tag{2.11}$$

Equating between the rates of kinetic energy and electromagnetic energy and using $v_{out} \gg v_{in}$ give

$$\frac{v_{in} B^2}{\mu_0} = \frac{1}{2} \rho v_{in} v_{out}^2 \tag{2.12}$$

so

$$\frac{B^2}{2\mu_0} = \frac{\rho v_{out}^2}{2} \tag{2.13}$$

The outflow speed can be written as

$$v_{out} = \frac{B}{\sqrt{\mu_0 \rho}} = V_A \tag{2.14}$$

This outflow speed is called the Alfvén speed (V_A). V_A is the speed of motion of the Alfvén wave which propagates along magnetic field lines.

Equations 2.8 and 2.9 state that if $L \gg \delta$, then $v_{out} \gg v_{in}$ and $B_{in} \gg B_{out}$. Thus, the kinetic energy of the outflowing plasma is much larger than the inflowing rate of kinetic energy, whereas the outflowing magnetic energy is much smaller than the inflowing magnetic energy, when considering the energy balance. This indicates that magnetic energy is dissipated and converted into kinetic energy (plasma bulk flow energy and thermal energy) during the reconnection process.

The efficiency of the reconnection can be estimated by the magnetic reconnection rate that can be defined as the inflow speed into the reconnection site,

$$v_{in} = \frac{1}{\delta \mu_0 \sigma} \tag{2.15}$$

$$v_{in}^2 = \frac{1}{\delta \mu_0 \sigma} \left(v_{out} \frac{\delta}{L} \right) = v_{out} \frac{1}{\mu_0 \sigma L} = v_{out}^2 \frac{1}{\mu_0 \sigma L V_A} \tag{2.16}$$

Thus, the dimensionless reconnection rate can be written as

$$\frac{v_{in}}{v_{out}} = \frac{1}{\sqrt{\mu_0 \sigma L V_A}} = \frac{1}{\sqrt{S}} \tag{2.17}$$

where S ($= \mu_0 \sigma L V_A$) is Lundquist number that is a Magnetic Reynolds number based on the Alfvén speed. The frozen-in condition is broken down in this region where the magnetic field lines diffuse and reconnect.

The Magnetic Reynolds number in all solar-system plasmas is very large so that the magnetic reconnection rate given by Sweet-Parker model is too slow to explain the rapid energy release such as solar flares. Figure 2.2(b) shows a Petschek's reconnection model [*Petschek*, 1964]. The length of the diffusion region of Petschek's model is much shorter than that of Sweet-Parker's model. Note that a much shorter and thinner diffusion region allows for the faster reconnection rate. The plasma does not have to flow through the diffusion region to be accelerated. It can be accelerated by slow mode shocks (dashed lines) that are connected to the diffusion region (shaded region). This allows a fast enough reconnection rate to explain many observations in terms of magnetic reconnection

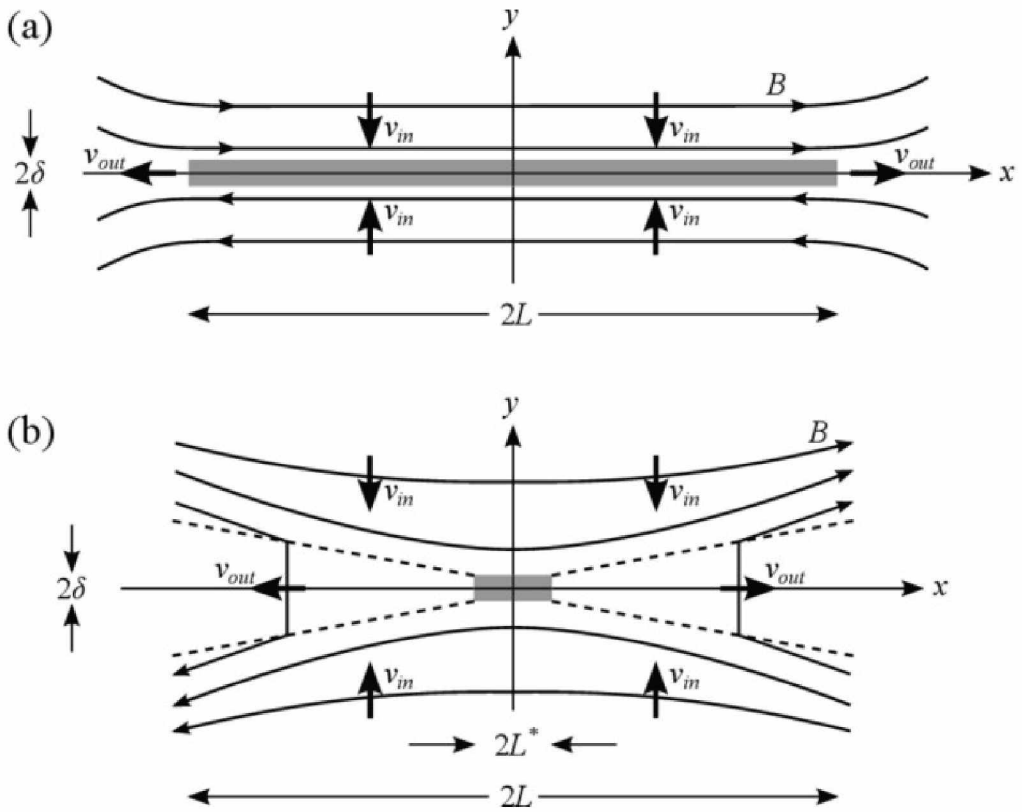

Figure 2.2. Configurations of the (a) Sweet-Parker and (b) Petschek's magnetic reconnection models [*Comisso and Asenjo*, 2014]. The inflow and outflow regions are indicated by subscripts *in* and *out*. The magnetic diffusion regions with length $2L$ and width 2σ are shaded. The dashed lines indicate the slow mode shocks.

such as the solar flares.

Both the Sweet Parker and Petschek models describe symmetric reconnection with two identical inflow regions. This description is suitable for some cases, such as reconnection in the Earth's magnetotail, however, plasma and magnetic field parameters in the two inflow regions are quite different at the magnetopause. The plasma density on the magnetosheath side at the Earth's dayside magnetopause is much higher than that on the magnetospheric side and the magnetic field strength on the magnetosheath side is usually smaller than that on the magnetospheric side. *Cassak and Shay* [2007] did a Sweet-Parker type scaling analysis for the asymmetric antiparallel reconnection by using the laws of conservation of mass, energy, and magnetic flux (Figure 2.3). The resulting scaling laws for asymmetric reconnection including the reconnection rate (E), the outflow speed (v_{out}), and the outflow number density (n_{out}) are written as functions of the asymmetric upstream magnetic field strengths and densities [*Cassak and Shay*, 2007].

$$E \sim \left(\frac{B_1 B_2}{B_1 + B_2}\right)\left(\frac{v_{out}}{c}\right)\left(\frac{2\delta}{L}\right) \tag{2.18}$$

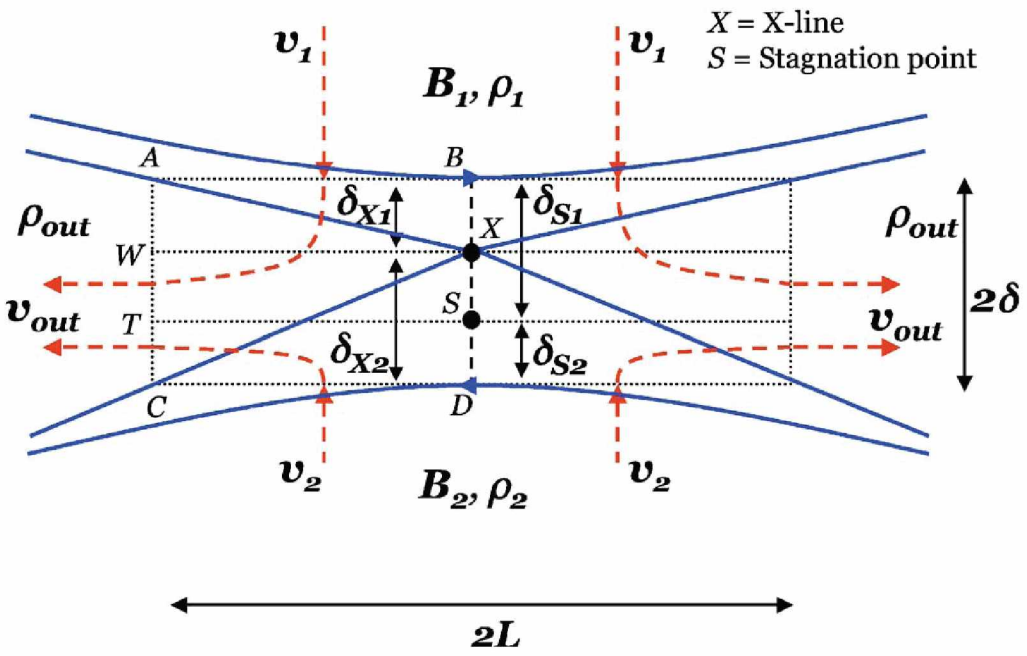

Figure 2.3. Schematic geometry of the diffusion region during asymmetric reconnection [*Cassak and Shay*, 2007]. The subscripts of "1", "2", and "out" represent values of inflow regions on either side of the diffusion region and values for the outflow region, respectively.

$$v_{out}^2 \sim \frac{B_1 B_2}{\mu_0 m n_{out}} \tag{2.19}$$

$$n_{out} \sim \frac{n_1 B_2 + n_2 B_1}{B_1 + B_2} \tag{2.20}$$

Where B is the magnetic field, m is the particle mass, n is the number density, δ is the half-width, and L is the half-length of the dissipation region. The subscripts 1, 2, and *out* indicate each side of the current sheet and outflow region, respectively. The reconnection rate decreases as density increases.

One way to predict the efficiency of reconnection is monitoring the outflow speed in the exhaust region, although it does not provide the reconnection rate quantitatively. For a rotational discontinuity at the magnetopause, the outflow (v_{out}) is a hybrid Alfvén speed (V_A) which depends on the magnetic field strengths and plasma densities on both sides of the magnetopause [*Cassak and Shay*, 2007],

$$V_A = \sqrt{\frac{B_m B_s (B_m + B_s)}{\mu_0 (\rho_m B_s + \rho_s B_m)}} \tag{2.21}$$

where ρ is the mass density (nm), the subscripts of m and s represent the values on the magnetospheric side and the magnetosheath side of the magnetopause, respectively.

2.1.2 Kinetic Treatments

The MHD description of the reconnection is quite accurate at large scales. However, there are some phenomena that the resistive MHD reconnection model cannot describe such as sudden onsets of the magnetic reconnection during magnetic substorms and energetic electron being released during magnetic reconnection. The non-MHD effects are important at scales comparable to or smaller than the ion inertial length (c/w_{pi}). The generalized Ohm's law must be taken into account in order to understand non-MHD effects [*Drake*, 1995].
The generalized Ohm's law is written as

$$\mathbf{E} = -\mathbf{v} \times \mathbf{B} + \eta \mathbf{j} + \frac{1}{en}\mathbf{j} \times \mathbf{B} - \frac{1}{en}\nabla p_e + \frac{m_e}{ne^2}\left[\frac{\partial \mathbf{j}}{\partial t} + \nabla \cdot (\mathbf{ju} + \mathbf{uj})\right] \tag{2.22}$$

where η is resistivity. Generalized Ohm's law describes four possible processes that can break down the frozen-in condition so that reconnection can occur. The terms on the right-hand side of the generalized Ohm's law are the motional electric field, resistivity, Hall term, electron pressure, and electron inertia, respectively. Each of these terms is associated with a scale length and that term is important when the typical length scale of a system L is comparable to or smaller than that scale length. The scale length of each term can be computed by letting each term comparable to the motional electric field term ($\mathbf{v} \times \mathbf{B}$) [*Priest and Forbes*, 2000].

For the resistive term $\eta\mathbf{j}$, assuming $\nabla \approx 1/L$ and $|\mathbf{j}| \approx B/(\mu_0 L)$,

$$\eta \frac{B}{\mu_0 L} \approx VB \tag{2.23}$$

L can be solved,

$$L_{resistive} \approx \frac{\eta}{\mu_0 V} = \lambda_{res} \tag{2.24}$$

For the Hall term $\frac{1}{en}\mathbf{j} \times \mathbf{B}$,

$$\frac{B^2}{en\mu_0 L} \approx VB \tag{2.25}$$

solving for L,

$$L_{Hall} \approx \frac{B}{en\mu_0 L} = \frac{\sqrt{m_i}}{eV\sqrt{n\mu_0}}\frac{B}{\sqrt{\mu_0 n m_i}} = \sqrt{\frac{m_i}{\mu_0 n}}\frac{1}{e}\frac{V_A}{V} = \sqrt{\frac{m_i c^2 \epsilon_0}{n}}\frac{1}{e}\frac{V_A}{V} = \frac{c}{w_{pi}}\frac{V_A}{V} = \frac{\lambda_i}{M} \tag{2.26}$$

where

$$\lambda_i = \frac{c}{w_{pi}} \tag{2.27}$$

is the ion inertial length (or ion skin depth), w_{pi} is the ion plasma frequency, and M is the Alfén

Mach number,

$$M = \frac{V}{V_A} \tag{2.28}$$

For the electron pressure term $\frac{1}{en}\nabla p_e$, assuming $p_e = nk_BT_e$,

$$\frac{nk_BT_e}{enL} \approx VB \tag{2.29}$$

L can be solved,

$$L_{pressure} \approx \frac{k_BT_e}{eVB} \tag{2.30}$$

Assuming $T_e \approx T_i$, $L_{pressure}$ can be rewritten as

$$L_{pressure} \approx \frac{k_BT_e}{eVB} \approx \frac{\sqrt{k_BT_e}}{V_A}\frac{V_A}{V}\frac{\sqrt{k_BT_i}}{eB} = \frac{\sqrt{k_BT_e/m_i}}{B/\sqrt{\mu_0\rho}}\frac{V_A}{V}\frac{\sqrt{k_BT_im_i}}{eB} = \sqrt{\frac{nk_BT_e}{B^2/\mu_0}}\frac{V_A}{V}\frac{\sqrt{k_BT_im_i}}{eB} \tag{2.31}$$

$$L_{pressure} \approx \frac{\beta^{1/2}}{M_A}R_{gi} \tag{2.32}$$

where β is the plasma beta,

$$\beta = \frac{nk_BT_e}{B^2/2\mu_0} \tag{2.33}$$

and R_{gi} is the ion gyro-radius,

$$R_{gi} = \frac{\sqrt{k_BT_im_i}}{eB} \tag{2.34}$$

Assuming $V \approx \sqrt{3k_BT_i/2m_i} = V_{thermal}$, $L_{pressure}$ can be rewritten as

$$L_{pressure} \approx \frac{k_BT_e}{eVB} = \frac{m_i}{eB}\frac{k_BT_e}{m_iV} \approx \frac{\sqrt{k_BT_e/m_i}}{w_{ci}}\frac{\sqrt{k_BT_i/m_i}}{V} \approx \frac{\sqrt{k_BT_e/m_i}}{w_{ci}} = r_{ci} \tag{2.35}$$

where $r_{ci} = \frac{\sqrt{k_BT_e/m_i}}{w_{ci}}$ is the effective ion Larmor radius.

For the electron inertial term,

$$\frac{m_e}{ne^2}\left[\frac{\partial \mathbf{j}}{\partial t} + \nabla\cdot(\mathbf{ju} + \mathbf{uj})\right] = \frac{1}{\epsilon_0 w_{pe}^2}\frac{d\mathbf{j}}{dt} \tag{2.36}$$

assuming $d/dt \approx V/L$, this term can be rewritten as

$$\frac{1}{\epsilon_0 w_{pe}^2}\frac{VB}{\mu_0 L^2} = \frac{c^2}{w_{pe}^2}\frac{VB}{L^2} \approx VB \tag{2.37}$$

L can be solved,

$$L_{inertia} \approx \frac{c}{w_{pe}} = \lambda_e \tag{2.38}$$

where w_{pe} is the electron plasma frequency and λ_e is the electron inertial length or electron skin depth.

The last four terms on the right-hand side of equation 2.22 are associated with four characteristic scale lengths: the ion inertial length $\lambda_i = c/w_{pi}$, the electron inertial length $\lambda_e = c/w_{pe}$, the effective ion Larmor radius $r_{ci} = (\kappa_B T_e/m_i)^{1/2}/w_{ci}$, and the resistive scale length $\lambda_{res} = \eta/\mu_0|\mathbf{v}|$. Magnetic reconnection can occur when the thickness of the current sheet is comparable to a characteristic scale length. Theoretically, reconnection can be initiated either by resistive or collisionless mechanisms. If the resistive scale size (λ_{res}) is smaller than the ion inertial length, collisionless effects are dominant. Collisions and resistivity can be ignored when the reconnection layer (current layer) is comparable to the ion inertial length. This reconnection is regarded as a collisionless process [*Drake*, 1995; *Shay et al.*, 1999].

When the reconnection layer width is comparable to the ion inertial length, the Hall term is important. Ions decouple from the magnetic field at the ion inertial length while the magnetic field lines are still frozen-into the electron fluid. Electrons decouple with the magnetic field at the electron inertial length. Since the ion inertial length is much longer than the electron inertial length, the ions are first unmagnetized (at the larger ion scale length) while the electrons are still coupled to the magnetic field. The separation between ions and electrons produces a system of currents, namely, the Hall current system. The Hall current induces a quadrupolar out-of-plane magnetic field pattern (B_y) near an X-type neutral line.

Figure 2.4 shows the schematic configuration of the Hall current system [*Øieroset et al.*, 2001]. The shaded orange area shows the ion diffusion region and the electron diffusion region is marked by the small grey box. The x-component of the coordinate system is directed towards the Sun, y is the out-of-plane direction, and z direction is the normal component to the current sheet. Top and bottom regions are referred to as the upstream regions (or the inflow regions). Left and right regions are referred to as the downstream regions (or the outflow regions). There are reconnected field lines (curved black lines) and plasma outflow (red arrows) in the downstream region. The upstream and downstream regions are separated by the separatrix which are the magnetic field lines connected to the X-line. The oppositely directed field lines from top and bottom reconnect at a distance of the order of the ion skin depth (c/w_{pi}) from the X-line. *Øieroset et al.* [2001] reported that a bipolar signature in the y-component of the magnetic field (B_y) was observed by the Wind spacecraft as traveling from the region of Earthward jets to the tailward jet region. The observation of the Hall magnetic field signature during magnetotail reconnection indicates that magnetic reconnection can

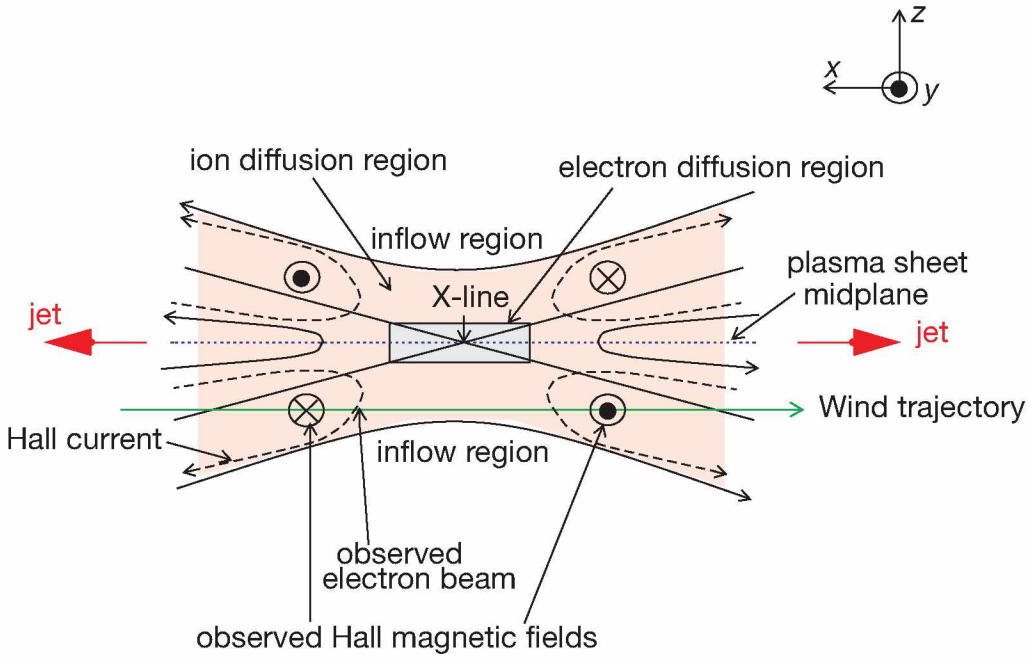

Figure 2.4. Schematic configuration of the Hall current system in the magnetotail [*Øieroset et al.*, 2001].

occur in the absence of a collisional resistivity.

2.1.3 Magnetic Reconnection at the Magnetopause

Magnetic reconnection in the Earth's magnetosphere can occur at the dayside magnetopause as well as in the magnetotail. Figure 2.5 shows a simple configuration of magnetic reconnection in an open magnetosphere model proposed by *Dungey* [1961]. The solid lines are interplanetary magnetic field lines (blue) and geomagnetic field lines (red). The closed geomagnetic field reconnects with the interplanetary magnetic field during periods of southward IMF at the dayside magnetopause. The reconnected Earth's magnetic field lines (purple) become open field lines and charged particles from the solar wind can penetrate into the Earth's magnetosphere. This also allows transport of mass, momentum, and energy from the solar wind to the Earth's magnetosphere.

During northward IMF, the magnetosheath magnetic field (tailward) and the terrestrial magnetic field (sunward) are antiparallel in the high-latitude region (beyond the polar cusp) and magnetic reconnection can occur there. Figure 2.6 illustrates the case when the reconnection occurs at Earth's high-latitude in the northern hemisphere [*Frey et al.*, 2003]. The magnetosheath plasma is accelerated in both tailward and sunward directions, as marked by the red arrows. The plasma of the magnetosheath origin can penetrate tailward into the low altitude and can also be found deep within the polar cap region during the reconnection.

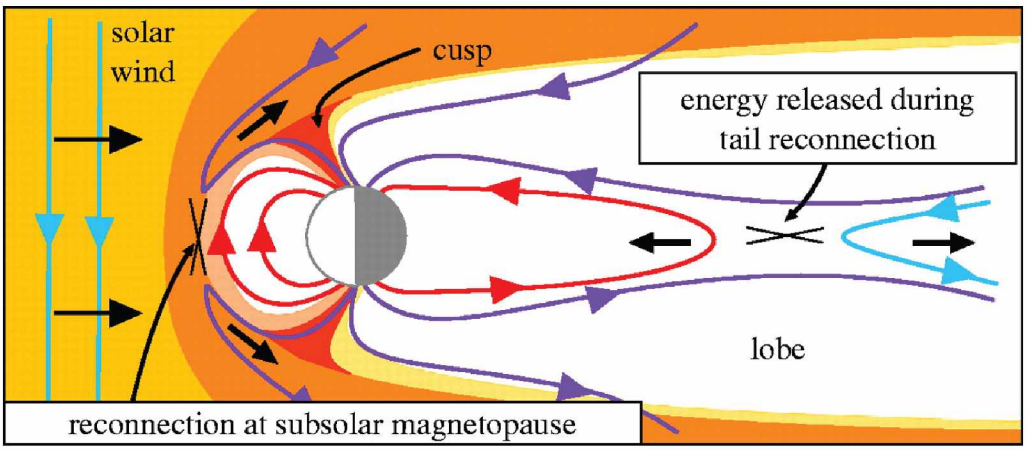

Figure 2.5. The configuration of an open magnetosphere as proposed by *Dungey* [1961] (This figure is from http://rsta.royalsocietypublishing.org/content/366/1884/4489).

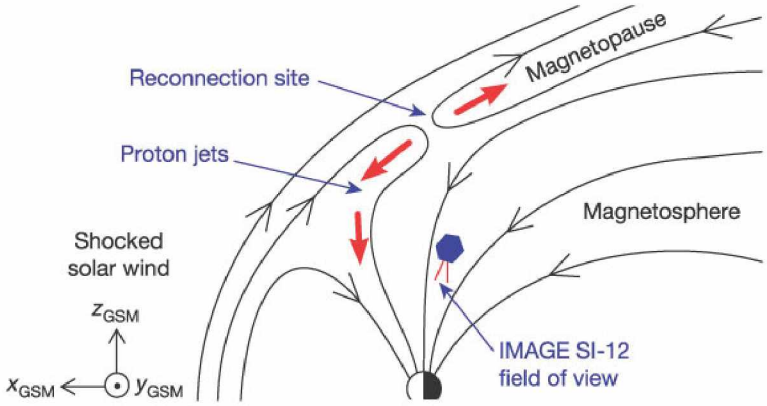

Figure 2.6. Schematic illustration of the reconnection in the northern tail lobe during northward IMF [*Frey et al.*, 2003].

The following signatures have been used to identify reconnection at the magnetopause.

1. The primary evidence for reconnection has been the observations of high speed plasma flows which satisfy the Walén relation. The Walén test is a technique for comparing the observed bulk plasma flows with those predicted from the reconnection theory [*Walén*, 1944]. The reference frame in which the electric field vanishes is called the de Hoffmann-Teller (HT) frame [*de Hoffman and Teller*, 1950]. In this frame, the plasma bulk flow resulting from steady state reconnection is field-aligned and Alfvénic [*Sonnerup et al.*, 1990]:

$$\mathbf{u} - \mathbf{u_{HT}} = \pm \mathbf{v_A} = \pm \frac{\mathbf{B}}{\sqrt{\mu_0 \rho}} \tag{2.39}$$

   where $\mathbf{u} - \mathbf{u_{HT}}$ is the plasma velocity in the HT frame and $\mathbf{v_A}$ is the Alfvén velocity.

2. The reflection and transmission of magnetospheric and magnetosheath ion species at the magnetopause provide strong evidence for reconnection. *Gosling et al.* [1990a] described the particle behavior during reconnection at the magnetopause as illustrated in Figure 2.7. The white arrows indicate the magnetosheath and magnetospheric particles. Two different plasma populations flowing from the magnetosheath side (left) and the magnetospheric side (right) enter the reconnection region (cross-hatching) [*Gosling et al.*, 1990a]. Some of the incident populations will reflect off the magnetopause, returning to the magnetosheath or magnetosphere and some will cross the magnetopause. The field lines labeled S1 and S2 (separatrix) are the newly reconnected field lines and formed the X-point. The two boundaries E1 and E2 (I1 and I2) where electrons (ions) have been accelerated are formed through the reconnection process [*Gosling et al.*, 1990a]. These boundaries are not field aligned, because the particles drift or convect with the magnetic field. Both electrons and ions drift across the magnetic field at the same speed ($\mathbf{E} \times \mathbf{B}$ drift). However, the light electrons move along the field line much faster than ions. Thus, the electron boundaries are more closely field-aligned than the ion boundaries [*Kivelson and Russell*, 1995]. *Cowley* [1982] predicted the ion velocity distributions near the magnetopause based on a kinetic description of quasi-static reconnection. These predictions were confirmed by observations [*Fuselier et al.*, 1991].

3. The flux transfer events (FTEs) [*Haerendel et al.*, 1978; *Russell and Elphic*, 1978] have been regarded as the product of patchy reconnection at the magnetopause. The FTE was first proposed by *Russell and Elphic* [1978] who suggested that patchy magnetic reconnection generates a magnetic flux tube (or rope) which connects the magnetosheath and magnetospheric sides and thus contains both magnetosheath and magnetospheric plasma. The FTE is characterized by a bipolar signature in the normal component of the magnetic field (B_N) and an

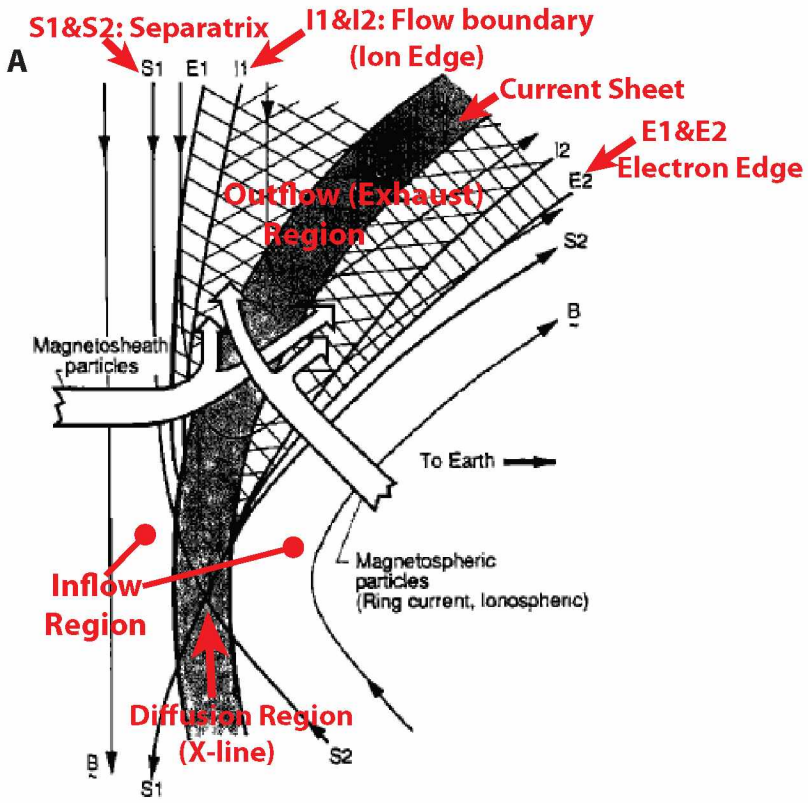

Figure 2.7. Sketch of the dayside magnetopause reconnection geometry. S1 and S2 represent the separatrix which are newly reconnected field lines connected to the X-line. E1, E2, I1, and I2 mark the boundaries of the accelerated electrons and ions. When the reconnection occurs, magnetosheath and magnetospheric particles entering from the left and right, respectively, combine on the reconnected flux tubes [*Gosling et al.*, 1990a].

enhancement in the magnetic field strength [*Russell and Elphic*, 1978].

Figure 2.8 (top) shows a sketch of an FTE [*Russell and Elphic*, 1978]. The magnetosheath and magnetospheric magnetic field lines drape around the flux tube and can generate the bipolar signature of B_N. The reconnected open flux tube lies along the magnetopause, partially inside and outside of the current sheet. The open flux tube is pulled upward by magnetic tension. Figure 2.8 (bottom) shows the magnetic field measurements from ISEE 1 and 2 at the magnetopause in the boundary normal coordinates on 29 November 1977 [*Elphic and Russell*, 1979]. In the boundary normal coordinate system, B_N points along the magnetopause normal, B_L is directed northward along the magnetospheric field, and B_M points dawnward. The FTEs are easily distinguishable. Three FTEs observed in the magnetosheath are marked by shaded regions. The magnetic field strength is often larger within FTEs than that in the magnetosheath and there is a polarity, a positive and then a negative perturbation in B_N. The polarity, B_N first positive and then negative (outward then inward), is usually observed around the open flux tube when the spacecraft is in the north of the magnetic equator. If the observed polarity of B_N is opposite (negative/positive or inward then outward), the spacecraft is located in the south of the magnetic equator [*Elphic*, 1990]. In addition, these magnetic flux tubes are moving faster than the magnetosheath plasma flow. Most FTEs are observed when the IMF is southward [*Elphic*, 1990].

2.1.4 Magnetic Reconnection in the Magnetotail

The reconnected Earth's magnetic field and IMF convect tailward carrying the solar wind and become field lines of the geomagnetic tail. During the anti-sunward motion of field lines, the ionospheric plasma is joined together with the magnetosheath plasma. The mixed plasma convects onto the tail and fills the mantle. The convected plasma from the plasma mantle moves towards the plasma sheet in the magnetotail. The plasma sheet is a region that separates the oppositely directed magnetic fields of the north and south lobes. The magnetic fields point towards the Earth in the north lobe, whereas they direct away from the Earth in the south lobe. Therefore, the neutral sheet is a suitable position for reconnection to occur. The ejection of plasma by the reconnection can produce the beautiful phenomenon of auroras.

Figure 2.5 shows a schematic illustrating the Earth's magnetosphere in the noon-midnight plane showing the magnetic reconnections at the dayside magnetopause and the nightside magnetotail. Oppositely directed magnetic field lines convect towards the plasma sheet and reconnect in the magnetotail. The inflow plasmas from the southern and northern lobes have similar plasma properties in the magnetotail reconnection. The tailward reconnected magnetic field lines are pulled

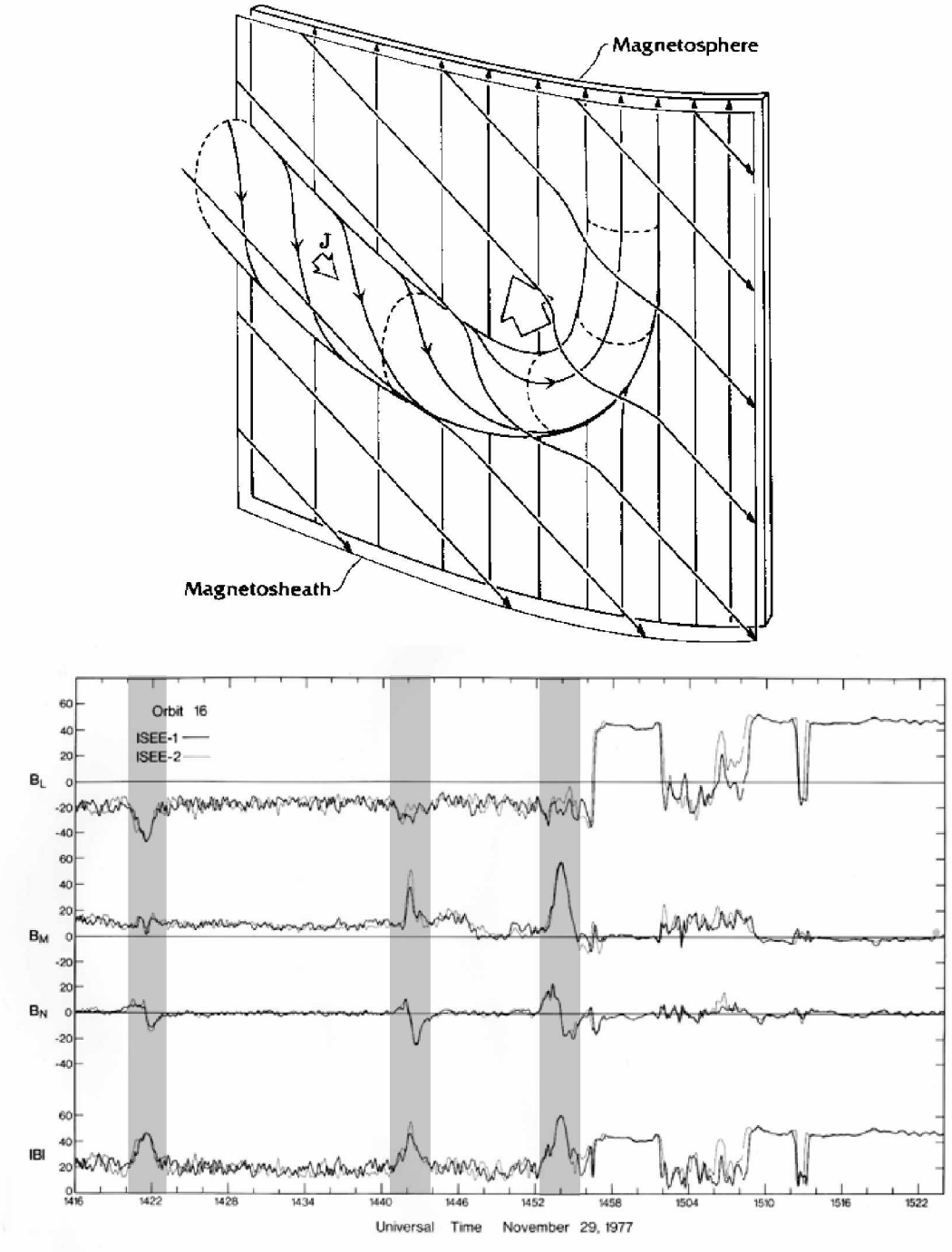

Figure 2.8. Sketch of a magnetic flux tube (top) and magnetic field data across the magnetopause in the presence of FTEs indicated by the shaded region (bottom) [*Elphic and Russell*, 1979]

away and joined with the IMF by magnetic tension. The plasma jets generated by magnetic reconnection move away from the reconnection diffusion region (black arrows). The earthward flows of plasma move along the newly reconnected closed field lines and toward the Earth's southern and northern poles. The earthward field-aligned particles mirror at low altitude and return along the plasma sheet boundary layer. Then, the counterstreaming particles are thermalized and become a more isotropic plasma.

2.2 Geomagnetic Storm and Substorm

The geomagnetic activity is highly correlated with variations at the Sun, such as the solar-cycle variation. Geomagnetic storms and substorms are two major types of geomagnetic activity. A magnetospheric substorm is a brief (2–3 hours) disturbance in the magnetosphere which occur when the IMF turns southward. During a substorm a large amount of energy is released from the magnetotail into the high latitude ionosphere. A magnetospheric storm is a world-wide depression of the horizontal component of the Earth's magnetic field which lasts for several days. Geomagnetic storms are directly driven by coronal mass ejections (CME), solar flares, or fast streams. Geomagnetic indices (e.g., AE, AL, AU, K_p and D_{st} indices) are used to measure the disturbances of geomagnetic fields. The following most commonly used indices will be introduced in this section: (1) Low-latitude (equatorial D_{st}); (2) Auroral zone (AE, AL and AU); (3) Mid-latitude (K_p). Substorms are characterized by AE (auroral electrojet) index and D_{st} (disturbance storm time) index is used to measure the intensity of magnetic storms.

2.2.1 Magnetic Storm

Geomagnetic storms are major magnetic disturbances in the magnetosphere that occur when the IMF turns southward and remains southward for an extended interval. The characteristic signature of a magnetic storm is a depression in the horizontal component (H) of the Earth's magnetic field. This depression is caused by the enhanced ring current encircling the Earth in the westward direction. Figure 2.9 shows a typical geomagnetic storm phases, the initial, main, and recovery phases monitored by the D_{st} index. There is a sudden positive increase in the H component which is known as a sudden storm commencement (the initial phase). This was followed by the development of a large decrease in the H component (the main phase). The recovery phase is caused by loss of ring current ions. It leads to a decrease in the intensity of the ring current and the geomagnetic field approaches its prestorm condition [*Kivelson and Russell*, 1995]. The magnitude of magnetic storms can be defined by the minimum D_{st} index.

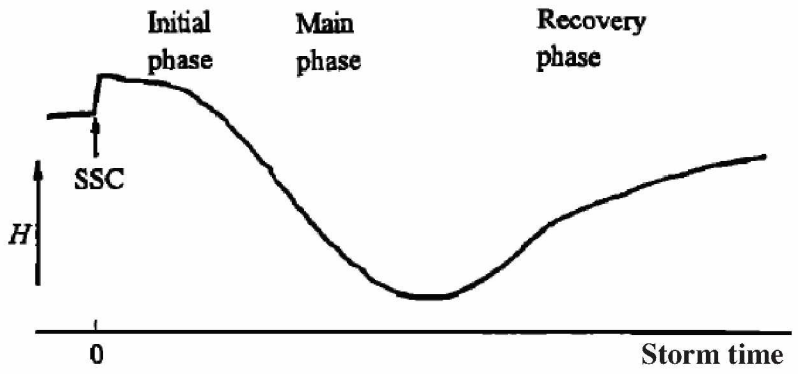

Figure 2.9. Schematic diagram of the typical magnetic storm phases: the initial, main, and recovery phases [*Kamide et al.*, 1998].

2.2.2 Substorm

A magnetospheric substorm is a transient process during which a significant amount of energy is first stored in the magnetotail with a subsequent fast release of this energy. The energy dissipation during a substorm confined mostly to the auroral oval [*Rostoker et al.*, 1980]. When a dayside magnetic reconnection occurs, magnetic flux is removed from the dayside and accumulated in the magnetotail (growth phase of a substorm: energy loading). Subsequently, the stored magnetic energy is explosively released into the ionosphere known as magnetospheric substorms (expansion phase: energy dissipation). The onset of the expansion phase is signaled by a sudden brightening of an auroral arc around midnight. It is accompanied by an intensification of the auroral electrojets [*McPherron*, 1979]. During substorms, the magnetic reconnection is initiated in the magnetotail and a portion of the plasma is ejected away from the X-line. The magnetosphere returns to its ground state (recovery phase) [*Kivelson and Russell*, 1995].

2.2.3 Geomagnetic Indices

D_{st} index

D_{st} index is used to measure the storm strength. It is derived from the average value of the equatorial H disturbances measured hourly at four near-equatorial geomagnetic stations. Larger negative D_{st} indicates a more intense storm. Figure 2.10 (top) shows the magnetometer data (horizontal component of the magnetic field H) from four near-equatorial geomagnetic observatories and Figure 2.10 (bottom) shows the corresponding D_{st} index plotted as the middle line with maximum (upper line) and minimum (lower line) disturbance values for the Halloween storm in 2003 [*Love and Remick*, 2007]. D_{st} index is determined by the difference between the maximum and minimum disturbance fields among the four observatories. A geomagnetic storm often starts with a sudden

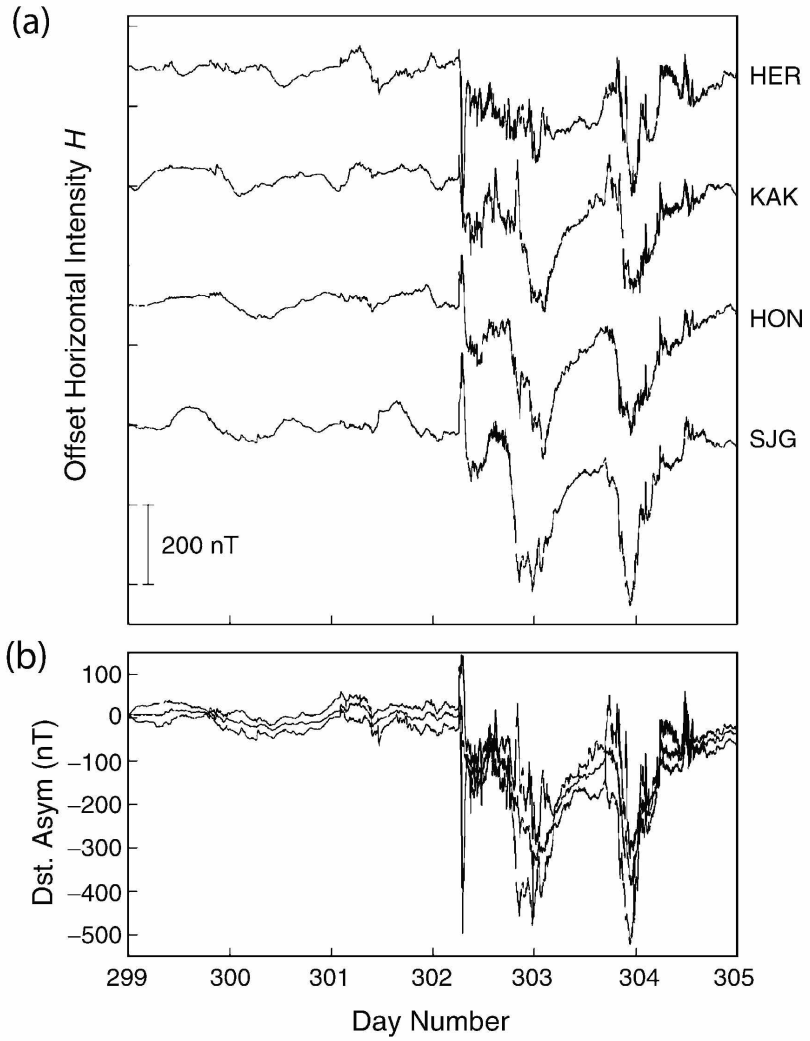

Figure 2.10. Effects of a magnetic storm as recorded in the hourly D_{st} index values with magnetograms from four near-equatorial geomagnetic observatories [*Love and Remick*, 2007].

increase in the D_{st} index. This is known as the storm sudden commencement. Following the initial phase a rapid and highly disturbed decrease begins and D_{st} index reaches a minimum (the storm main phase). D_{st} returns to its pre-storm level during storm recovery phase.

AE, AL and AU index

During substorms, electrojets and the substorm current wedge are the primary sources of magnetic disturbances. The AE index is the auroral electrojet index which were defined by *Davis and Sugiura* [1966] to measure the strength of the auroral electrojets. This index provides information on the auroral activity which is obvious manifestation of a substorm. The horizontal component (H) of the magnetic field from 12 auroral-zone magnetic observatories are used to calculate AE, and the average value of H during the five magnetically quietest days is subtracted. The AU index is

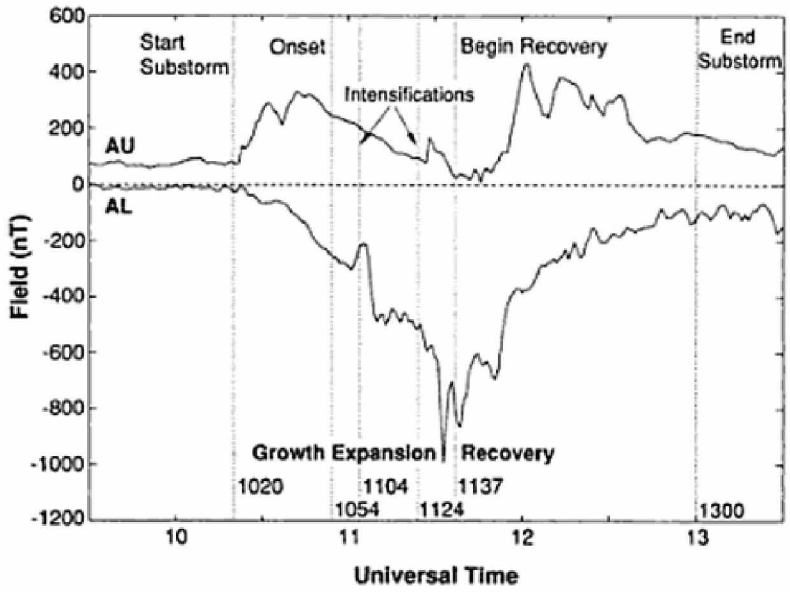

Figure 2.11. Three substorm phases in terms of the AU and AL indices [*McPherron and Manka*, 1985].

defined as the maximum positive disturbance and AL is the minimum disturbance. The difference is defined as $AE = AU - AL$.

Figure 2.11 shows AU and AL indices during a substorm [*McPherron and Manka*, 1985]. The three substorm phases (growth, expansion, and recovery) can be identified by changing in the slope of the AL index trace. When AU and AL are slowly growing, the time interval is the growth phase of the substorm. The onset of the substorm expansion phase is often signaled by a sudden increase of AL. During expansion phase, AL index reaches a minimum. The magnitude of AL index begins to decrease during the recovery phase [*McPherron and Manka*, 1985].

$\mathbf{K}_p$ index

The planetary K_p index represents the geomagnetic disturbance levels. This is derived from 3 h measurements of the K index obtained from 13 geomagnetic observatories located between 44° and 60° magnetic latitudes. The K index is designed to measure the range of irregular and rapid, storm-time magnetic activity. The K_p index measures the deviation of the most disturbed H-component of the magnetic field on worldwide observatories. The average value obtained from every station provides the global K_p index. The K_p index varies from 0 to 9 with plus and minus designations given between two intervals (for example, 1-, 1, 1+) [*Parks*, 2004]. Higher numbers indicate more intense disturbances.

2.3 Motivation and Outline of the Dissertation

The Earth's dayside magnetopause provides us the most proximity for investigating important dynamic processes. Magnetic reconnection at the dayside magnetopause is one of most important processes that efficiently transfer mass, momentum and energy from the solar wind to the Earth's magnetosphere. Magnetic reconnection at the magnetopause is usually asymmetric since the plasma density on the magnetosheath side is much higher than that on the magnetospheric side of the magnetopause and the magnetic field strength on the magnetospheric side is often stronger than that on the magnetosheath side. The asymmetric properties of the plasma and magnetic field at the magnetopause may lead the asymmetric reconnection geometry. However, what is the controlling factor that leads to the asymmetric reconnection geometry remains unclear.

The cold dense plasma, originated either directly from the ionosphere or from the plasmasphere, has often been observed near the dayside magnetopause. The plasmaspheric plumes and ionospheric outflows may play an important role in the reconnection process since they affect the plasma properties on the magnetospheric side of the magnetopause. Observations of cold dense plasma (plasmaspheric plume or ionospheric outflow) at different locations in the magnetosphere have been studied. However, there is no study on the characteristics of both plasmaspheric plumes and ionospheric outflows near the magnetopause. In addition, the role played by cold dense plasmas in the solar wind-magnetosphere coupling is still under debate. This dissertation investigates the characteristics and behavior of the cold dense ions observed at the dayside magnetopause and their effects on magnetic reconnection. The occurrence rates of the plasmaspheric plume and ionospheric outflow and their dependence on the solar wind/IMF condition are studied as well.

This dissertation addresses the following outstanding questions:

1. What is the controlling factor that leads to the asymmetric reconnection geometry at the magnetopause?

2. What are the characteristics (density and distribution of the location) of the plasmaspheric plume and ionospheric outflow observed near the dayside magnetopause?

3. Do the occurrence rates of the plumes and outflows depend on the geomagnetic activity and the solar wind/IMF conditions?

4. What is the role played by cold dense plasmas in the solar wind-magnetosphere coupling?

5. What is the behavior of the cold dense ions during magnetic reconnection?

This dissertation is organized as follows: Chapter 1 introduces the solar-terrestrial environments. Chapter 2 gives a brief introduction to dynamic process such as magnetic reconnection and

geomagnetic activities. Chapter 3 describes the instrumentation of the Cluster mission focusing on the data from CIS, RAPID, EFW, PEACE, STAFF, and FGM instruments onboard Cluster spacecraft. The analysis methods utilized in this research focuses on the Walén test, Minimum Variance Analysis, the Multi-spacecraft timing method, and the curlometer technique that are introduced in Chapter 4. In Chapter 5, controlling factors for asymmetric reconnection and the behaviors of the cold plasmaspheric ions during reconnection are discussed. Chapter 6 describes the existence and the characteristics of the asymmetric ionospheric outflows observed from Cluster 3 spacecraft near the dayside magnetopause. The comparison between the characteristics of the plasmaspheric plumes and the ionospheric outflows are investigated and the occurrence rates of two populations depending on the geomagnetic activity and solar wind/IMF conditions are discussed in Chapter 7. Chapter 8 contains the conclusions of the dissertation and future work.

Chapter 3
Cluster Mission and Instruments onboard

The European Space Agency's Cluster mission is designed to study detailed spatial and temporal characteristics of various regions of the Earth's magnetosphere, the interaction between the solar wind and the Earth's magnetosphere and ionosphere, and near-Earth solar wind plasma [*Escoubet et al.*, 1997; *Escoubet et al.*, 2001]. The Cluster mission consists of four identical satellites. The four-identical Cluster spacecraft were given names of Latin American dances (Rumba, Salsa, Samba and Tango). The four-point Cluster mission covers the main regions of the magnetosphere (solar wind, bow shock, magnetopause, magnetosheath, polar cusp, plasmasphere, magnetotail and auroral zone) depending on the configuration of the orbit. The four identical satellites flying in a tetrahedral configuration provide outstanding results on the three dimensional distributions of plasma and waves which allows us to study the small- and medium-scale structures of the magnetosphere and to derive important physical quantities (e.g., current density, plasma density and pressure gradients). The Cluster mission was launched in July 16 and August 9, 2000 and reached the final polar orbits with an apogee of 19.6 R_E and a perigee of 4 R_E. The mission will be extended until the end of 2018.

Each Cluster spacecraft carries 11 identical instruments. The Cluster data are available at Cluster Science Archive (CSA) website (http://www.cosmos.esa.int/web/csa). Data from the following instruments onboard Cluster were used in this dissertaion: CIS, FGM, PEACE, RAPID, EFW, STAFF and WHISPER. Most data used in this dissertation is averaged over one spin (4 s resolution). A brief description of these instruments are presented in the following sections.

3.1 Cluster Orbits and Configuration

The orbits of the Cluster spacecraft have a 360° coverage of the magnetosphere every year with a perigee at 4 R_E, an apogee at 19.6 R_E, and an inclination of 90° (Figure 3.1). The orbital period is 57 hours. The separation distances between the four spacecraft (the size of the tetrahedral configuration of the four spacecraft) vary from 200 km in the cusp to 18000 km in the magnetotail. It is capable of studying the three-dimensional structures in key regions of the terrestrial magnetosphere (bow shock, magnetosheath, magnetopause, polar cusp, magnetotail, and the auroral zone) with high time resolution.

Orbital dynamics allow changing of a constellation throughout a complete orbit (Figure 3.2). When Cluster crosses the dayside magnetopause (or the polar cusps), a perfect tetrahedron is constituted over the northern and southern cusp (Figure 3.2a). The spacecraft configuration is still close to a tetrahedron throughout the solar wind and the magnetosheath. The spacecraft follows

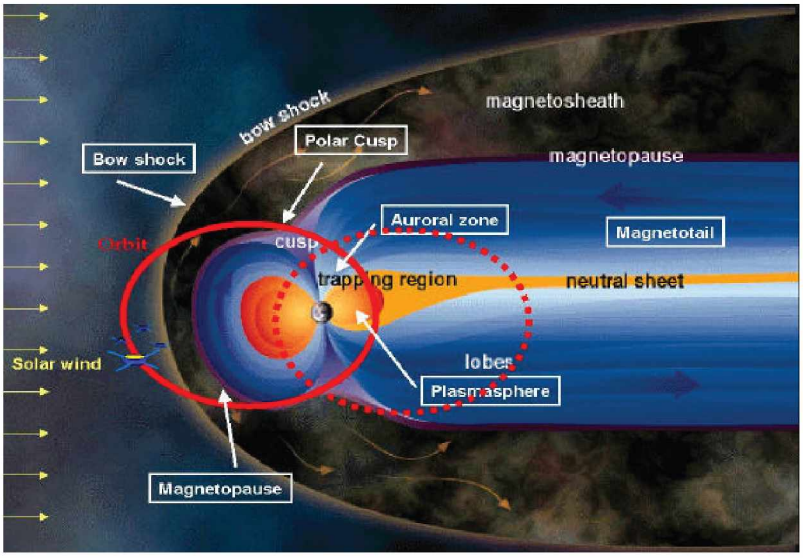

Figure 3.1. Orbits of the Cluster spacecraft and key regions in the magnetosphere. Credit: ESA

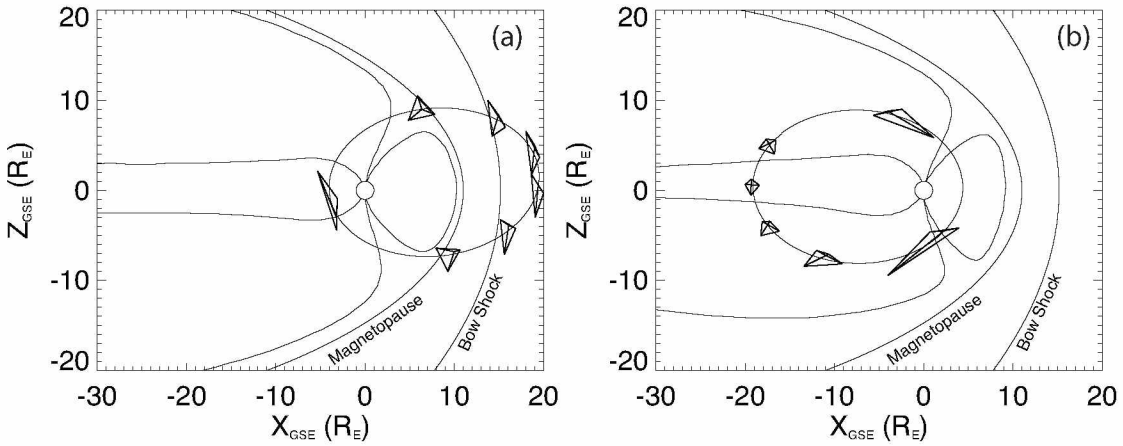

Figure 3.2. Cluster orbits and the tetrahedral configurations in GSE $X-Z$ plane during (a) dayside magnetopause crossing and (b) tail crossing [*Escoubet et al.*, 2001].

each other along the same orbit in the auroral zone (like a string of pearls) near perigee, which allows us to study temporal variations.

When the Cluster spacecraft crosses the magnetotail (Figure 3.2b), a perfect tetrahedron is formed in the plasma sheet near the apogee and the configuration becomes elongated in the mid-altitude cusp. Both the separation and the shape of the constellation change based on the complex constellation maneuvers.

3.2 Instruments onboard Cluster

3.2.1 CIS

The CIS (Cluster Ion Spectrometer) instrument measures full three-dimensional ion distributions of cold and hot ions from the solar wind, the magnetosheath, the magnetosphere, and the ionosphere with good angular, mass, and energy resolutions [*Rème et al.*, 2001]. The CIS experiment consists of two different sensors: a Hot Ion Analyser (HIA) sensor and a time-of-flight ion COmposition and DIstribution Function (CODIF) sensor. The CIS instrument on Cluster 2 (Salsa) is not operating.

The HIA instrument provides a full 3D distribution of the ions (5 eV/e to 32 keV/e) in every 4 s as scanning the entire 4 π steradian solid angle within one spin of the spacecraft (4 s). HIA offers a high angular resolution (5.6°$\times$ 5.6°), which is adequate for solar wind measurements and ion-beam, but, does not offer mass resolution. The CODIF instrument offers 3D distribution functions of the major ion species, including H^+, He^{++}, He^+, and O^+ ions with a high-sensitivity and a mass resolution. CODIF covers the energy range between the energies as low as the spacecraft potential and ~38 keV/e with a mass per charge composition and medium angular resolution (22.5° $\times$ 10.25°). The plasma moments (ion density, temperature and flow velocity) are calculated from integrating over the ion distribution function.

Figure 3.3 shows ion energy fluxes in all of the plasma regions encountered along the Cluster orbit. This indicates that the ClS instruments are capable of obtaining diverse characteristics of plasma, which have a large dynamic flux range. The main features and parameters of the HIA and CODIF sensors are summarized in Table 3.1.

3.2.2 FGM

The Fluxgate Magnetometer (FGM) provides accurate measurements of magnetic field vectors at high time resolution (up to 67 vectors/s) [*Balogh et al.*, 2001]. FGM contains two tri-axial fluxgate magnetic field sensors mounted on one of the two radial booms. One of the magnetometer sensors is located at the end of the two radial booms (outbound); the other is at 1.5 m from the end of the boom (inbound). This configuration minimizes the effect of the spacecraft background magnetic

Table 3.1. Performances of the CIS experiments [*Rème et al.*, 2001]

Analysers	HIA	CODIF
Energy Range	~5 eV/e – 32 keV/e	~0 – 38 keV/e
Time Resolution 2D (ms)	62.5	125
Time Resolution 3D (s)	4	4
Mass Resolution (M/δM)	–	~4–7
Angular Resolution	~5.6°×5.6°	~11.2°×22.5°
Geometrical Factor (cm^2sr keV/keV)	1.9×10^{-4} for one half	1.9×10^{-2} for one half
	4.9×10^{-3} for the other half	2.1×10^{-4} for the other half
Dynamics $(cm^2 sec\ sr)^{-1}$	10^4 – 2×10^{10}	3×10^3 – 3×10^9

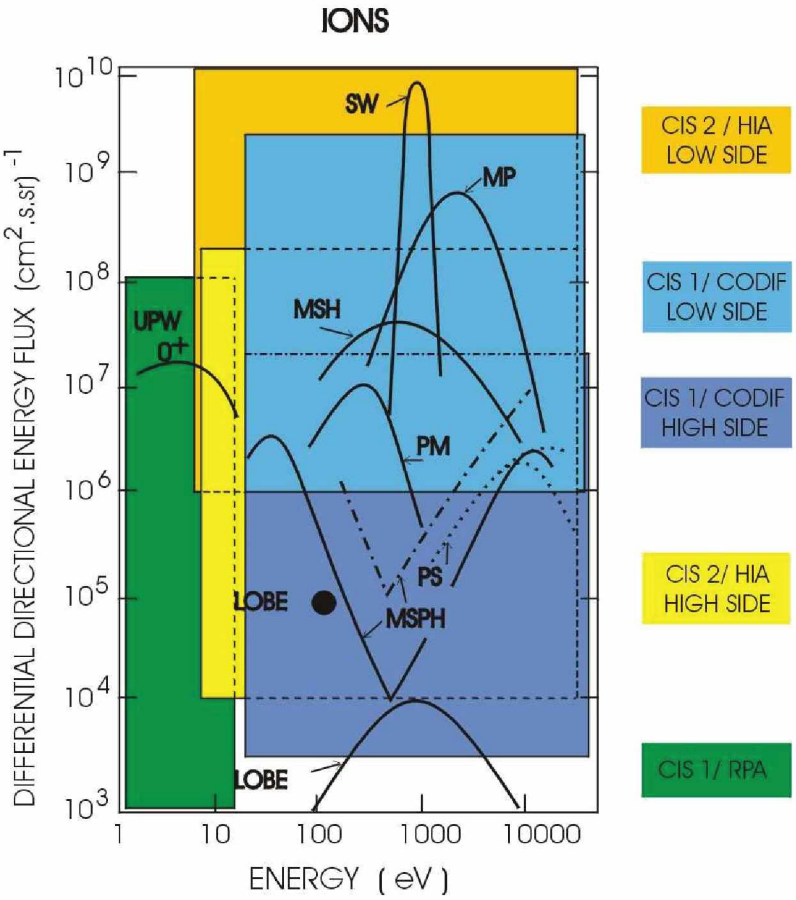

Figure 3.3. Representative ion fluxes in the plasma regions: the solar wind (SW), the magnetopause (MP), the magnetosheath (MSH), the plasma mantle (PM), the magnetosphere (MSPH), the plasma sheet (PS), and the low and the upwelling ions (UPW) [*Rème et al.*, 2001].

Table 3.2. Parameters of the PEACE sensors [*Johnstone et al.*, 1997]

Sensor	HEEA	LEEA
Energy Range	0.59 eV to 26.4 keV	0.59 eV to 26.4 keV
Energy Resolution (FWHM)	0.165 ± 0.007	0.127 ± 0.006
Field of view: polar	180°	180°
Field of view: azimuthal	5.27° ± 0.20°	2.79° ± 0.20°
Angular resolution: polar	3.75°, 15°	3.75°, 15°
Energy sweeps per spin	16, 32, or 64	16, 32, or 64
Angular resolution: azimuthal	22.5°, 11.25°, 5.625°	22.5°, 11.25°, 5.625°
Geometry factor, per 15° zone	6.0×10^{-8} m^2sr eV/eV	1.6×10^{-8} m^2sr eV/eV

field. Both sensors are used to obtain the three components of the magnetic field vectors in flight. Simultaneous four-point magnetic field measurements from the four Cluster spacecraft provide information about the geometry and structure of discontinuities and current density vector.

3.2.3 PEACE

The Plasma Electron and Current Experiment (PEACE) instrument is designed to measure the three dimensional velocity distribution of electrons in the energy range from 0.59 eV to 26.4 keV [*Johnstone et al.*, 1997]. The PEACE instrument is capable of measuring the low-energy (< 10 eV) electron velocity distributions with a high quality. Each PEACE instrument contains two sensor heads, LEEA (low-energy electron analyser) and HEEA (high-energy electron analyser). These sensors are mounted on opposite sides of the spacecraft. Thus, the instantaneous field of view of one sensor head is the same as that measured by the other sensor head in half a spacecraft rotation (2 s) later. Therefore, the fastest time resolution for PEACE to obtain complete electron distributions is 2 s.

The full PEACE energy range is divided into 88 different energy levels. Full coverage of the energy can be achieved by using both sensors together, since each sensor cannot cover the full energy range. LEEA admits less electrons than HEEA. HEEA detects more diffused electrons with energies 34 eV–26.5 keV [*Owen et al.*, 2001]. LEEA specializes in the measurement of the lower end of the electron energy spectrum (0.59 eV–9.45 eV) and has the smaller geometric factor. The smaller geometric factor is appropriate for the high fluxes to be found at low energy. Parameters of the PEACE instrument are summarized in Table 3.2 [*Johnstone et al.*, 1997].

3.2.4 RAPID

The Research with Adaptive Particle Imaging Detectors (RAPID) instrument is an advanced imaging spectrometer for the analysis of suprathermal plasma distributions [*Wilken et al.*, 2001]. The

Table 3.3. Characteristic parameters of the RAPID spectrometer [*Wilken et al.*, 2001]

Energy ranges:	Hydrogen	30-1500 keV
	Helium	100-1500 keV
	CNO	105-1500 keV
	Electrons	20-400 keV
Mass range:		1, 4, 12-16, 28-56 amu
Resolution (A/dA):	Oxygen	4
Field-of-view:	IIMS (Ions)	$\pm$ 3°×180°
	IES (Electrons)	$\pm$ 17.5°×180°
Geometry factor:	IIMS	2.6×10^{-2} cm^2·sr
(for 180°)	IES	2.0×10^{-2} cm^2·sr

RAPID instrument provides three-directional particle fluxes of four species in the following energy ranges: from ~20 keV to 400 keV for electrons, 30–1500 keV for hydrogen, 29–1500 keV for Helium ions, and 26–1500 keV for CNO (heavy ions).

RAPID consists of two sets of detectors, the IIMS (Imaging Ion Mass Spectrometer) for ions and the IES (Imaging Electron Spectrometer) for electrons. The IIMS contains three identical sensor heads. Each ion sensor head has a Time of Flight (TOF) and energy detection system. The TOF system determines the particle velocity (v) by measuring the flight time traveling a known distance in the detector geometry. The energy detection system measures the energy of the particles. The different mass (m) of the particles can be identified using the relationship between the energy (E) and velocity (v), $E = \frac{1}{2}mv^2$ [*Wilken et al.*, 2001]. The ion spectral counts are sorted into 12 polar angle segments, 8 energy bins, 16 azimuthal sectors, and 3 mass ranges, but only 9 polar segments for the electron spectral counts. The IES detects electrons from ~20 keV to 400 keV. The characteristic parameters of the RAPID instrument are listed in Table 3.3 [*Wilken et al.*, 2001].

3.2.5 EFW

The Cluster Electric Field and Wave (EFW) instrument measures the electric field and density fluctuations [*Gustafsson et al.*, 2001]. The instrument includes two pairs of spherical probes on wire booms in the spin plane with a separation of 88 m between the probes. This allows us to obtain spin plane components (E_x and E_y) of the quasi-static electric field vector in the range from 0.3 to 700 mV/m with 0.1 ms time resolution. The spacecraft potential from two pairs of spherical probes to the spacecraft is used to estimate the electron density in the range of 10^{-2}– 10 cm^{-3} with 0.2 s time resolution [*Gustafsson et al.*, 2001].

3.2.6 STAFF

The STAFF (Spatio-Temporal Analysis of Field Fluctuations) instrument is designed to measure the rapid electromagnetic fluctuations [*Cornilleau-Wehrlin et al.*, 1997]. The instrument consists of two parts: (1) A three-axis search coil magnetometer mounted at the end of a 5 m long boom measures the magnetic field components of the electromagnetic fluctuations in the frequency range up to 4 kHz. (2) A spectrum analyzer measures auto- and cross correlation between magnetic and electric field components. The STAFF instrument provides the total power of the magnetic field in three frequency ranges, 1–10 Hz, 10–180 Hz, and 180–4000 Hz.

3.2.7 WHISPER

The WHISPER (Whisper of HIgh frequency and Sounder for Probing Electron density by Relaxation) instrument is a relaxation sounder that provides two data sets: the total electron density which is obtained from an active radio frequency technique and the spectrum of natural plasma emissions in the high frequency range from ∼2 to 80 kHz. The principle of WHISPER is that an emitter sends a series of pulses in the plasma and a receiver observes a strong resonance when the pulse frequency matches one of characteristic plasma frequencies. The observed resonances in a sounder spectrum determine the electron plasma frequency, F_p (kHz). Thus, the total electron density (N_e) can be derived from the relation,

$$N_e[cm^{-3}] = F_p^2/81 \tag{3.1}$$

The absolute electron density variations with a sufficient time resolution (0.3–3 s) are in the range of 0.2–80 cm^{-3} [*Décréau et al.*, 2001].

Chapter 4
Analysis Methods

The Cluster mission with four identical spacecraft was designed to make simultaneous measurements at different locations. This allows us to do data analyses based on four-point measurements. This chapter introduces the main methods used in this dissertation: Walén test, minimum variance analysis (MVA), the multi-spacecraft timing method, and the curlometer technique. Minimum variance analysis of the magnetic field data allows us to estimate the invariant direction (the orientation of the structure) based on the physical constraint $\nabla \cdot \mathbf{B} = 0$. The normal vector and the propagation velocity of the observed boundary along the normal direction are obtained by using the timing method. The current density is obtained from the four-point magnetic field vectors using the curlometer method. Therefore, the $\mathbf{j} \times \mathbf{B}$ force density in the reconnection region can be calculated.

4.1 de Hoffmann-Teller Frame

A good de Hoffmann-Teller frame indicates that a process is approximately steady state. The de Hoffmann-Teller (HT) frame was first applied to a one-dimensional shock [*de Hoffman and Teller*, 1950]. The shock frame is a reference frame in which the shock is stationary. The velocity transformation can be used to transfer from the shock frame to another frame [*Kivelson and Russell*, 1995]. Figure 4.1(a) shows the normal incidence frame containing the shock normal $\hat{\mathbf{n}}$, the flow velocity $\mathbf{U}$, and the magnetic field $\mathbf{B}$. The subscripts u and d indicate the upstream and downstream sides of the shock, respectively. The upstream flow is parallel to the shock normal. There is a motional electric field ($\mathbf{E}_u$) that is perpendicular to both $\mathbf{U}_u$ and $\mathbf{B}_u$. This electric field is then parallel to the plane of the shock, $\mathbf{E}_u = -\mathbf{U}_u \times \mathbf{B}_u$, and can be made zero by adding a transformation velocity parallel to the shock plane. The transformation velocity from the normal incident frame is denoted by $\mathbf{V}_{HT}$ as shown in Figure 4.1(b). This frame is called the de Hoffman-Teller (HT) frame. The $\mathbf{V}_{HT}$ is the frame velocity vector (i.e. HT frame velocity).

The upstream flow velocity ($\mathbf{U}'_u$) is parallel to the upstream field ($\mathbf{B}_u = \mathbf{B}'_u$). All quantities are marked by a prime in the HT frame. The frame velocity vector can be written as

$$\mathbf{V}_{HT} = \mathbf{U}_u tan(\theta_{B_n}) \tag{4.1}$$

The transformed velocity can be written as

$$\mathbf{U}'_u = \mathbf{U}_u - \mathbf{V}_{HT} \tag{4.2}$$

The motional electric field vanishes in this HT frame.

$$\mathbf{E}' = -\mathbf{U}'_u \times \mathbf{B}'_u = 0 \tag{4.3}$$

Equations 4.2 and 4.3 can be combined.

$$\mathbf{V}_{HT} \times \mathbf{B}_u = \mathbf{U}_u \times \mathbf{B}_u \tag{4.4}$$

Solving for $\mathbf{V}_{HT}$, we get

$$\mathbf{V}_{HT} = \frac{\hat{\mathbf{n}} \times (\mathbf{U}_u \times \mathbf{B}_u)}{\hat{\mathbf{n}} \cdot \mathbf{B}_u} \tag{4.5}$$

Because the motional electric field is zero, the motion of the upstream particles is very simple: gyrational motion around the magnetic field and motion parallel to it.

Sonnerup and Wang [1987] developed a least-squares analysis technique to determine the HT frame velocity from data by a single spacecraft. To obtain $\mathbf{V}_{HT}$ from measurements, we need to find a frame in which the mean square of the electric field is as small as possible. This is accomplished by minimizing the quantity D which is the object function with respect to the frame velocity $\mathbf{V}$,

$$D(\mathbf{V}) = \frac{1}{M}\sum_{m=1}^{M} |\mathbf{E}'^m|^2 = \frac{1}{M}\sum_{m=1}^{M} |(\mathbf{v}^m - \mathbf{V}) \times \mathbf{B}^m|^2 \tag{4.6}$$

where $\mathbf{v}^m$ and $\mathbf{B}^m$, m = 1, 2, ...M, are the measurements of plasma bulk velocities and magnetic fields, respectively. The minimization condition $\nabla_{\mathbf{V}} D = 0$ follows linear equation for $\mathbf{V}_{HT}$.

$$K_0 \mathbf{V}_{HT} = \langle K^m \mathbf{v}^m \rangle \tag{4.7}$$

$K_0 \equiv \langle K^m \rangle$ is assumed to be non-singular and the angle brackets denote an average of an enclosed quantity given a set of M measurements. The solution is

$$\mathbf{V}_{HT} = K_0^{-1} \langle K^m \mathbf{v}^m \rangle \tag{4.8}$$

where K^m is the matrix of projection (P^m) into a plane perpendicular to $\mathbf{B}^m$.

$$K^m_{\mu\nu} = B^{m^2} \left(\delta_{\mu\nu} - \frac{B^m_\mu B^m_\nu}{B^{m^2}} \right) \equiv B^{m^2} P^m_{\mu\nu} \tag{4.9}$$

The result is often applied to a Walén test. Figure 4.2 shows a planar flow and field configuration for a shock-like structure. The HT frame velocity ($\mathbf{V}_{HT}$) and the velocity of motion of the discontinuity along the normal, $\mathbf{V}_{HT} \cdot \hat{\mathbf{n}} = u_n$ are shown. The existence of an HT frame indicates that a quasi-

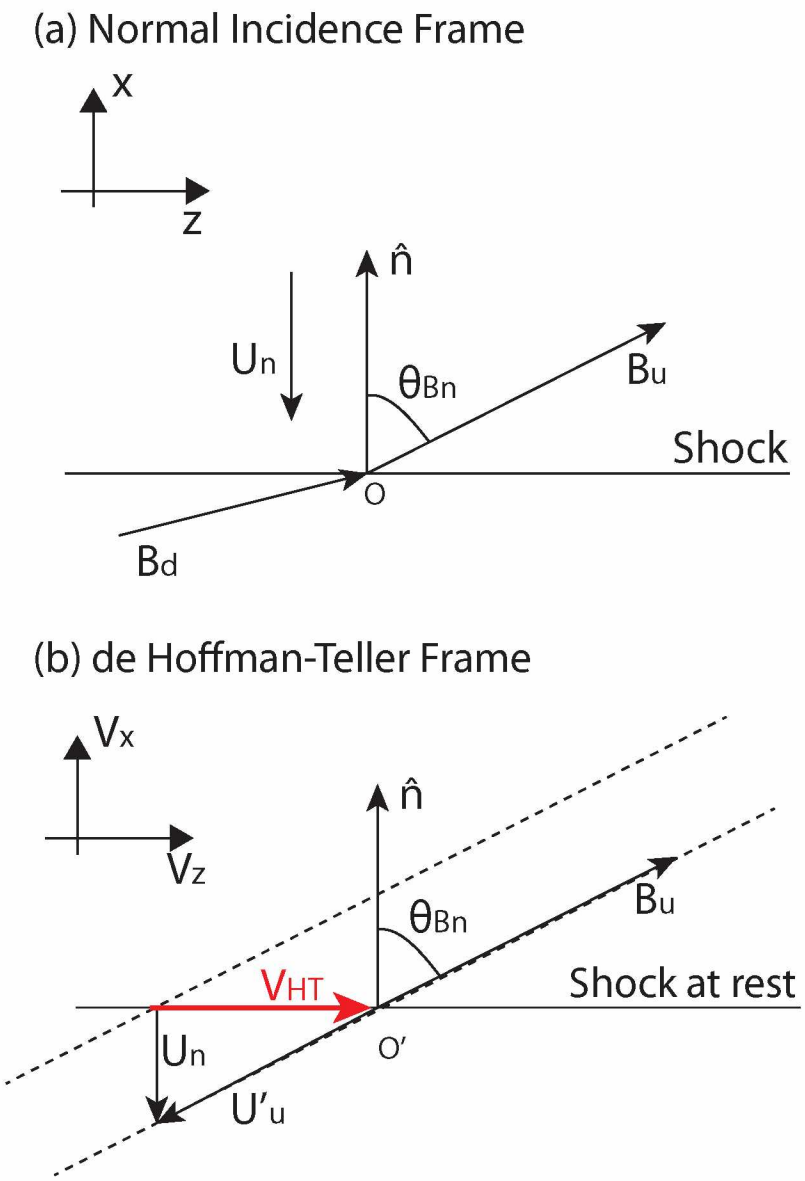

Figure 4.1. Simple illustrations for (a) the normal incidence frame and (b) the de Hoffman-Teller frame. The HT frame is shown in velocity coordinate system.

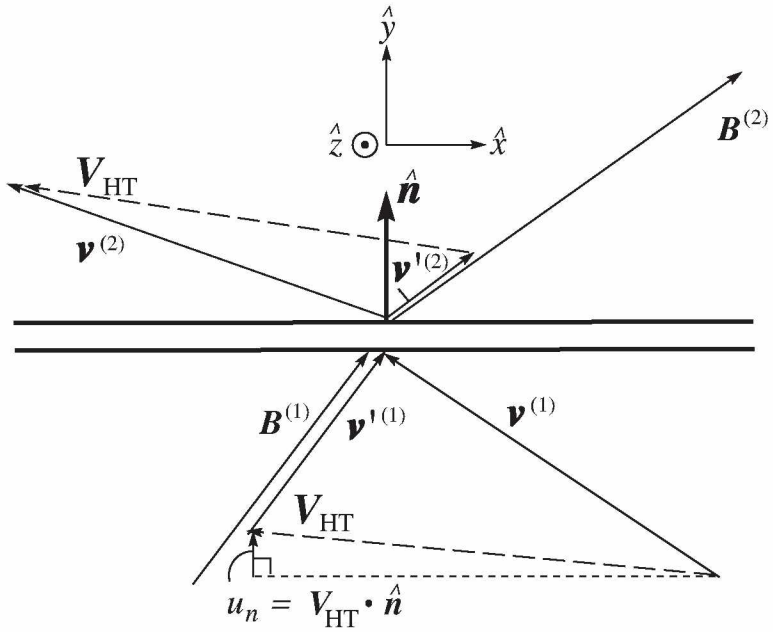

Figure 4.2. A simple planar illustration showing measured magnetic fields, $\mathbf{B}^{(1)}$ and $\mathbf{B}^{(2)}$, velocities, and $\mathbf{v}^{(1)}$ and $\mathbf{v}^{(2)}$ in the spacecraft frame. $\mathbf{V}_{HT}$ and u_n represent the HT frame velocity and its normal component, respectively. $\mathbf{v}'^{(1)}$ and $\mathbf{v}'^{(2)}$ are the plasma velocities in the HT frame [*Khrabrov and Sonnerup*, 1998].

stationary pattern of magnetic field is present. The usage of the HT frame allows us to identify the passage of such a moving quasi-static structure and the HT frame is suitable for the Walén test.

4.2 Walén Test

Direct evidence of the magnetic reconnection can be found in the existence of the high-speed flow away from the diffusion region which satisfies the Walén relation [*Paschmann et al.*, 1979]. MHD theory predicts that the accelerated plasma flow generated by reconnection is Alfvénic in the HT frame, which is called the Walén relation. The plasma velocities are $\mathbf{v}'^m \equiv \mathbf{v}^m - \mathbf{V}_{HT}$ in the HT frame and the local Alfvén velocities ($\mathbf{V}_A^m$) are computed from the measured magnetic fields ($\mathbf{B}^m$) and total mass densities (ρ^m, assuming all particles are H^+), $m = 1, 2, ...M$,

$$\mathbf{V}_A^m = \frac{\mathbf{B}^m}{\sqrt{\mu_0 \rho^m}} \tag{4.10}$$

The anisotropy-corrected local Alfvén velocity is $\mathbf{V}_A = \mathbf{B}[(1-\alpha)/(\mu_0\rho)]^{1/2}$ when considering the effect of pressure anisotropy $\alpha = (p_\parallel - p_\perp)\mu_0/B^2$. The Walén test is to determine whether the high-speed flow is Alfvénic by generating a component-by-component scatter plot of the plasma

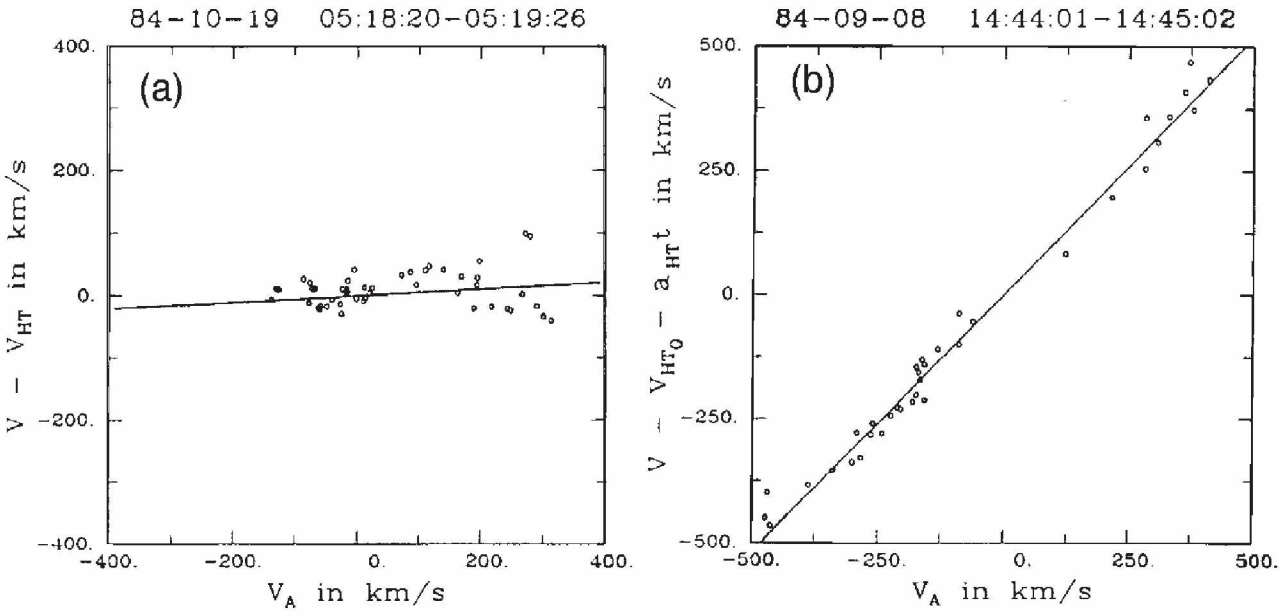

Figure 4.3. (a) Walén plot, the plasma velocities ($\mathbf{V} - \mathbf{V}_{HT}$) in the HT frame as a function of the components of the Alfvén velocity ($\mathbf{V}_A$) for AMPTE/IRM magnetopause crossing on October 19, 1984; (b) same format but including acceleration of HT frame for crossing on September 8, 1984 [*Khrabrov and Sonnerup*, 1998].

velocities in the HT frame, $\mathbf{v}'$, and the Alfvén velocities, $\mathbf{V}_A$.

$$\mathbf{v}' = \pm \mathbf{V}_A \tag{4.11}$$

The positive (negative) sign in the relation indicates that the normal components of the magnetic field (B_n) and plasma velocity (v_n) have the same (opposite) signs.

Figure 4.3 shows examples of the Walén test for two magnetopause crossings by the AMPTE/IRM spacecraft. As shown in Figure 4.3(a), the Walén test is not successful since the plasma flow velocities ($\mathbf{V} - \mathbf{V}_{HT}$) in the HT frame are much smaller than the Alfvén velocities. This indicates that reconnection did not occur during this magnetopause crossing. By contrast, Figure 4.3(b) shows the data points fall along one of the diagonals in the plot indicating that the Walén relation is satisfied. The HT frame was assumed to be accelerating for a good agreement. It can be drawn that the magnetopause has a structure of rotational discontinuity. A linear relation, $\mathbf{v}' = \mathbf{V} - \mathbf{V}_{HT} = \pm \mathbf{V}_A$, in the range of $\pm(0.8$–$1.0)$ is interpreted as an indication that magnetopause reconnection is occurring (rotational discontinuity). The existence of a good HT frame for a magnetopause crossing is a necessary, but not sufficient condition for a rotational discontinuity.

4.3 Minimum Variance Analysis

The purpose of minimum variance analysis (MVA) is to determine the normal direction and velocity of a one-dimensional structure such as a current layer, wave front, or other transition layer in a plasma. This technique is applied to magnetic field vector data measured from a single spacecraft as it traverses a current layer. MVA is based on the one-dimensional (1-D: $\partial/\partial x = 0, \partial/\partial y = 0$) model of the layer so that the field component B_z is independent of z for the divergence of $\mathbf{B}$, $\nabla \cdot \mathbf{B} = \partial B_z/\partial z = 0$. The normal component is continuous across the infinite, thin current layer. To determine the normal vector ($\hat{\mathbf{n}}$), three distinct vector measurements ($\mathbf{B}^{(1)}, \mathbf{B}^{(2)}$, and $\mathbf{B}^{(3)}$) are needed. The difference vectors between ($\mathbf{B}^{(1)} - \mathbf{B}^{(2)}$) and ($\mathbf{B}^{(2)} - \mathbf{B}^{(3)}$) are tangential to the layer. Thus, the cross product between those vectors is along the normal vector assuming that they are not colinear ($\mathbf{B}^{(1)} \cdot \hat{\mathbf{n}} = \mathbf{B}^{(2)} \cdot \hat{\mathbf{n}} = \mathbf{B}^{(3)} \cdot \hat{\mathbf{n}}$).

The normal field component is then

$$B_n = \mathbf{B} \cdot \hat{\mathbf{n}} = \pm \frac{\mathbf{B}^{(1)} \cdot (\mathbf{B}^{(2)} \times \mathbf{B}^{(3)})}{|(\mathbf{B}^{(1)} - \mathbf{B}^{(2)}) \times (\mathbf{B}^{(2)} - \mathbf{B}^{(3)})|} \tag{4.12}$$

where the normal vector,

$$\hat{\mathbf{n}} = \pm \frac{(\mathbf{B}^{(1)} - \mathbf{B}^{(2)}) \times (\mathbf{B}^{(2)} - \mathbf{B}^{(3)})}{|(\mathbf{B}^{(1)} - \mathbf{B}^{(2)}) \times (\mathbf{B}^{(2)} - \mathbf{B}^{(3)})|} \tag{4.13}$$

For real transition layers that have 2-D or 3-D internal structures, $\hat{\mathbf{n}}$ is determined by minimization of

$$\sigma^2 = \frac{1}{M} \sum_{m=1}^{M} |(\mathbf{B}^m - \langle \mathbf{B} \rangle) \cdot \hat{\mathbf{n}}|^2 \tag{4.14}$$

where the average $\langle \mathbf{B} \rangle \equiv \frac{1}{M} \sum_{m=1}^{M} \mathbf{B}^m$ ($m = 1, 2, 3, ...M$) and the normalization constraint $|\hat{\mathbf{n}}|^2 = 1$. Using a Lagrange multiplier (λ), the magnetic variance matrix can be written as

$$\sum_{\nu=1}^{3} M^B_{\mu\nu} n_\nu = \lambda n_\nu \tag{4.15}$$

where the subscripts $\mu, \nu = 1, 2, 3$ define cartesian components x, y, and z and $M^B_{\mu\nu} \equiv \langle B_\mu B_\nu \rangle - \langle B_\mu \rangle \langle B_\nu \rangle$. The λ values are the eigenvalues λ_1, λ_2 and λ_3 (in order of decreasing magnitude) of $M^B_{\mu\nu}$, which are all real, and the corresponding eigenvectors x_1, x_2 and x_3 are orthogonal. The three eigenvectors (x_1, x_2 and x_3) correspond the directions of maximum, intermediate, and minimum variance of the magnetic field along each vector.

The normal direction of the transition layer can be estimated using the eigenvector (x_3) corresponding to the smallest eigenvalue, λ_3. The maximum and intermediate variance directions (x_1 and x_2) are tangential to the current sheet. In the application to the dayside magnetopause, the

maximum variance eigenvector x_1 and the minimum variance eigenvector x_3 can be chosen to be the northward and outward directions from the Earth, respectively. The ordered set x_1, x_2 and x_3 is similar to the local coordinate system, called LMN coordinate system which was introduced by *Russell and Elphic* [1979]. The directions of L, M and N are the maximum, intermediate, and minimum variance directions, respectively. For an example of the magnetopause as the rotational discontinuity in the boundary normal coordinate system, the maximum variance direction L represents the northward direction along the magnetospheric field, N corresponds to the direction along the magnetopause normal, and M completes the coordinates.

The matrix and the variance are non-degenerate when the three eigenvalues of the variance matrix are distinct. There is number of cases where near degeneracy occurs when two eigenvalues are nearly the same. The uncertainty in the corresponding eigenvalues for these cases is large so that the eigenvalue ratio (intermediate to minimum eigenvalues) should be large in order to obtain a valid direction of normal to the transition layer.

4.4 Multi-Spacecraft Timing Method

The purpose of the multi-spacecraft timing method, referring to as the time-delay method and/or triangulation method, is to obtain the normal vector $\hat{\mathbf{n}}$ and the velocity along the normal direction (V_n) of an observed boundary [*Schwartz*, 1998]. If the same boundary passes the four Cluster satellites, four measurements allow us to construct the boundary normal and the propagation velocity along the normal direction. Assuming a planar boundary moves with a constant velocity, the relation between the normal vector $\hat{\mathbf{n}}$ and the propagation velocity along the normal direction V_n can be written as

$$V_n = \frac{\mathbf{r}_{\alpha\beta} \cdot \hat{\mathbf{n}}}{t_{\alpha\beta}} \tag{4.16}$$

where $\mathbf{r}_{\alpha\beta}$ is the relative position vector between any spacecraft pair and $t_{\alpha\beta}$ is the time difference between this pair for the boundary. The timing method can be applied to various types of discontinuities such as the magnetopause, the bow shock, and the plasmapause. This method allows us to obtain the orientation and the velocity of a planar structure. It should be kept in mind that this method fails if the separation vectors of four satellites are large or the spacecraft are nearly coplanar.

4.5 Curlometer Technique

The curlometer method [*Robert et al.*, 1998] is to estimate the electric current density ($\mathbf{J}$) using the magnetic field data from the FGM instrument. This method uses the Ampere's law,

$$\mu_0 \mathbf{J} = \nabla \times \mathbf{B} \tag{4.17}$$

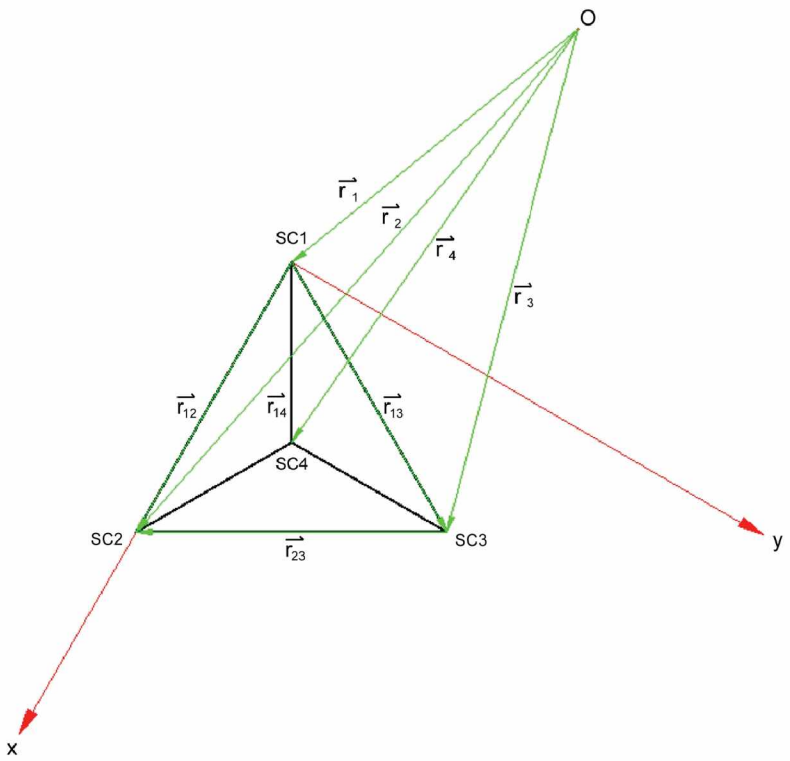

Figure 4.4. The configuration of the Cluster tetrahedron

to calculate the current density as treating that this current is a constant in the whole volume of the tetrahedron formed by the four spacecraft (see Figure 4.4). Equation 4.17 can be rewritten as

$$\mu_0 J_{ijk} \cdot (\Delta r_{ik} \times \Delta r_{jk}) = \Delta B_{ik} \cdot \Delta r_{jk} - \Delta B_{jk} \cdot \Delta r_{ik} \tag{4.18}$$

where i, j, and k are the number of satellites. J_{ijk} represents measured mean current normal to the surface made by the satellites i, j and k. $\Delta r_{ik} = r_i - r_k$ and $\Delta B_{ik} = B_i - B_k$ represent the distance and the magnetic field differences between respective satellites, respectively.

The two main assumptions of this method are that the current density is constant over the tetrahedron configuration and the magnetic field changes linearly (i.e., stationarity) over the transition layer. The parameter of $(\nabla \cdot \mathbf{B})/(\nabla \times \mathbf{B})$ allows us to estimate of the accuracy of the current density. A greater than 1 value of $(\nabla \cdot \mathbf{B}/\nabla \times \mathbf{B})$ indicates a bad estimation of the average current density (J_{av}), whereas $(\nabla \cdot \mathbf{B}/\nabla \times \mathbf{B}) \ll 1$ indicates a good estimation of J_{av} [*Robert et al.*, 1998].

Chapter 5
Behavior of Cold Ions during Asymmetric Magnetic Reconnection at the Magnetopause

5.1 Introduction

Magnetic reconnection is a universal process that converts stored magnetic energy into particle kinetic energy and produces changes in the magnetic topology. It is primarily invoked to transfer momentum and energy from the solar wind to the magnetosphere at Earth's magnetopause [*Dungey*, 1961; *Sonnerup et al.*, 1987]. If the magnitude of the magnetic field and the plasma density on both sides of the current sheet are similar, the magnetic reconnection is defined as symmetric reconnection [*Mozer et al.*, 2008; *Mozer and Pritchett*, 2009]. Symmetric reconnection is usually characterized by a quadrupolar out-of-plane magnetic field component and a bipolar normal electric field [*Øieroset et al.*, 2001; *Mozer et al.*, 2002].

At the dayside magnetopause, the solar wind plasma density is generally much higher than that inside the magnetosphere and the magnitude of the interplanetary magnetic field (IMF) is much weaker than that of the terrestrial field. Thus dayside reconnection occurring at the subsolar region is generally characterized by asymmetric plasma and magnetic field conditions. For reconnection occurring at the dayside subsolar region, the magnitude of the reconnecting magnetic field and plasma density may vary more than an order of the magnitude across the dayside magnetopause current layer, leading to the magnetic field and the plasma flow geometries being very different from those associated with symmetric reconnection. The scaling analyses for the reconnection rate, outflow speed, the density of the outflow, and the structure of the dissipation region during asymmetric magnetic reconnection have been investigated with different simulation models [*Pritchett and Mozer*, 2009; *Birn et al.*, 2008; *Borovsky and Hesse*, 2007] and theories [*Cassak and Shay*, 2007, 2008, 2009].

Magnetic topological changes are to be expected once the IMF on the magnetosheath side becomes magnetically connected to the magnetic field on the magnetospheric side and the accelerated plasma jets away from the reconnection region. The reconnection separatrix is defined as the field line connected to the X-line and it is located close to the electron edge which is a boundary of both transmitted and mirrored electrons, whereas the flow boundary is a boundary between inflow and the outflow jet and it approximately coincides with the ion edge. Electrons move much faster than ions while both electrons and ions convect with the magnetic field by the $\mathbf{E}\times\mathbf{B}$ drift, so the electron boundaries are more closely field-aligned than the ion boundaries. Two boundaries, the separatrix and the flow boundary, have been identified by taking into account kinetic effects during magnetic reconnection [*Øieroset et al.*, 2001; *Retinò et al.*, 2006; *Lindstedt et al.*, 2009; *Gosling et al.*, 1990a].

The topology of magnetic reconnection can be deduced from either the magnetic separatrix angles or the plasma flow boundary angles. Identifying the boundaries (the separatrix and the flow boundary) is important in order to obtain the angles of the separatrix and the flow boundary on both sides of the current sheet. *Xiao et al.* [2007] identified the separatrix by sharp variations in the elevation angle of the local magnetic field ($\theta_B \approx tan^{-1}(B_z/B_x)$). As illustrated in Figure 5.1, the separatrix angle $\theta \approx \theta_B$ (the elevation angle of the local magnetic field) at the separatrix since the magnetic field lines are approximately parallel near the separatrix [*Xiao et al.*, 2007].

Since the length (in the x-direction) and width (in the z-direction) of the diffusion region are related to the separatrix angle,

$$\frac{L_z}{L_x} \approx tan\theta \tag{5.1}$$

where L_z (L_x) are the half-width (length) of the diffusion region, the length of the diffusion region can be calculated if the width of the diffusion region is known (e.g., from best-fit to a Harris sheet model). In the *Xiao et al.* [2007] event, the length and width of the diffusion region are 460 km and 1680–2597 km, respectively. In addition, the magnetic reconnection rate can be calculated based on the mass conservation and the separatrix angle,

$$\gamma_{rec} \sim V_{in} = V_{out} \cdot (L_z/L_x) = V_A \cdot tan\theta \tag{5.2}$$

where V_{in} (V_{out}) is the inflow (outflow) speed and V_A is the asymptotic Alfvén speed. They found that the reconnection rate calculated this way is (0.09–0.30)V_A which is similar to the direct measurement of V_{in}.

Until now, few studies on the dayside reconnection have considered the plasma and energetic particle behaviors during asymmetric magnetic reconnection at the magnetopause. Energetic particles have been observed during magnetic reconnection events in various astrophysical environments, such as solar flares, the magnetotail, and the magnetopause [*Lin et al.*, 2003; *Øieroset et al.*, 2002; *Zhang et al.*, 2008]. Some studies have explored the acceleration mechanisms for the presence of the energetic ions in the reconnection region [*Speiser et al.*, 1981; *Cowley*, 1982; *Zong and Wilken*, 1998, 1999; *Zong et al.*, 2001]. However, different aspects of energetic particle behavior during symmetric and asymmetric reconnection are still little explored. On the other hand, cold and dense plasmaspheric plasma at the dayside magnetopause has been investigated by several studies [*Su et al.*, 2000; *Borovsky and Steinberg*, 2006; *Borovsky and Denton*, 2006; *Cowley*, 1982; *Gosling et al.*, 1990b; *André et al.*, 2010]. We find some important characteristics of the accelerated cold dense ions and their effect on the reconnection dynamics which is related to the previous observational and simulation studies [*Gosling et al.*, 1990b; *Borovsky and Denton*, 2006; *Borovsky et al.*, 2008].

Here we present Cluster observations of the magnetic reconnection event at the dayside magne-

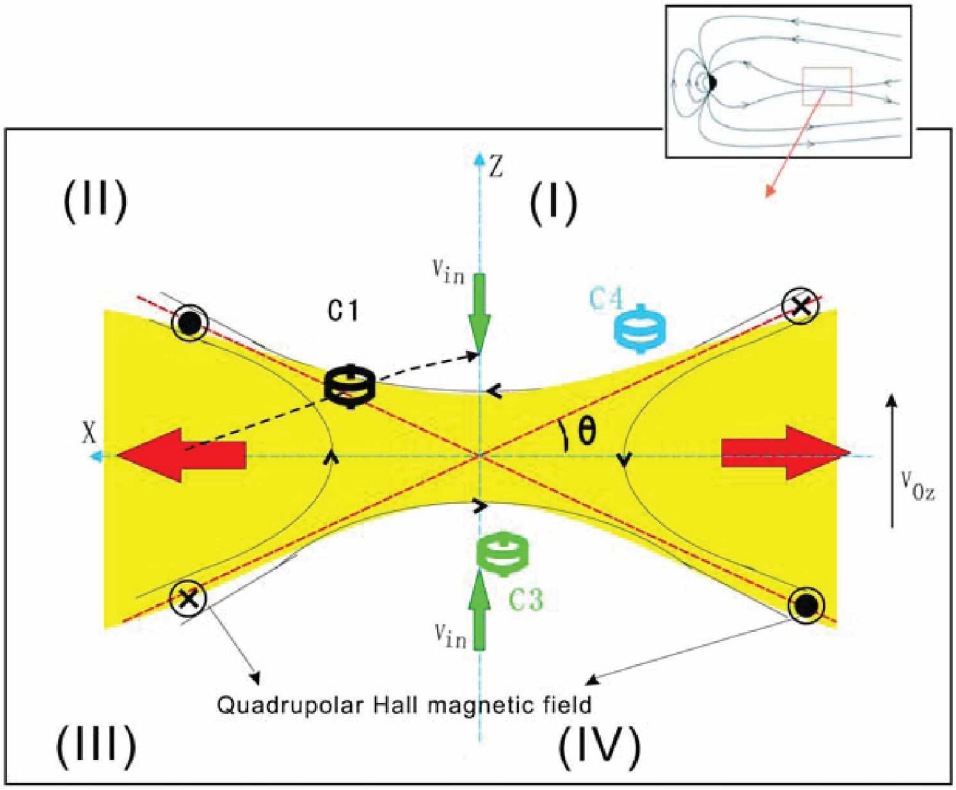

Figure 5.1. Geometry of the magnetic diffusion region encountered by the Cluster spacecraft in the magnetotail [*Xiao et al.*, 2007].

topause to illustrate the asymmetric reconnection topology with identification of the separatrices and flow boundaries on the magnetosheath and magnetospheric sides, and study the cold ion and energetic particle behaviors during asymmetric magnetic reconnection at the magnetopause. The outline of this chapter is as follows. In section 5.2, we describe the geometry of the magnetic reconnection and cold and energetic ion behaviors during reconnection. In section 5.3, we discuss the asymmetric reconnection geometry and effect of cold ions on the reconnection dynamics. Section 5.4 contains the summary and conclusions of this chapter.

5.2 Cluster Observations and Interpretation

Figure 5.2 illustrates the Cluster orbit from 18:00-20:00 UT on March 5, 2007. Cluster 3 (C3, green star) was located primarily inside the magnetosphere and crossed the magnetopause at (X, Y, Z) = (8.1, 1.3, 4.5) R_E in the *GSM* reference frame. While traveling outbound in the northern hemisphere, Cluster crossed the magnetopause several times and exited to the magnetosheath. The inner and outer red lines indicate the locations of the magnetopause and bow shock determined by the Fairfield model [*Fairfield*, 1971].

The separatrix can be identified by using electric field spectrograms. The first transmitted electrons may induce plasma instabilities which generate wave emissions. Hence the separatrix can be found as a boundary in wave activity features where the waves become more intense and broadband [*Retinò et al.*, 2006]. Similarly, *Lindstedt et al.* [2009] have defined the electron edge or separatrix on the magnetospheric side where the first magnetosheath electrons or parallel electrons with a typical energy of hundred of eV are observed. *Matsumoto et al.* [2003] have observed enhanced broadband electrostatic emissions, such as Electrostatic Solitary Waves (ESW) and Amplitude Modulated Electrostatic Waves (AMEW) with high-speed spikes of the plasma velocities, related to the reconnection along the dayside magnetopause. Large-amplitude solitary waves have been observed by the Cluster spacecraft at multiple locations along the separatrices associated with magnetotail reconnection [*Cattell et al.*, 2005]. *Retinò et al.* [2006] have also identified the magnetic separatrix by taking a sharp boundary in electric field waveforms using the Wideband (WBD) Plasma Wave Investigation. The flow boundary has been defined by the density gradient, first observed magnetosheath ions on the magnetospheric side, a sharp change in the ion distribution, the plasma flow V_L component increases [*Lindstedt et al.*, 2009; *Gosling et al.*, 1990a], and the thermal speed of plasmas [*Vaivads et al.*, 2010].

5.2.1 Overview

Figure 5.3 shows magnetic field data from WIND and plasma and magnetic field data from Cluster 3 for an outbound crossing of the magnetopause on March 5, 2007. The solar wind speed was

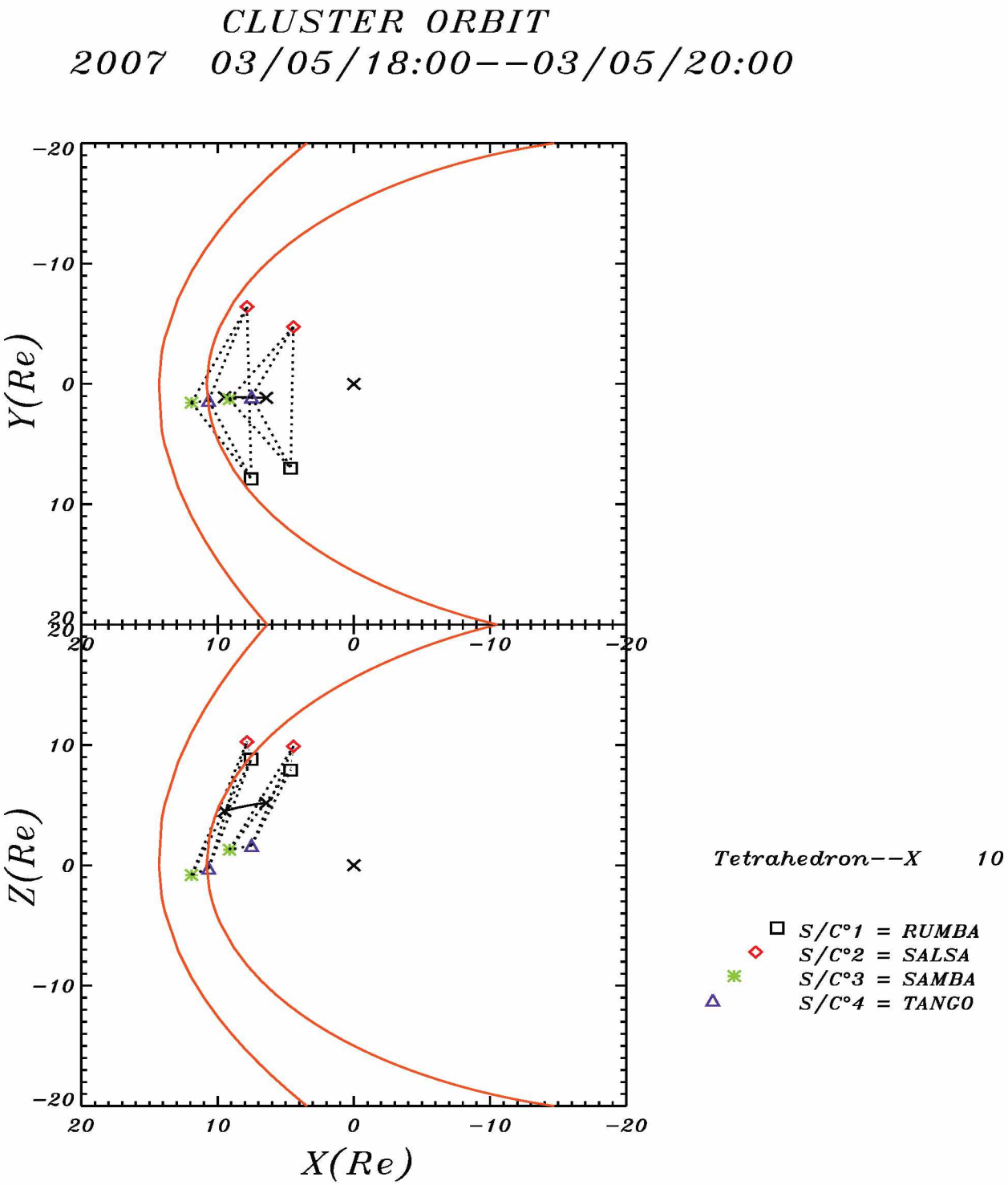

Figure 5.2. Cluster orbit in the X-Z and X-Y *GSM* plane from 18:00 UT - 20:00 UT on March 5, 2007. The tetrahedron configuration is enlarged by 10 times. The locations of the magnetopause and the bow shock, which are determined by the Fairfield model, are marked by the red lines [*Lee et al.*, 2014].

around 400 km/s as detected by the WIND satellite at $(X, Y, Z)_{GSM}$ = (200, -57.5, -43) R_E during the magnetic reconnection at the dayside magnetopause. Therefore, the solar wind parameters are shifted by about 64 minutes to match the Cluster magnetic field measurements. The IMF (B_x, B_y, B_z) was (-4, 1, -4) nT (Figure 5.3a), the geomagnetic activity index (Dst) was -9 nT, the dynamic pressure was less than 3 nPa and the Kp index was 4, indicating a moderately quiet magnetosphere (not shown). The spacecraft crossed the magnetopause several times, which can be identified by the sign change in B_z from positive (magnetosphere) to negative (magnetosheath) or the opposite (Figure 5.3b). The magnetic field strength (Figure 5.3c), the plasma density and three components of the plasma velocity from the CIS instrument as shown in Figures 5.3(d)–5.3(f). The ratio of the magnetic field strength on the magnetospheric side to that on the magnetosheath side is approximately 1.2 and the density ratio is about 1/13. The high-speed flow peaked at 350 km/s was observed from 18:50:00 UT to 19:20:00 UT (Figure 5.3f). It satisfies the Walén relation, indicating the spacecraft being in the reconnection exhaust region [*Paschmann et al.*, 1979; *Sonnerup et al.*, 1981]. Flow velocity in the de Hoffmann-Teller (HT) frame is highly correlated (0.93) with the local Alfvén velocity from 19:00:30 UT to 19:01:00 UT (not shown). The differential fluxes of energetic electrons, protons, helium (> 30 keV) and heavy ions (> 84 keV) from the RAPID instrument are shown in Figures 5.3(g)–5.3(j).

5.2.2 Geometry of the Magnetic Reconnection

Figure 5.4 shows C3 data from 19:00:00 UT to 19:20:00 UT. The bars at the top mark three different regions: the magnetosphere (Msp), the magnetosheath (Msh), and the boundary layer (BL). The ion energy spectrogram from CIS-HIA high sensitivity data shows a mixture of the magnetosheath ($\sim$ 1 keV) and magnetospheric ($\sim$ 10 keV) ions in the boundary layer, pure magnetospheric ion ($\sim$ 10 keV) in the magnetosphere, and pure magnetosheath ion ($\sim$ 1 keV) in the magnetosheath (Figure 5.4a). The electron differential flux parallel and anti-parallel to the magnetic field (4 s time resolution) from the PEACE instrument can also be used to distinguish different regions (Figures 5.4b–5.4d). In the boundary layer there are both magnetospheric ($\sim$ 10 keV) and magnetosheath ($\sim$ 100 eV) electrons and ions. High speed flow, $V_L \sim$350 km/s, was observed in the boundary layer (Figure 5.4e). The L component of the magnetic fields (B_L) changed its sign several times, indicating that C3 crossed the current sheet several times. The boundary normal coordinates (L_{GSE}=(-0.526, 0.298, 0.797), M_{GSE}=(-0.003, -0.937, 0.348), N_{GSE}=(0.850, 0.181, 0.494)), which were determined by the minimum variance analysis (MVA) of the magnetic field, are used. Three boundary crossings have been selected to understand the structure of the reconnection region in detail. The transition between the boundary layer and the magnetosphere is marked by the blue bar and between the boundary layer and the magnetosheath is marked by the red bar. The electric

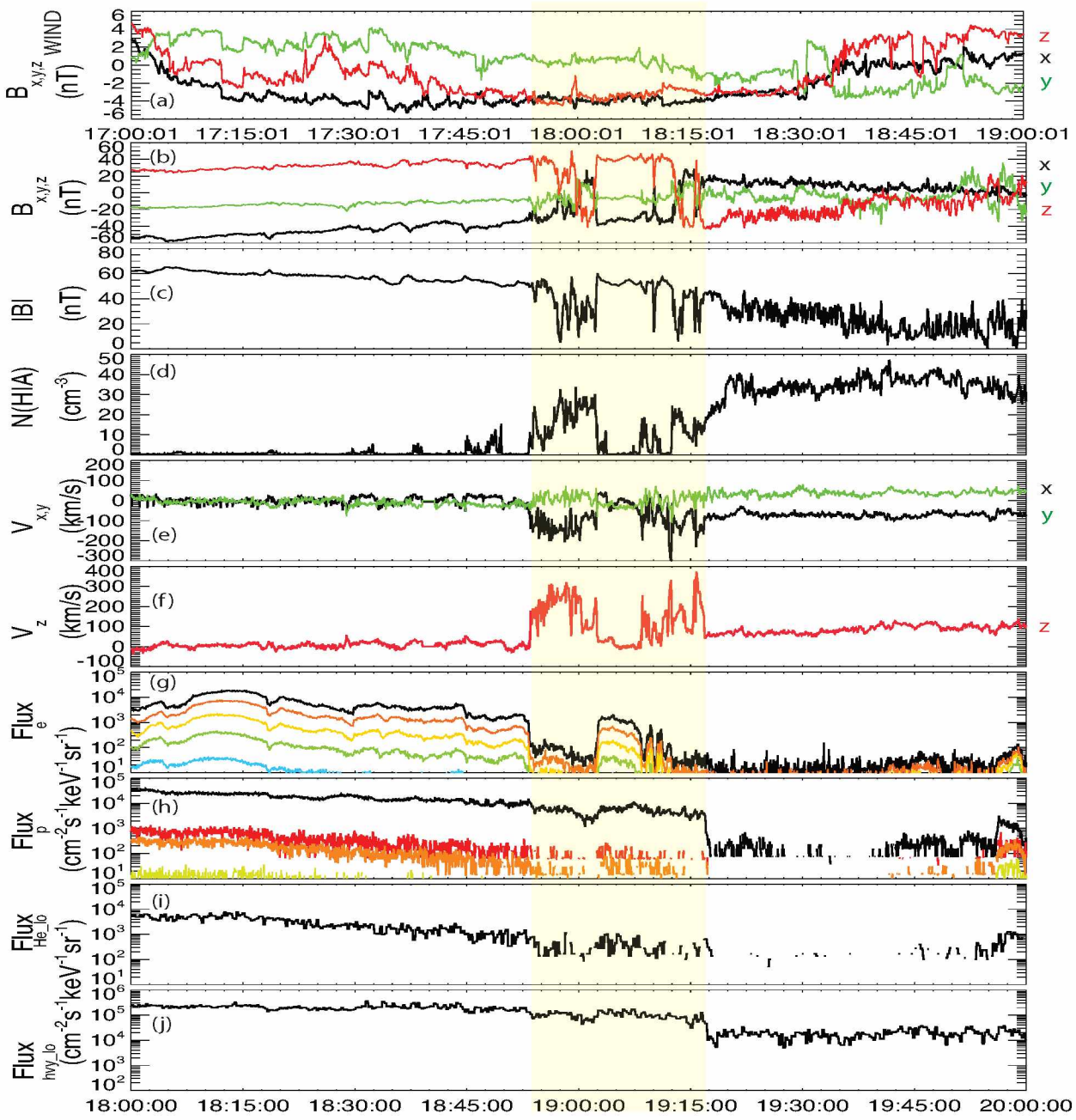

Figure 5.3. Field and plasma data from multiple magnetopause crossings collected by C3 from 18:00 UT to 20:00 UT on March 5, 2007. (a) Time-shifted (by 1 hour) interplanetary magnetic field (IMF) in the *GSM* coordinate from WIND satellite, (b) magnetic field in the *GSM* coordinates (x-component, black; y, green; z, red), (c) total magnetic field, (d) ion density, (e) plasma flow, V_x and V_y components, (f) V_z component in the *GSM* coordinates, and (g-j) differential particle flux of electrons, protons, helium (> 30 keV) and heavy ions (> 84 keV) [*Lee et al.*, 2014].

field spectrograms (1 s time resolution) from STAFF are displayed in extended time scale from 19:01:00 UT to 19:04:00 UT and from 19:06:00 UT to 19:09:00 UT on the magnetospheric side and from 19:15:00 UT to 19:18:00 UT on the magnetosheath side in Figure 5.4g. The spectrograms are used to determine the location of the separatrices (black dashed lines) on both the magnetospheric and magnetosheath sides where the wave emissions in high frequency range (> 200 Hz) become more intense and broader [*Retinò et al.*, 2006]. C3 crossed the separatrix on the magnetospheric side twice at 19:02:35 ± 1.5s UT and 19:07:19 ± 0.5s UT.

The separatrix on the magnetospheric side can also be identified from a sharp change in the parallel electron differential flux (4 s time resolution) at 19:02:36 ± 2s UT and 19:07:23 ± 2s UT, i.e., from a magnetosheath electron population with a typical energy of several hundred eV to a magnetospheric population of several keV (Figure 5.4c) [*Lindstedt et al.*, 2009]. The separatrix on the magnetosheath side was observed at 19:16:53 ± 0.5s UT when there was a sharp decrease in the wave emissions in the high frequency range. This separatrix can also be identified from a decrease in the electron flux anti-parallel to the magnetic field at 19:16:51 ± 2s UT. Considering the data resolution, the identifications of the separatrix from two different instrument measurements are consistent with each other. The separatrix angle (θ_s), which is the angle from the current sheet to the separatrix, can be calculated by taking the ratio of the magnetic fields at the separatrix, $\theta_s \approx \tan^{-1}(B_N/B_L)$ [*Xiao et al.*, 2007].

The separatrix angle derived from the second separatrix crossing is -5° ± 1°, which is similar with the separatrix angle (-5.5° ± 1°) derived from the first crossing at 19:02:34 ± 0.5s UT, indicating that the structure of the magnetic reconnection did not change while C3 crossed the separatrix twice. The magnetosheath side separatrix angle was 18° ± 1.5° (Figure 5.4j). The error bars were obtained from a propagation error analysis with data resolutions for each instrument. The separatrix angle on the magnetosheath side is much larger than that on the magnetospheric side, indicating an asymmetric magnetic reconnection geometry.

There are three ways to identify the flow boundary (gray dashed lines), the density gradients (Figure 5.4h) [*Vaivads et al.*, 2010; *Lindstedt et al.*, 2009], the velocity changes (Figure 5.4i) [*Lindstedt et al.*, 2009; *Gosling et al.*, 1990a], and the ion energy spectrum (Figure 5.4a) [*Lindstedt et al.*, 2009]. We used all three ways to identify the flow boundary on the magnetospheric side, which was observed at 19:02:31 ± 2s UT and at 19:08:00 ± 2s UT. However, the flow boundary on the magnetosheath side is hard to identify using the density changes because the density on the magnetosheath side of the reconnection region is already high. Therefore *Gosling et al.* [1990a] used the velocity changes to identify the flow boundary (ion edge) and *Lindstedt et al.* [2009] identified the flow boundary using the velocity changes of V_L and the ion energy spectrum on the magnetosheath side, which are the same criteria as we used and it was observed at 19:16:47 ± 2s UT.

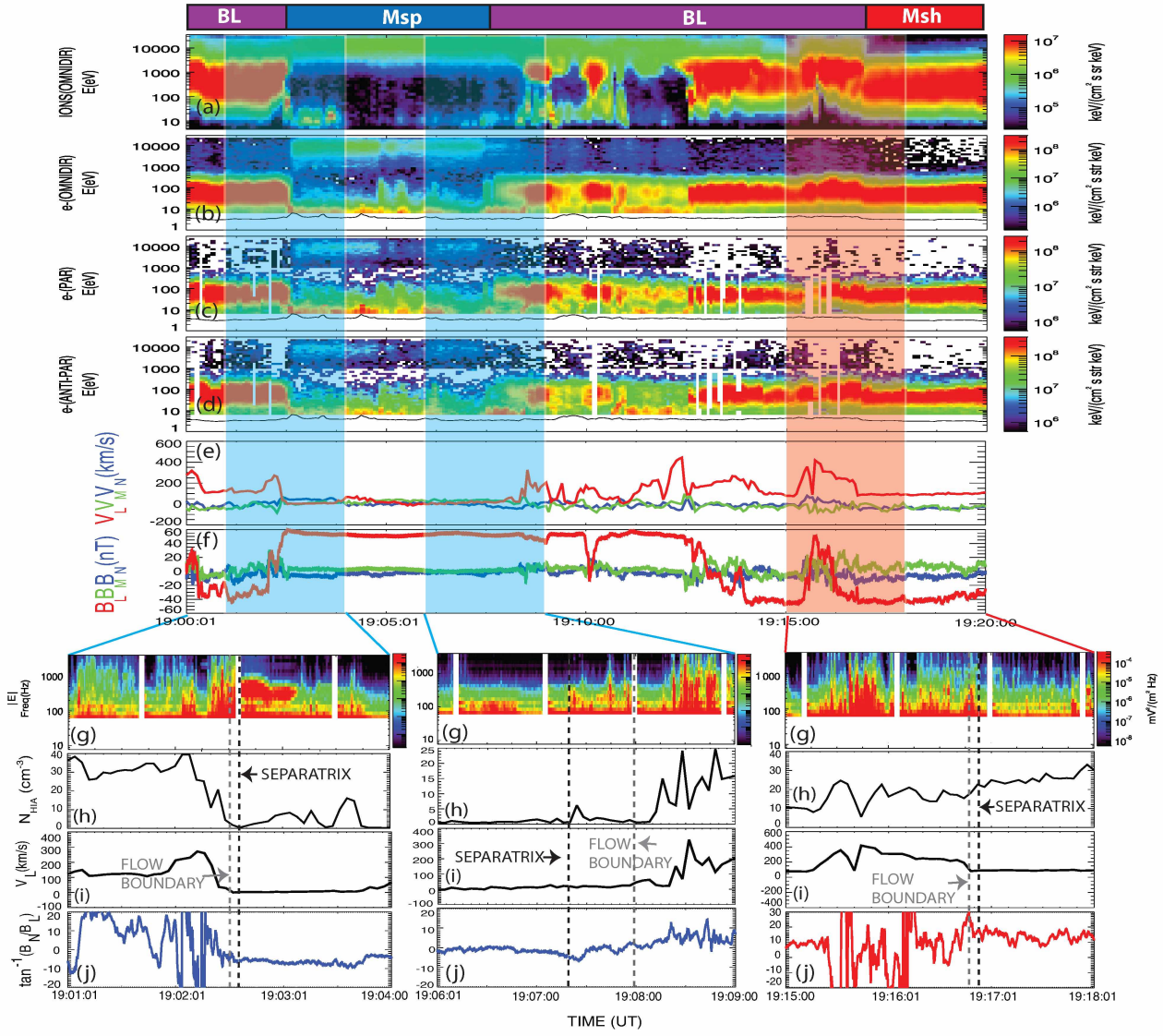

Figure 5.4. Extended time scale observations from C3. Two blue bars and a red bar show the separatrix crossings on magnetospheric and magnetosheath side. (a) Energy spectrogram of ions, (b) electron differential flux (omni-direction), (c and d) electron differential flux parallel and anti-parallel to the magnetic field, (e and f) velocity and magnetic field projected in the *LMN* coordinate system, respectively, (g) electric field spectrogram from 19:01:00 UT to 19:04:00 UT (left), from 19:06:00 UT to 19:09:00 UT (middle), and from 19:15:00 UT to 19:18:00 UT (right), (h) plasma flow, V_L component, (i) plasma density, (j) arctangent of B_N/B_L [*Lee et al.*, 2014].

The angle of flow boundary relative to the current sheet can be obtained by using the simple trigonometry (see Figure 5.5a). If the structure is stable and moves at a constant speed along the direction normal to the magnetopause, time intervals taken from the current sheet (blue dashed line) to the flow boundary (gray solid line) and to the separatrix (black solid line) are proportional to the distances. The velocities of the structure along the normal direction, while crossing the current sheet and the separatrix on the magnetospheric side, are 28.5 ± 3.6 km/s and 26.7 ± 1.1 km/s, respectively. The normal velocities obtained from two different boundary crossings by the timing method are similar, so the assumption is reasonable. We obtain the time intervals, t_s = 32 ± 1.5s and t_f = 27 ± 2s, to approach the separatrix and the flow boundary from the current sheet during 19:01:00 UT - 19:04:00 UT, respectively, and the separatrix angle ($\theta_{s,magnetosphere}$ = -5.5° ± 1°) on the magnetospheric side, allowing the flow boundary angle (θ_f) to be estimated at $\theta_f \approx \tan^{-1}(t_f/(t_s/\tan\theta_s))$. The flow boundary angle on the magnetospheric side is -4.6 ± 0.9°. The flow boundary angle on the magnetosheath side can be also obtained as 15.6° ± 1.7° by taking t_s = 42 ± 0.5s, t_f = 36 ± 2s, and $\theta_{s,magnetosheath}$ = 18° ± 1.5°.

The separatrix angle ($\theta_{s,magnetosheath}$) and flow boundary angle ($\theta_{f,magnetosheath}$) on the magnetosheath side are larger than those on the magnetospheric side (strongly asymmetric). Then the geometry of the asymmetric reconnection can be deduced with different separatrix and flow boundary angles and illustrated in Figure 5.5(a). C1 crossed the separatrix on the magnetospheric (magnetosheath) side at 19:03:38 ± 0.5s UT (19:17:48 ± 2s UT) with separatrix angles, -6.5° ± 0.5° (18° ± 1°). The flow boundary was observed by C1 at 19:03:34 ± 2s UT with flow boundary angle -5.7° ± 0.6° on the magnetospheric side and at 19:17:28 ± 2s UT with 17° ± 1° on the magnetosheath side.

C1 (black square) and C3 (green square) configurations are also illustrated in the *LMN* reference frame, while they were crossing the separatrices several times on the magnetospheric and the magnetosheath sides (Figure 5.5a). The distances of C3 and C1 from the X-line can be estimated by using the separatrix angles, velocity of the structure along the normal direction, and the time differences from the current sheet to the separatrix. For example, using the time interval, 32 s, which C3 takes from the current sheet to the separatrix on the magnetospheric side, and the velocity of the structure along the normal direction, 28.5 km/s, the distance (h = V×t) from the current sheet to the separatrix is 0.14 ± 0.02 R_E. And taking the tangent of the separatrix angle (ℓ = h/tanθ_s), the distances (ℓ, red numbers) from the X-line to the location of the C3 and C1 on the magnetospheric side (magnetosheath side) can be obtained as 1.48 ±0.2 R_E (0.25 ±0.06 R_E) and 1.21 ±0.18 R_E (0.95 ±0.13 R_E), respectively.

The RAPID experiment on board Cluster measures 3-D energetic proton fluxes in the energy range above 30 keV (Figure 5.5b) and FGM measures L component of the magnetic field observed

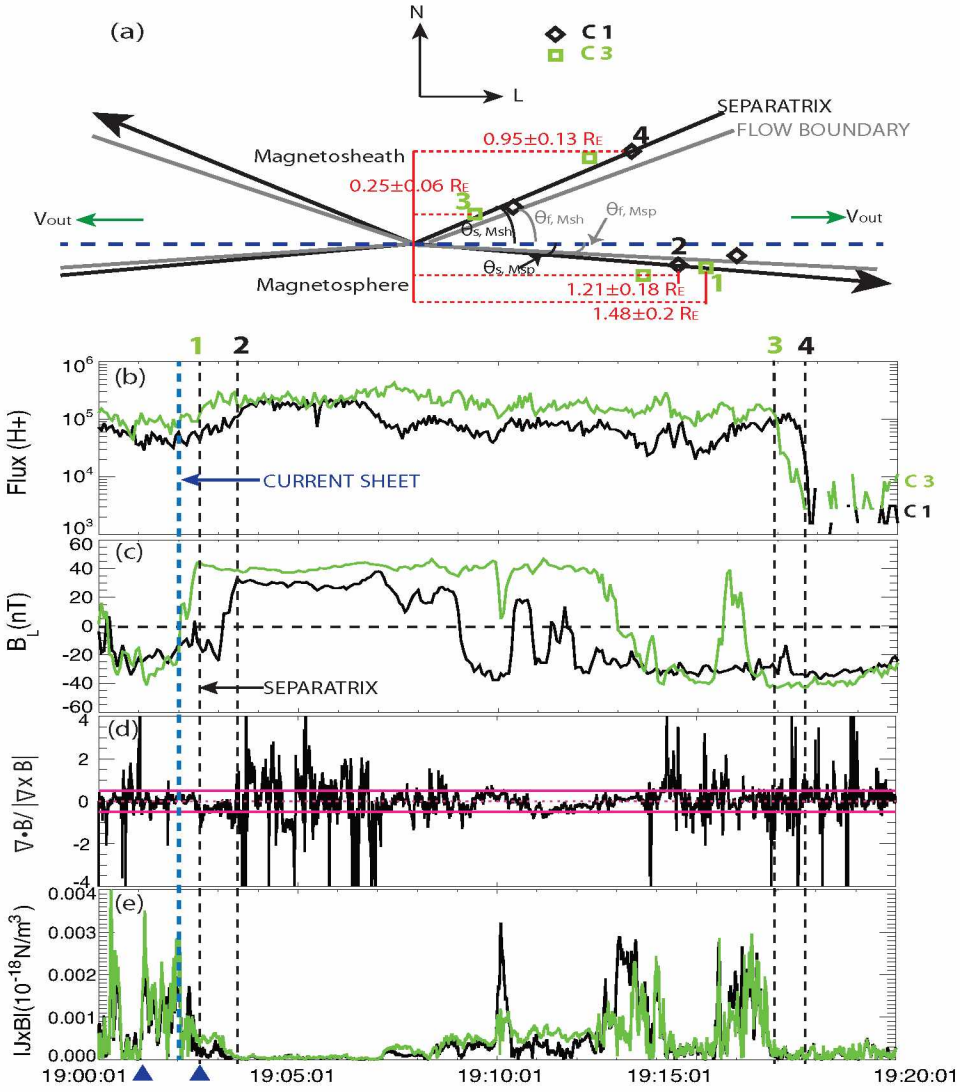

Figure 5.5. (a) A sketch of the asymmetric reconnection geometry with different separatrix angles (θ_s) and the flow boundary angles (θ_f), $\theta_{s,magnetosheath}$ = 18°±1.5°, $\theta_{s,magnetosphere}$ = -5.5°±1°, $\theta_{f,magnetosheath}$ = 15.6°±1.7°, and $\theta_{f,magnetosphere}$ = -4.6°±0.9° in the boundary normal coordinates, assuming the motion of structure is stable and moves at a constant speed along the direction normal to the magnetopause. '1' and '3' ('2' and '4') mark the times when C3 (C1) cross the separatrices (e.g., '1' is the time when C3 crosses the separatrix on the magnetospheric side). The red numbers show the distances from the X-line to the locations of the C1 and C3 at the separatrices. (b) Differential flux of energetic protons, (c) B_L component, (d) error of current calculation, and (e) J×B force density observed by C1 and C3. The separatrices are marked by black dashed lines and the current sheet crossings are marked by blue dashed lines [*Lee et al.*, 2014].

by C1 (black line) and C3 (green line) (Figure 5.5c). In the plot we have identified several separatrix crossings labeled '1' to '4' with black dashed lines (e.g., '1' marks the time when C3 crosses the separatrix on the magnetospheric side). The flux detected by C3 was higher than that detected by C1 because C3 is closer to the equator and the X-line. The distances (numbers in red color) from the X-line are approximately the same within the error bar when C1 and C3 crossed the separatrix on the magnetospheric side ('1' and '2') so that same amount of fluxes were detected (Figure 5.5b); on the other hand, more energetic protons were observed by C3 than C1 when they crossed the separatrix on the magnetosheath side ('3' and '4') because C1 was further away from the X-line.

The current sheets are marked by blue dashed lines, the separatrices by black dashed lines. The left boundaries cover the inbound pass of the magnetopause while those on the right describe its outbound pass. The current can be calculated from the curl of the magnetic fields measured by the four spacecraft using the curlometer method. The quantity $\nabla \cdot \mathrm{B}/\ |\nabla \times \mathrm{B}|$ can be used as an estimate of the error, $\Delta J/J$ [*Robert et al.*, 1998]. Most of the values of $\nabla \cdot \mathrm{B}/\ |\nabla \times \mathrm{B}|$ (the error of current density calculation) are between ± 0.5, indicating that the current calculation is reliable in general (Figure 5.5d). The $\mathbf{J} \times \mathbf{B}$ force density on the magnetosheath side is approximately 0.0018 10^{-18} N/m^3 from 19:01:06 (marked by blue triangles) to 19:02:04 UT (blue dashed line, i.e., the current sheet), while that on the magnetospheric side is about 0.0005 10^{-18} N/m^3 from 19:02:04 (blue dashed line, i.e., the current sheet) to 19:02:36 UT (marked by blue triangles) for C3 (Figure 5.5e). The force is larger on the magnetosheath side of the reconnection region than that on the magnetospheric side.

5.2.3 Cold and Energetic Ion Behaviors

Both cold ions (5∼30 eV) and energetic ions (>10 keV) were present in the magnetosphere from 19:02:20 - 19:05:00 UT (Figure 5.6a). The motion of the cold ions were initially perpendicular to the magnetic field (Figure 5.6b) and were accelerated perpendicular to the magnetic field between the separatrix and the flow boundary and beyond the flow boundary (Figures 5.6c–5.6e). The pitch angle of the magnetospheric ions (>10 keV) peaked at 90° in the magnetosphere. The energetic ions also moved perpendicular to the magnetic field between the separatrix and the flow boundary. Then the pitch angle of the energetic ions peaked at 0° from 19:02:04 UT to 19:02:31 UT (between the blue dashed line and the black dashed line) and 180° from 19:01:00 UT to 19:02:04 UT (inside the blue dashed line) (Figures 5.6j–5.6l). Mixture of magnetospheric and magnetosheath ions (Figures 5.6e–5.6i, 100 eV∼10 keV) moved parallel to the magnetic field on the magnetospheric side of the reconnection region (0° pitch angle) and anti-parallel to the magnetic field on the magnetosheath side (180° pitch angle). The cold ions were not observed on the magnetosheath side of the current sheet.

The energetic ions were observed in the boundary layer during the reconnection process. The energetic ions (>10 keV) have 90° pitch angle outside of the reconnection region in the magnetosphere (Figures 5.6j–5.6l). Once they entered the reconnection region, the pitch angle changed to 0° on the magnetospheric side of the reconnection region, then to 180° on the magnetosheath side. The observed pitch angle distributions are consistent with the reconnection picture: The energetic ions flow into the reconnection region from the magnetosphere and participate the reconnection process, then they are accelerated together with other magnetosheath ions and thermal magnetospheric ions by the reconnection and observed in the outflow region.

Figure 5.7 shows 9 examples of two-dimensional cuts through the three-dimensional distributions observed while C3 is near the current sheet (Figure 5.7C 1-3), at the flow boundary (Figure 5.7F 1-3) , and at the separatrix (Figure 5.7S 1-3). The horizontal and vertical axes denote velocity components perpendicular and parallel to the magnetic field, respectively. There were two ion populations detected simultaneously at the separatrix on the magnetospheric side in Figures 5.7(S1) and 5.7(S2): one was the cold dense plasmaspheric ions with energies of the order of 10 eV, the other, the hot magnetospheric ions with energy above ~10 keV. Both populations were flowing perpendicular to the magnetic field. The magnetosheath ions also moved perpendicular to the magnetic field (Figure 5.7(S3)). The thermal and energetic magnetospheric ions moved parallel to the magnetic field at the flow boundary (Figure 5.7(F1)) and the magnetosheath ions moved anti-parallel to the magnetic field (Figure 5.7(F3)), while the cold ions were accelerated with near zero parallel velocity as shown in Figure 5.7(F2) by comparing the perpendicular velocity in Figure 5.7(S2). The mixture of the magnetospheric ions and transmitted magnetosheath ions were flowing parallel and anti-parallel to the magnetic field, respectively in Figure 5.7(C1) and 5.7(C3). The cold ions were not observed on the magnetosheath side of the reconnection region, i.e., inside the flow boundary (Figure 5.7(C2)).

5.3 Discussion

5.3.1 Asymmetric Reconnection Geometry

In the previous section, we have shown that the flow boundary angle on the magnetospheric side is -4.6° ± 0.9° and on the magnetosheath side is 15.6° ± 1.7° and the saperatrix angle on the magnetospheric side is θ_s = -6.5° ± 0.5° and 18° ± 1° on the magnetosheath side. These results show a significant asymmetric reconnection geometry at the dayside magnetopause. How can we understand the asymmetric reconnection geometry at the dayside magnetopause?

In MHD simulations, the location of the X-line has been predicted by using the conservation of magnetic energy flux and follows $\delta_{X2}/\delta_{X1} \approx B_2/B_1$, where $\delta_{X1,2}$ are the distances between the upstream edges of the dissipation region and the X-line [*Cassak and Shay*, 2009]. For asymmetric

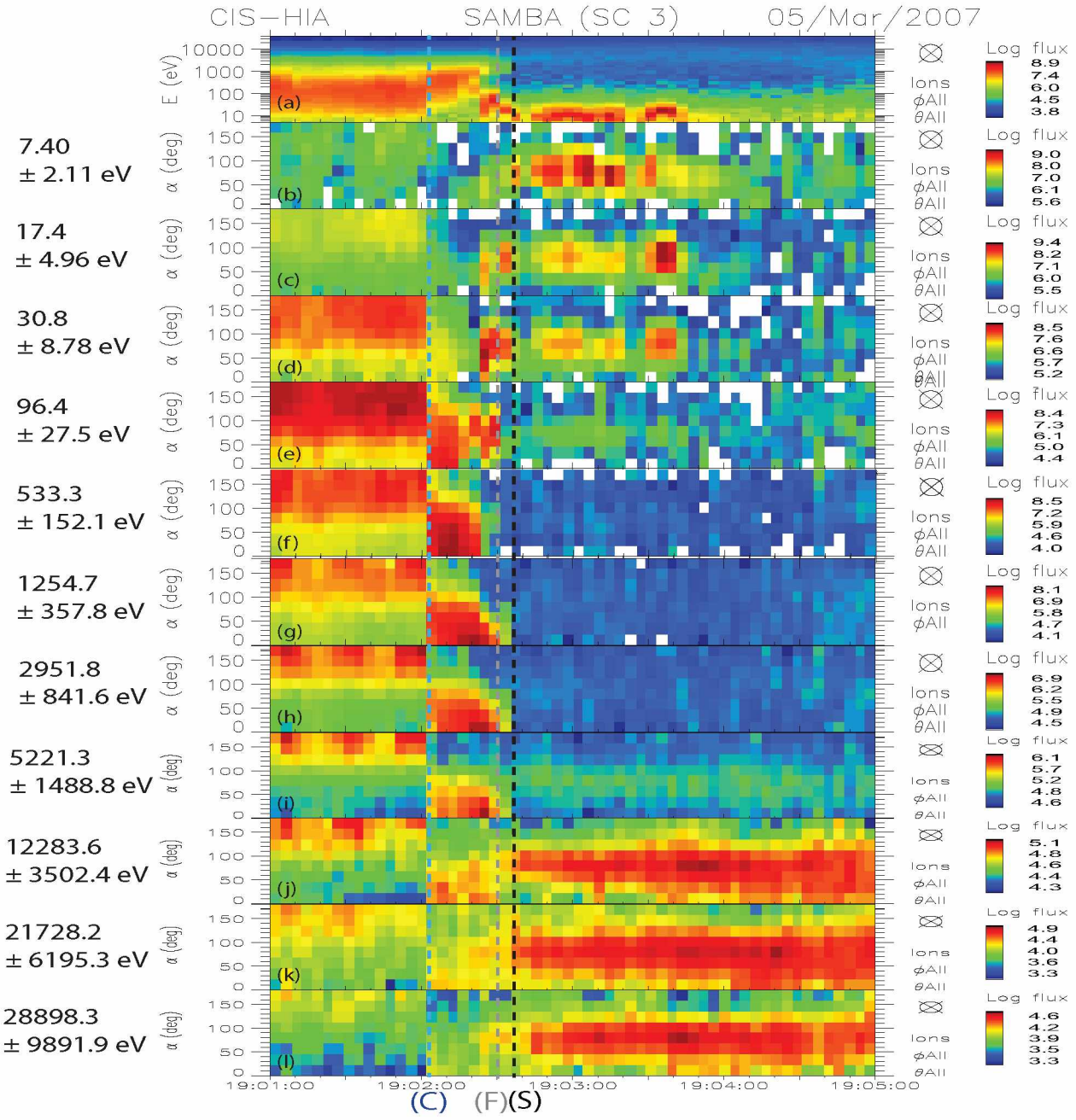

Figure 5.6. (a) Ion energy spectrum and (b-l) pitch angle distributions with different energy channels from 19:01:00-19:05:00 UT. Boundaries marked by vertical dashed lines are the separatrix (black dashed line, (S)), the flow boundary (gray dashed line, (F)), and the current sheet (blue dashed line, (C)) [*Lee et al.*, 2014].

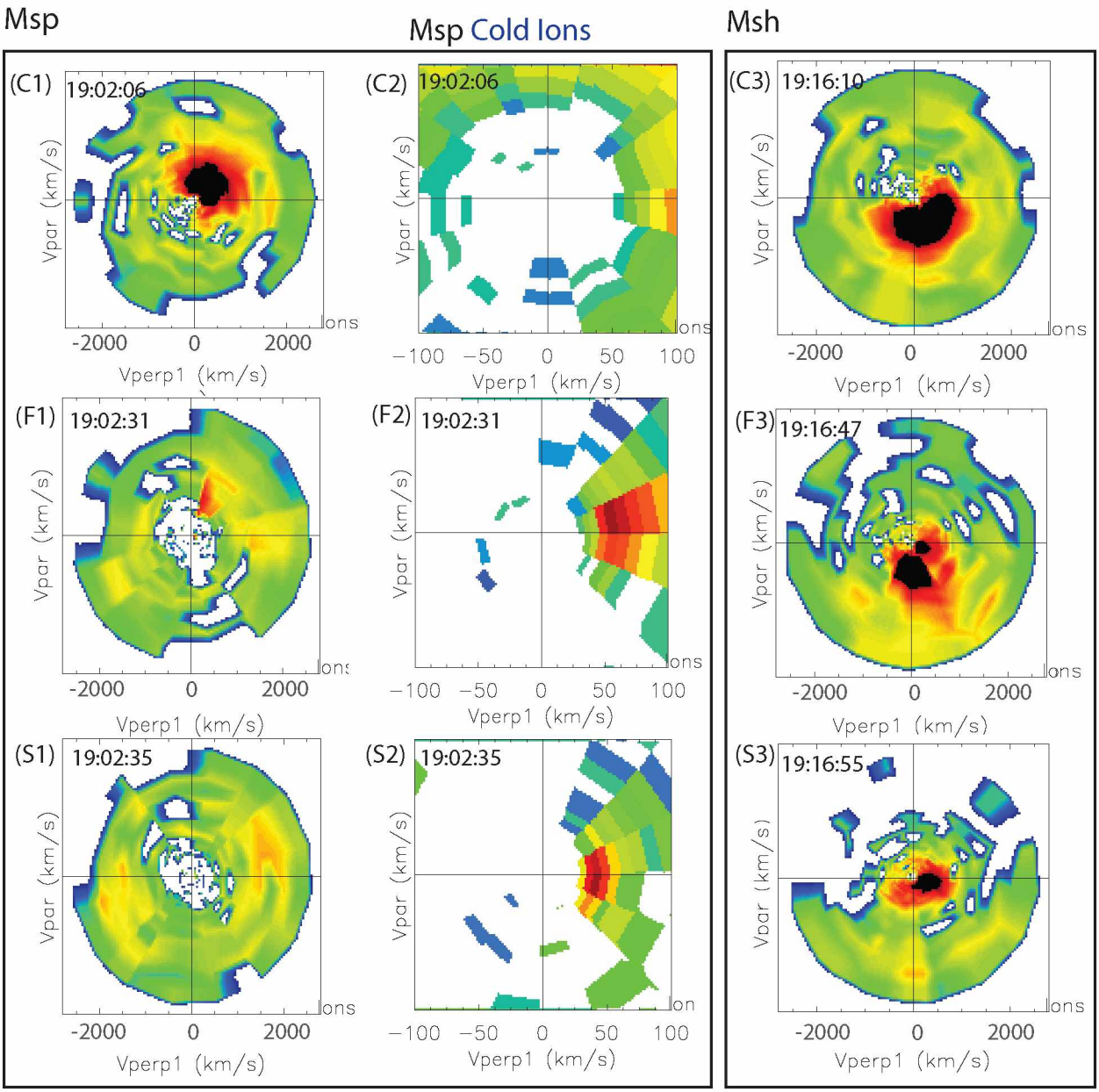

Figure 5.7. Two-dimensional cuts of the three-dimensional ion distributions obtained while C3 is (C 1-3) near the current sheet, (F 1-3) at the flow boundary, and (S 1-3) at the separatrix. There are three ion populations: the thermal and the energetic magnetospheric ions; the cold ions originating from the plasmasphere; and the transmitted magnetosheath ions. The cold ion behavior is different from the behaviors of the transmitted magnetosheath ions and thermal and energetic magnetospheric ions [*Lee et al.*, 2014].

reconnection, it has been shown by MHD simulation that the X-line and stagnation point are not co-located, enabling the bulk plasma inflow to cross the X-line. The X-line is offset toward the side with weaker magnetic field and sub-Alfvénic flow compared to that with the stronger magnetic field and the super-Alfvénic flow since it takes more energy to bend the magnetic fields on the strong field side and the stagnation point is offset toward whichever side has the smaller value of ρ/B [*Cassak and Shay*, 2007; *Birn et al.*, 2008; *Cassak and Shay*, 2009]. If the X-line moves toward the magnetosheath side, the separatrix angle on the magnetosheath side should be smaller than that on the magnetospheric side, which is opposite to the results obtained in this chapter.

In this chapter, we have analyzed in detail boundaries of the reconnection region and found an asymmetric structure, i.e., the separatrix and flow boundary angles and the $\mathbf{J} \times \mathbf{B}$ force density on the magnetosheath side are larger than those on the magnetospheric side. Acceleration of a higher density plasma requires a larger $\mathbf{J} \times \mathbf{B}$ force density, which is proportional to the square root of density and magnetic field ($\mathbf{J} \times \mathbf{B} = \mathbf{F} = \mathrm{nm}\mathbf{a} = \mathrm{nm}\mathbf{V_A}/\mathrm{t} = \mathrm{nm}\mathbf{B}/(\sqrt{\mu_0 nm}\mathrm{t}) \propto \sqrt{n}\mathbf{B}$). The $\mathbf{J} \times \mathbf{B}$ force density is also proportional to the tangent of the separatrix angle ($\mathbf{J} \times \mathbf{B}$ force density $\propto \tan(\theta_s)$). This causes the separatrix angle on the magnetosheath side to be larger than that on the magnetospheric side because the density ratio (~13) of the magnetosheath to the magnetospheric side is larger than magnetic field ratio (~1.2) of two sides. The larger force on the magnetosheath side can shift the X-line toward the magnetospheric side which is consistent with the results from *Mozer et al.* [2008].

5.3.2 Can Cold Ions Affect the Reconnection Dynamics?

The cold ions (5~30 eV) with near zero parallel velocity were observed at the separatrix (Figure 5.8a). As can be seen from Figure 5.8(b), once the cold ions were energized, three cold ion populations (probably H^+, He^+, and O^+) appeared in the energy spectrum because they have different masses and were accelerated to the same velocity (~100 km/s). Helium (He^+) and oxygen ions (O^+) were energized 4 and 16 times higher than that of the proton (H^+). *Borovsky and Steinberg* [2006] hypothesized that high-density plasma could reduce the local Alfvén speeds, and *Borovsky and Denton* [2006] noticed reductions in the amount of solar wind/magnetosphere coupling during geomagnetic storms when very high density plasma from the plasmasphere was convected into the dayside reconnection site. In a simulation study, *Borovsky et al.* [2008] showed a spatially localized plume of plasma can reduce the reconnection rate by about a factor of 2. However, the accelerated cold ions motion we have observed were perpendicular to the magnetic field. If they were accelerated by the reconnection process like the thermal and energetic magnetospheric ions, they would have velocity parallel to the magnetic field. In addition, the cold ions should be observed in the outflow region with other accelerated particles if they flow into the diffusion region and participate

the reconnection process. However, the cold ions were observed only near the separatrix and the flow boundary on the magnetospheric side. Therefore, the cold ions did not participate in the reconnection process.

The schematic drawings of the motion of the thermal and energetic magnetospheric ions (red arrows), cold ions (blue arrows), and the magnetosheath ions (dark green arrows) in the HT frame (where the convection electric field vanishes) are illustrated in Figure 5.9. Thermal and energetic magnetospheric ions and the magnetosheath ions were accelerated with large parallel velocities by the reconnection process and away from the X-line as shown in Figure 5.9(t1). The cold plasmaspheric ion flow into the reconnection outflow region by the $\mathbf{E}\times\mathbf{B}$ drift rather than into the diffusion region near the subsolar magnetopause (Figure 5.9(t2)). Thus the cold ions are picked up by newly reconnected field line at high latitude and accelerated by the convection electric field perpendicular to the magnetic field, which is similar to the pickup ion process in the solar wind. Behavior of the cold ions in our observations agrees with the test particle simulation results from *Drake et al.* [2009]. *Drake et al.* [2009] showed that heavy ions crossing the separatrix into the exhaust behave like pick up ions, which perform a cycloidal motion in the plane perpendicular to the guide field and gain perpendicular energy. Our observations show that the cold ions also behave like pick up ions, which were carried into the reconnection region by the reconnected field line and gain perpendicular energy. *Gosling et al.* [1990b] also observed a cold ion beam whose speed was always less than the transmitted magnetosheath ions although both populations shared the same $\mathbf{E}\times\mathbf{B}$ drift. They suggested that the cold beams are accelerated simply by being tied to the field lines. Our observations are consistent with those of *Gosling et al.* [1990b].

5.4 Summary and Conclusions

We have presented a study of an asymmetric magnetic reconnection event on March 5, 2007 at the dayside magnetopause. Separatrices and flow boundaries on both the magnetospheric and magnetosheath sides are identified by sharp changes in the electromagnetic wave spectrogram, particle differential flux, plasma flow, magnetic field and density gradients. The cold plasmaspheric ions (5$\sim$30 eV) are observed on the magnetospheric side of the current sheet and the energetic protons, helium, ($>$ 30 keV) and oxygen ions ($>$ 84 keV) are also observed in the reconnection region. The significant observations can be summarized as follows:

1. The separatrix and flow boundary angles on the magnetosheath side are larger than those on the magnetospheric side. This may be caused by the stronger asymmetry in the plasma density than that in the magnetic field.

2. The asymmetric geometry of the magnetic reconnection is obtained by different separatrix

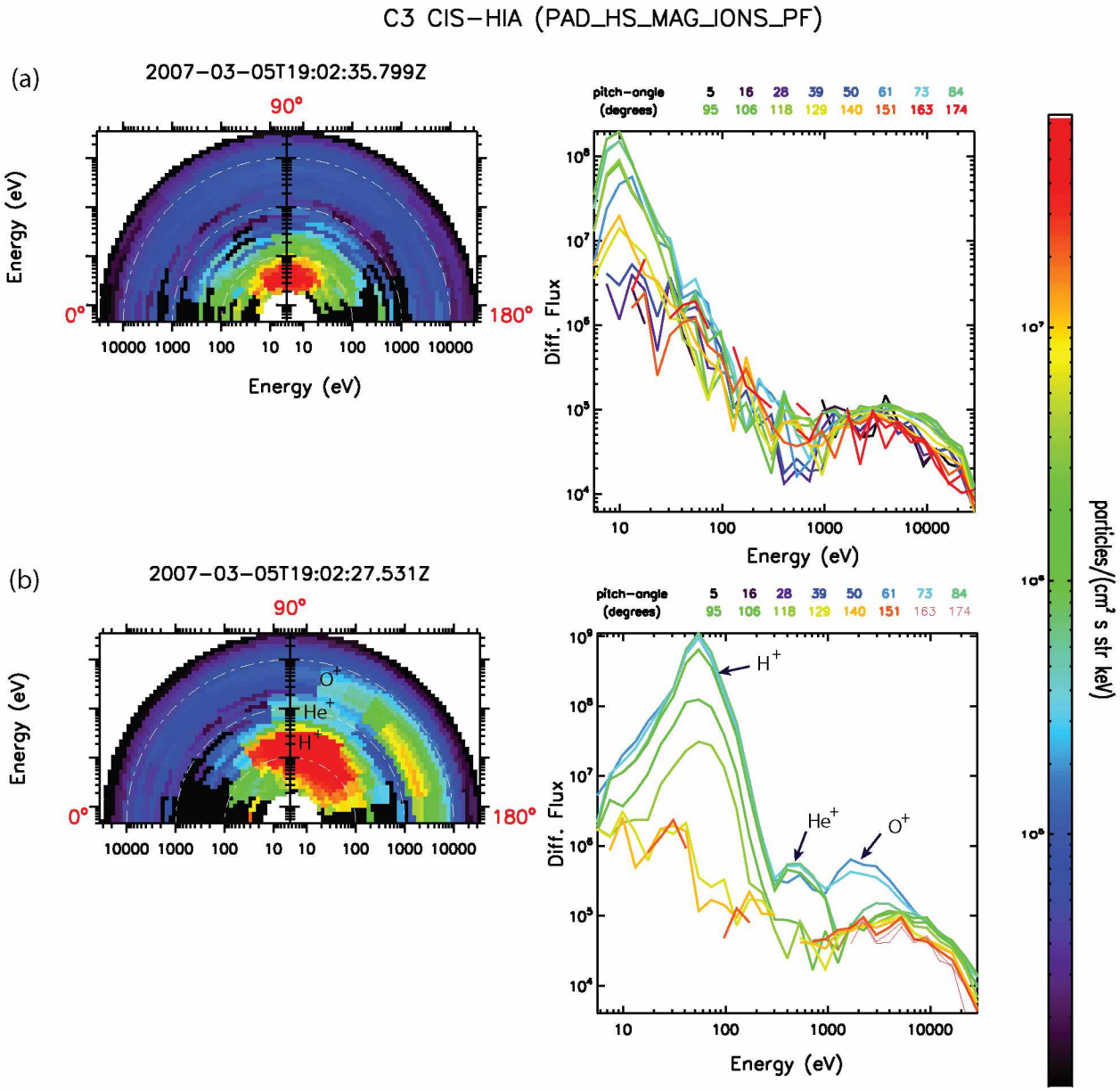

Figure 5.8. The energy spectra of cold ions with different pitch angles during the magnetic reconnection (a) at the separatrix and (b) inside the flow boundary. The cold dense plasmaspheric ions with near zero parallel velocity were observed at the separatrix (a) and were accelerated perpendicular to the magnetic field inside the flow boundary (b). Three cold ion populations (probably H^+, He^+, and O^+) appear in the energy spectrum because they have different masses and were accelerated to the same velocity (~100 km/s) [*Lee et al.*, 2014].

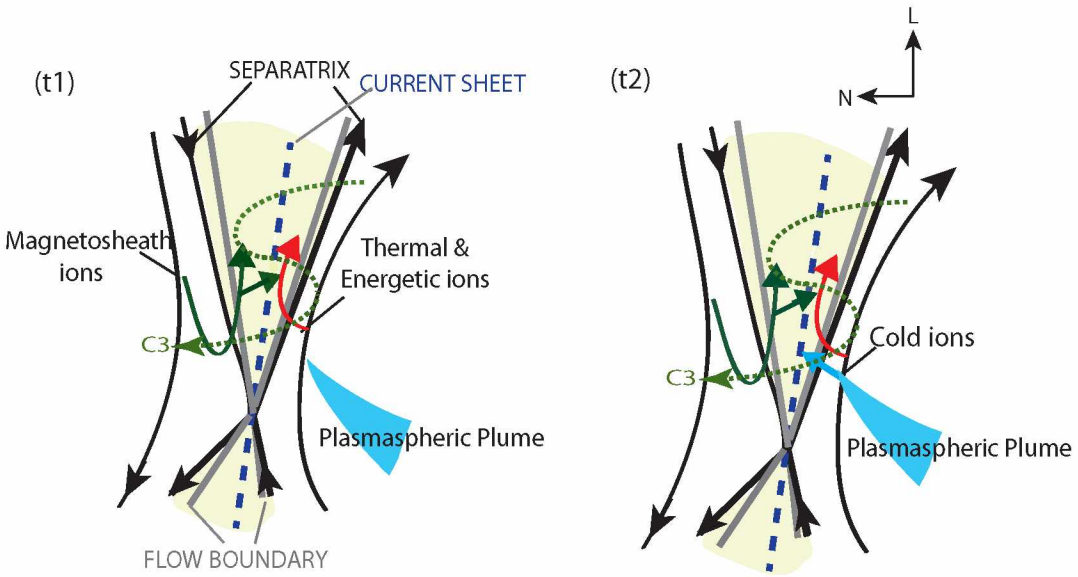

Figure 5.9. Reconnection configuration with qualitative sketch of the motion of cold (blue arrow), thermal and energetic magnetospheric ions (red arrow), and magnetosheath ions (dark green arrows) in the HT frame. The transmitted magnetosheath ions and thermal and energetic ions are accelerated by the reconnection process (t1). The source of the cold ions in reconnection can be plumes detached from the plasmasphere. The cold ions flow into the reconnection outflow region by the $\mathbf{E}\times\mathbf{B}$ drift. They are picked up by newly reconnected field line and accelerated by the convection electric field perpendicular to the magnetic field (t2). The green dotted line shows the spacecraft (C3) trajectory. The black lines, which are connected to the X-line, denote the separatrices, the gray lines correspond to the flow boundaries, the blue dashed line marks the current sheet crossings, and the yellow area shows the reconnection region [*Lee et al.*, 2014].

angles on both sides of the current sheet.

3. The cold dense plasmaspheric ions are picked up by recently reconnected field lines at higher latitude rather than in the diffusion region near the subsolar magnetopause. These cold ions are accelerated by the electric field perpendicular to the magnetic field and carried by the reconnection convection flow which is similar to the pickup ion process.

4. Three cold ion populations (probably H^+, He^+, and O^+) appear in the energy spectrum because they have different masses and are accelerated to the same velocity.

5. The observed pitch angle distributions for the energetic ions (> 10 keV) in the boundary layer are consistent with the reconnection picture.

Chapter 6
Asymmetric Ionospheric Outflow Observed at the Dayside Magnetopause

6.1 Introduction

The dominant sources of the plasma in the dayside low-latitude boundary layer of the magnetosphere are solar wind plasma from the magnetosheath, the magnetospheric plasma from the outer magnetosphere, and cold plasma from the ionosphere. During southward interplanetary magnetic field (IMF), solar wind plasma travels along the merged magnetic field line and is conducted into the low-latitude boundary layer. Even during periods of northward IMF, solar wind plasma is convected toward the magnetosphere with several transfer processes. The three different populations can be distinguished with their different energies shown in the energy spectra: the magnetosheath plasma (~1 keV), the magnetospheric plasma (~10 keV), and the ionospheric plasma (~1 eV).

The observed low-energy ions of ionospheric origin at the dayside magnetopause may result from three different regions: the plasmaspheric plume, the plasmaspheric wind, and the ionospheric outflow. During increasing geomagnetic activity, the enhanced convection electric field causes erosion of the outer plasmasphere. Thus, the cold and dense plasmaspheric ions can be released to the Earth's dayside magnetopause, which is called detached plasmaspheric material or plume [*Su et al.*, 2000; *McFadden et al.*, 2008; *Goldstein et al.*, 2004]. *Lee et al.* [2014] have reported the plume of cold plasma observed at the dayside magnetopause by the Cluster spacecraft. They have found that the plasmaspheric cold ions were transported into the reconnection region by $\mathbf{E} \times \mathbf{B}$ drifts at high latitudes on the recently reconnected magnetic field lines. *Walsh et al.* [2014] have also shown simultaneous observations of a plasmaspheric plume and its involvement in the dayside magnetic reconnection by using ground-based total electron content maps and Time History of Events and Macroscale Interactions during Substorms measurements.

The existence of a plasmaspheric wind was proposed by *Lemaire and Schunk* [1992]. This wind steadily transports cold plasmaspheric plasma outward across the magnetic field lines, even during quiet geomagnetic conditions. *Dandouras* [2013] presented Cluster observations of the plasmaspheric wind in the Earth's magnetosphere during quiet and moderately active geomagnetic conditions.

The ionospheric ion outflows also play very important roles as a particle source for populating the inner magnetosphere, nightside plasma sheet, and ionosphere-magnetosphere coupling [*Chappell et al.*, 1987; *Moore*, 1991]. The low-energy (~0.1 eV) ionospheric ions need to be energized at least to about ~10 eV by more than one ion energization mechanism in order to reach their escape velocities [*Yau and André*, 1997; *Engwall et al.*, 2009; *Yau et al.*, 2007; *Zheng et al.*, 2005; *Strangeway et al.*, 2005]. However, ionospheric ion outflows have rarely been observed at the dayside magnetopause.

Fuselier et al. [1989] have reported that field-aligned oxygen ion (O^+) beams and the enhanced O^+ density were observed in the low-latitude boundary layer from the Charge Composition Explorer satellite in the Active Magnetospheric Particle Tracer Explorers mission. They have suggested that the northern and southern high-latitude polar regions are potential sources for the O^+ beams, which have velocities both parallel and antiparallel to the magnetic field in the dayside magnetospheric boundary layer.

In this chapter, first, we show that the asymmetric ionospheric ion outflows (cold ions coming only from the Southern Hemisphere) are observed by the Cluster spacecraft during a magnetic reconnection event at the dayside magnetopause on 8 April 2008. In addition, cold ion (< 200 eV) flux modulations caused by the ULF wave electric fields are discussed.

6.2 Observations and Analyses

6.2.1 Overview of Observations

The Cluster observations and the DMSP F13 and F15 spacecraft data sets are used to investigate the properties of the cold ions observed at the dayside magnetopause in this chapter. Figure 6.1 shows the Cluster 1, Cluster 3, DMSP F13, and F15 spacecraft locations illustrated in the X-Y, Y-Z, and Z-X GSE plane at 12:35:00 UT on 8 April 2008. Cluster 1 (C1, black square) and Cluster 3 (C3, green star) were located at (X, Y, and Z) = (10.943, -1.529, and 1.320) and (10.868, -2.680, and 0.934) R_E, respectively, in the GSE reference frame. The Cluster spacecraft was traveling in the northern hemisphere on the dawn side. DMSP F13 (F13, orange upside down triangle) was in the Northern Hemisphere, (X, Y, and Z) = (0.334, 0.212, and 1.057) R_E and DMSP F15 (F15, dark green star) was in the Southern Hemisphere, (X, Y, and Z) = (-0.415, 0.102, and -1.045) R_E. The locations of the magnetopause and the bow shock, which are determined by the Fairfield model, are marked by the red lines [*Fairfield*, 1971].

Figure 6.2 shows solar wind observations from the Wind spacecraft. The solar wind speed, as measured by Wind located at (X, Y, and Z)$_{GSE}$ = (205.127, 76.675, and -9.785) R_E, is around 626 km/s. At this speed, it took the solar wind about 35 mins to propagate from Wind to Cluster. The shaded region marks the interval corresponding to the Cluster observation from 12:30:00 UT to 12:50:00 UT. On average, the dynamic pressure is about 1.9 nPa and the proton density is about 2.8 cm^{-3}. The dominant component of the IMF is a negative B_x (GSE), i.e., a nearly radial IMF; however, the IMF B_z component remains southward, which favors B_z reconnection at the subsolar point. The geomagnetic activity index (Dst) is -18 nT with $Kp \sim 4$, indicating a moderately quiet magnetosphere.

Figure 6.3 shows Cluster measurements in the GSE coordinate system by the C1 and C3 satellites. The density of the cold ions in the magnetosphere is less than 5 cm^{-3} from the Hot Ion

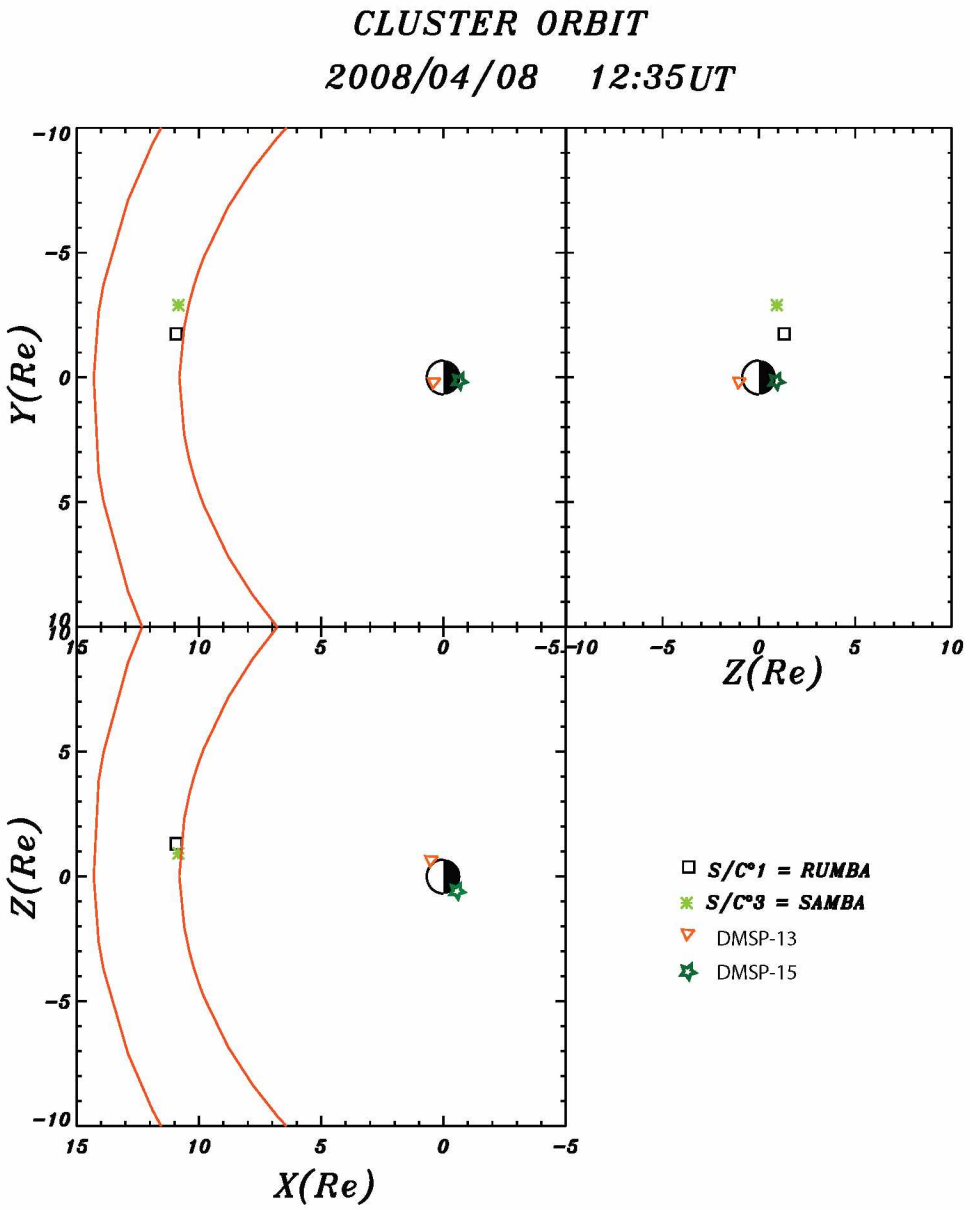

Figure 6.1. Cluster spacecraft C1, C3, DMSP F13, and F15 locations in the Y-X, Y-Z, and Z-X *GSE* plane at 12:35:00 UT on 8 April 2008. The locations of the magnetopause and the bow shock, which are determined by the Fairfield model, are marked by the red lines [*Lee et al.*, 2015a].

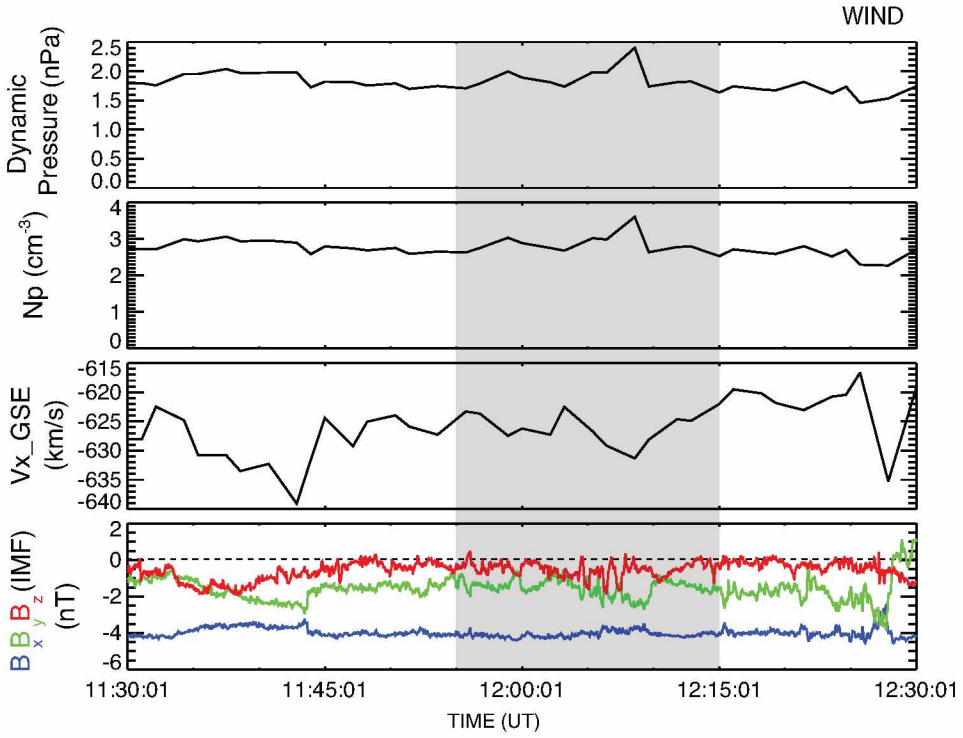

Figure 6.2. Solar wind measurements from Wind. (top to bottom) The dynamic pressure, proton density, plasma velocity V_x component, and magnetic field components in the GSE coordinate system. The shaded region marks the interval corresponding to the Cluster observations from 12:30:00 UT to 12:50:00 UT [*Lee et al.*, 2015a].

Analyzer (HIA) measurements from the Cluster Ion Spectrometry (CIS) experiment (4 s spin-resolution) [*Rème et al.*, 2001] (Figure 6.3a). The three components of the electric field from the electric field and wave (EFW) instrument (4 s resolution) are shown in Figure 6.3(b) [*Gustafsson et al.*, 1997]. The flow velocities from CIS/HIA (4 s resolution) and the magnetic fields from the fluxgate magnetometer (FGM) at a resolution of 0.004 s [*Balogh et al.*, 1997] in GSE coordinates for the interval from 12:30:01 UT to 12:50:00 UT are shown in Figures 6.3(c) and 6.3(d).

C1 and C3 encountered the magnetopause twice during the time interval from 12:30:00 UT to 12:50:00 UT, for C1 at around 12:33:04 UT and 12:43:35 UT and for C3 at around 12:32:56 UT and 12:45:24 UT. The magnetopause crossings was identified by the magnetic field rotation from its southward ($B_z < 0$, outside the magnetosphere) to its northward ($B_z > 0$, inside the magnetosphere) orientation. The northward high-speed plasma flow ($V_z > 0$) was observed in the magnetosheath boundary layer (MSBL) from 12:30:30 UT to 12:32:30 UT by C1 and from 12:32:10 UT to 12:33:30 UT by C3 (Figure 6.3c). The plasma jet speed in MSBL is higher than that of the magnetosheath flow. These factors indicate that both C1 and C3 are in the northern side of the reconnection site. [*Paschmann et al.*, 1979; *Sonnerup et al.*, 1981]. The ion energy spectrogram from CIS/HIA, high sensitivity data shows three different populations: magnetosheath (~1 keV) ions, magnetospheric ions (~20 keV), and low-energy (10–200 eV) ions (Figure 6.3e). The pitch angle distributions of cold ions changed from ~90° to broad range of pitch angles from 0° to 75° (Figures 6.3e and 6.3f). Figure 6.3(g–i) show the electron spectrogram and the pitch angle distributions for electrons with energy ranges: 5–200 eV and 0.5–1.5 keV, respectively, from the plasma electron and current experiment (PEACE), which is measured in a sequence of spins [*Fazakerley et al.*, 2010]. The pitch angle of the low-energy (5 eV–1.5 keV) electrons has a bidirectional distribution. It indicates that the magnetic field lines are closed, and the electrons are then coming from both hemispheres, or they come from the one side of the hemispheres and reflect back from the other side of the hemispheres.

6.2.2 Behavior of Cold Ions at the Dayside Magnetopause

Figure 6.4 shows the energy spectra of cold ions with 16 different pitch angles during two selected time intervals marked by black arrows in Figure 6.3 observed by C1 (a and c) and C3 (b and d). The cold ion behaviors were similar between the observations by C1 and C3. When the cold ions were close to the magnetic reconnection region, the pitch angles of the cold ions observed by both C1 and C3 were peaked at ~90° from 12:36:10 UT to 12:36:14 UT and from 12:36:09 UT to 12:36:13 UT, respectively (Figures 6.4a and 6.4b). This indicates that the cold ions move in a perpendicular direction to the magnetic field. They can be a locally trapped population (possibly, plasmaspheric plume population), which is different from the ionospheric outflow.

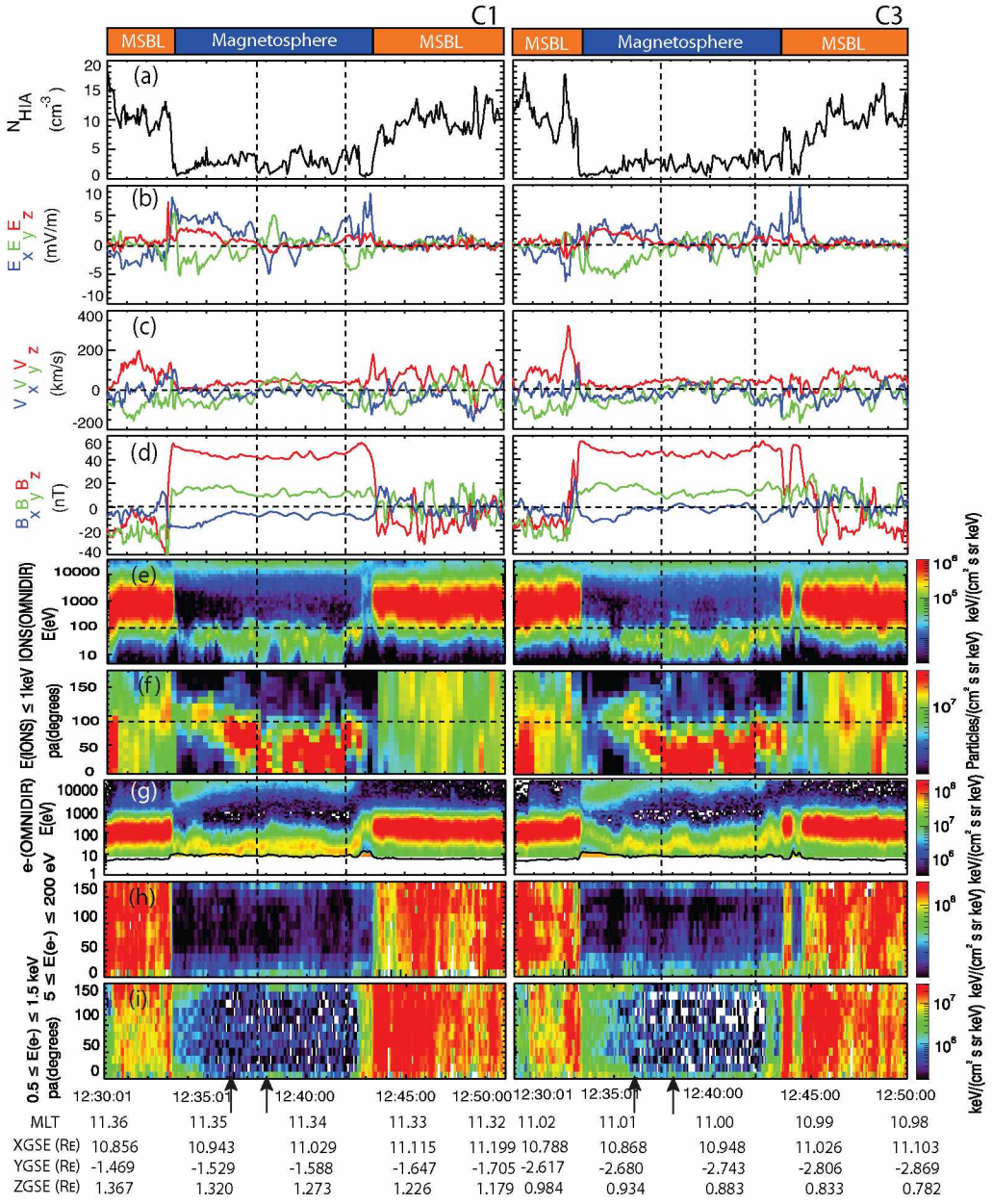

Figure 6.3. Cluster spacecraft (left) C1 and (right) C3 data from 1230 UT to 1250 UT on 8 April 2008. (a) Ion density from CIS/HIA. (b) The electric field components from EFW. (c) The velocity components. (d) The magnetic field components. (e) Ion spectrum. (f) Pitch angle distributions for low-energy (<1 keV) ions. (g) Electron spectrum. (h and i) Pitch angle distributions for electrons with the energy ranges $5 \leq E(e^-) \leq 200$ eV and $0.5 \leq E(e^-) \leq 1.5$ keV, respectively. The vertical dashed lines mark the times when the pitch angle distributions of the low-energy ions start to change (Figure 6.3f). Black arrows mark the times when the energy spectra of the cold ions in Figure 6.3 were measured [*Lee et al.*, 2015a].

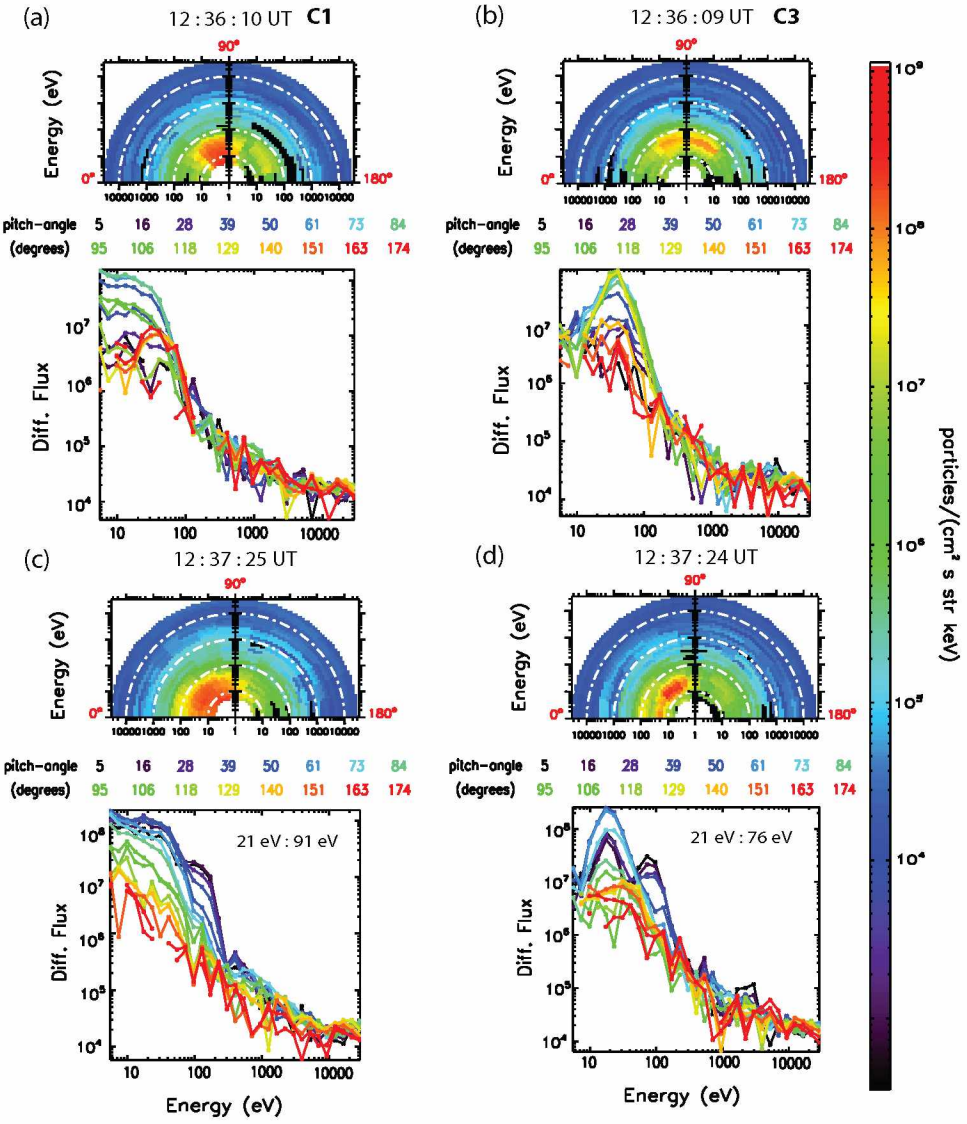

Figure 6.4. The energy spectra of cold ions with 16 different pitch angles during two selected time intervals (marked by black arrows in Figure 6.2) observed by (a, c) C1 and (b, d) C3 [*Lee et al.*, 2015a].

Figures 6.4c and 6.4d show two peaks of the differential particle flux whose pitch angles were mostly less than 50° from 12:37:25 UT to 12:37:29 UT and from 12:37:24 UT to 12:37:28 UT, respectively. The ion energy spectra from C1 and C3 were fitted by drifting Maxwellian distributions which allow us to find the energies at which the particle flux peaks. The energies of two ion flux peaks observed by C1 (C3) were found at 21 eV and 91 eV (21 eV and 76 eV), respectively, with near 0° pitch angle distribution. The two energy peaks in the ion spectra can be explained as the ionospheric outflow consisting of two ion compositions (H^+ and He^+) since the value of the second energy peak is about 4 times the first one. This is consistent with an ionospheric outflow scenario.

The cold ion (< 200 eV) flux variations were shown in the energy spectrum in the omnidirection from C1 (Figure 6.5a). Figure 6.5b shows the low-energy ion fluxes variation in the differential energy fluxes in less than 200 eV energy channels. The low-energy ion flux oscillations were highly correlated with the plasma drift velocity components V_x and V_y. The period of successive fluctuations is about 60–120 s (in the ULF wave frequency). The X_{GSE} and Y_{GSE} components of the measured ion bulk flow (black lines) are consistent with the X_{GSE} and Y_{GSE} components of the $\mathbf{E} \times \mathbf{B}$ drift velocity (red lines) calculated from the cross product of the measured electric and magnetic fields ($\mathbf{V} = \mathbf{E} \times \mathbf{B}/B^2$) (Figures 6.5c and 6.5d).

The Z_{GSE} component of the ion flow velocity (black line) is different from that of the $\mathbf{E} \times \mathbf{B}$ drift (red line) due to the presence of the field-aligned flow (Figure 6.5e). The average $\mathbf{E} \times \mathbf{B}/B^2$ velocity with $\mathbf{E}$ of 3 mV/m and $\mathbf{B}$ of 47 nT can be calculated to be 64 km/s, which is comparable with the velocity (~69 km/s) of a proton of 25 eV (the central energy of the ion spectrum from 12:33:40 UT to 12:43:00 UT is marked by the dashed line in Figure 6.5a). The average total ion flow velocity (V_t) of the cold ions in the magnetosphere from 12:33:40 UT to 12:43:00 UT is about 67 km/s (marked by the dashed line in Figure 6.5f), indicating that the cold ions are controlled by the $\mathbf{E} \times \mathbf{B}$ drift.

The low-energy ions may play an important role in the dayside reconnection. Several studies have predicted that the cold and dense plasmas may reduce the solar wind-magnetosphere coupling [*Borovsky et al.*, 2013; *Walsh et al.*, 2013]. However, *Lee et al.* [2014] suggested that cold ions have a limited effect on the reconnection process. Understanding the behavior of the cold-dense plasmas is important to address their effects on the solar wind-magnetosphere coupling, which is a goal of our future research.

6.3 Asymmetric Ionospheric Outflows

The unidirectional low-energy ions (< 200 eV) were observed by Cluster with a pitch angle distribution from 0° to 75°, revealing dominance in the parallel direction to the local magnetic field in the magnetosphere (Figures 6.3e and 6.3f). The parallel cold ion fluxes (0°–75°) were more than 100

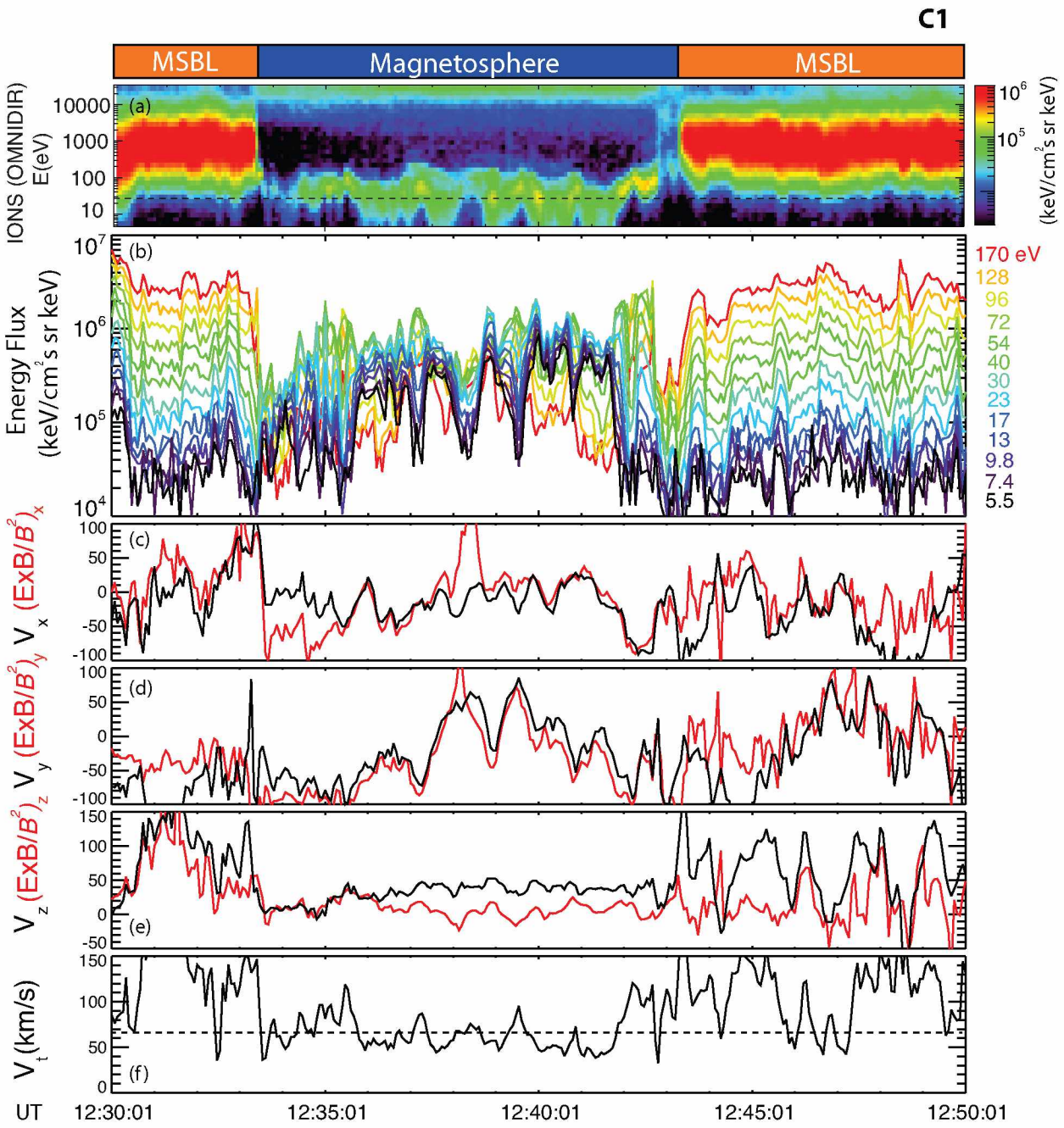

Figure 6.5. (a) Ion spectrum obtained by CIS-HIA of C1, (b) particle energy fluxes in less than 200 eV energy channels, (c–e) comparisons of X_{GSE}, Y_{GSE}, and Z_{GSE} components of ion flow velocity (black lines) with X_{GSE}, Y_{GSE}, and Z_{GSE} components of the $\mathbf{E} \times \mathbf{B}/B^2$ velocity (red lines), respectively. (f) Total ion bulk flow velocity [*Lee et al.*, 2015a].

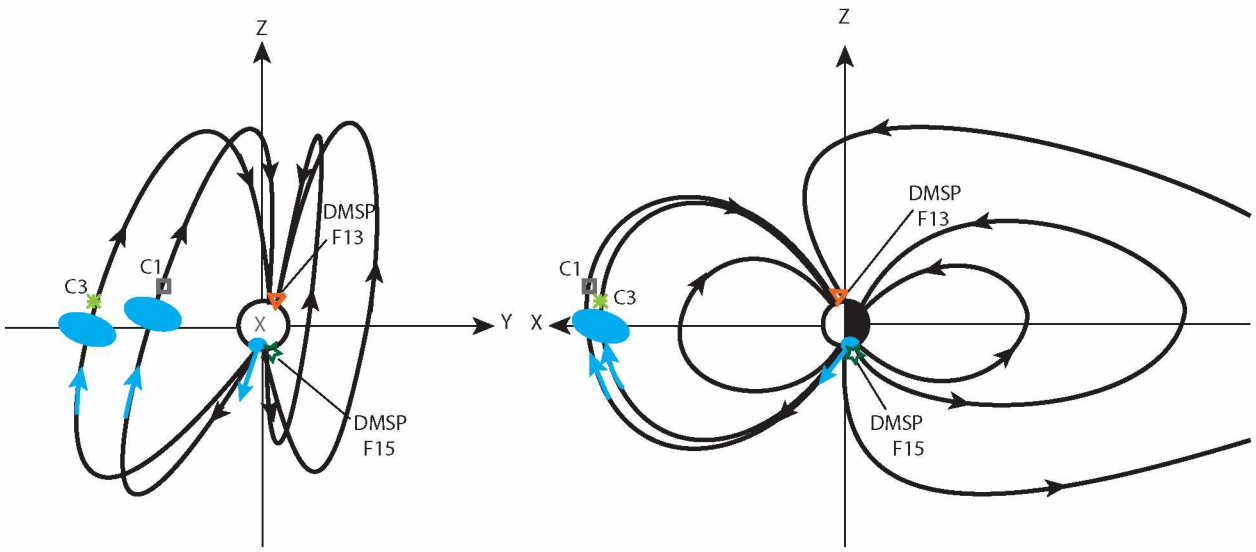

Figure 6.6. Sketch of geometry of the magnetosphere and the location of the C1, C3, DMSP F13, and DMSP F15 at 12:35:00 UT on Y-Z and X-Z plane in the GSE coordinate system. The blue arrows indicate the ion outflow from the ionosphere [*Lee et al.*, 2015a].

times higher than the antiparallel fluxes. This indicates that the Southern Hemisphere ionosphere can be the most dominating plasma source during this event.

The asymmetric ionospheric outflows at the dayside magnetopause can be due to the seasonal magnetic field geometry. During this event on 8 April 2008 (Figure 6.6), the Southern Hemisphere was in winter (darkness), and the Northern Hemisphere was in summer (sunlit). The winter hemisphere has a lower conductivity, which has been shown in statistical studies [*Laundal and Østgaard*, 2009; *Newell et al.*, 1996; *Liou et al.*, 2001]. The low conductivity drives an enhancement in the perpendicular electric field, due to closing the upward and downward Pedersen currents [*Karlsson*, 2001]. The strong perpendicular electric field causes strong frictional heating and, therefore, increases the ion temperature. Since the outflow rate is strongly correlated with the ion temperature [*Wahlund et al.*, 1992], this may cause that the ionospheric outflows come from only one hemisphere (an asymmetric ionospheric outflow).

The DMSP observations at Sun-synchronous orbit may provide some clues on the cause of the asymmetric ionospheric outflow, although the Cluster and DMSP spacecraft are not on the same field lines. The DMSP observations show that the ion temperature in the Southern Hemisphere is indeed higher than that in the Northern Hemisphere. Figure 6.7 shows plasma data taken from the Spacial Sensor-Ions, Electrons, and Scintillation (SSIES) package from the polar passes of F13 (left column) and F15 (right column) through the high-latitude regions in the Northern and Southern Hemispheres, respectively. The SSIES instrument ion drift meter (IDM) [*Rich and Hairston*, 1994] and the retarding potential analyzer (RPA) [*Rich and Hairston*, 1994; *Greenspan*

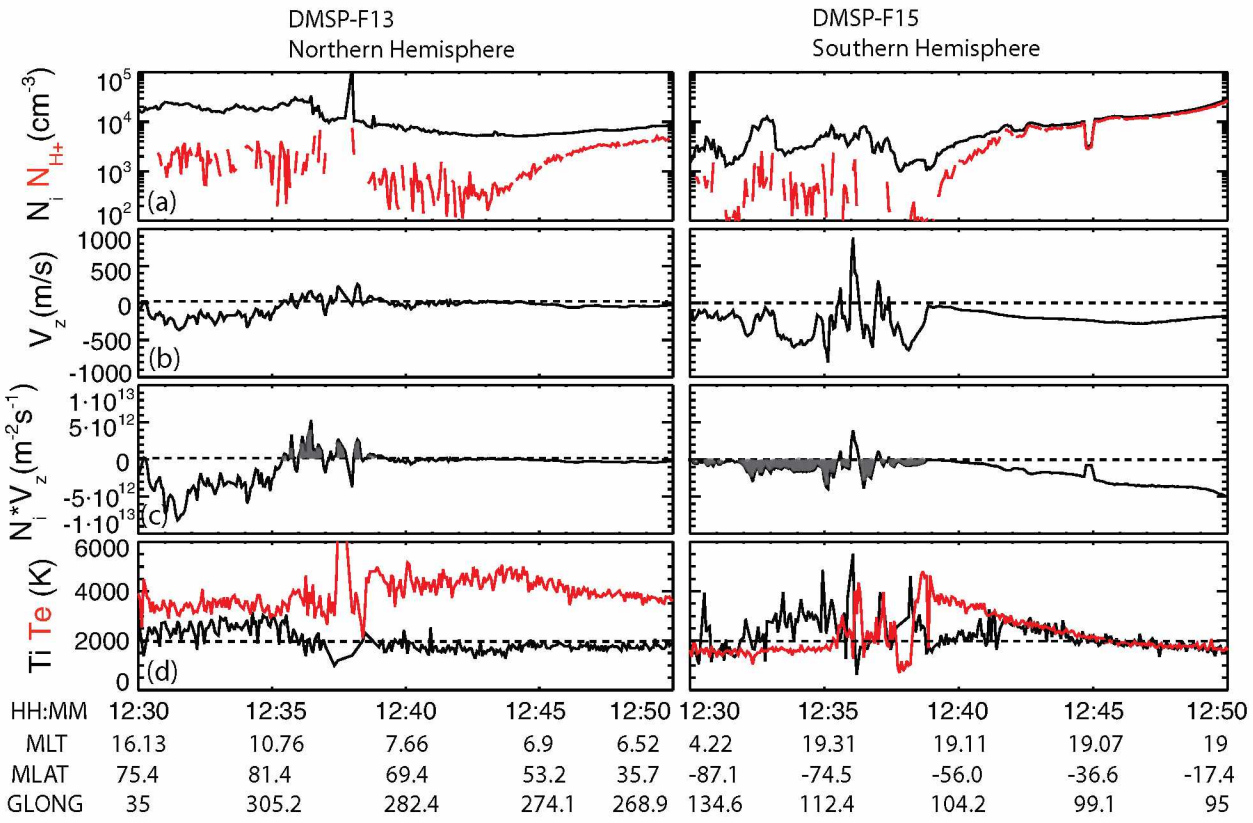

Figure 6.7. DMSP (left) F13 observations and (right) F15 observations (right) from 1230 UT to 1250 UT on 8 April 2008. (a) The total ion density (black line) and the hydrogen density (red line), (b) vertical ion velocity (positive spacecraft zenith), (c) vertical bulk ion number flux (positive spacecraft zenith), and (d) ion (black line) and electron (red line) temperatures. The shaded areas in Figure 6.7c represent the upward ion fluxes (i.e., upflows) [*Lee et al.*, 2015a].

et al., 1986] package provide density and flow data for the thermal plasma in the upper ionosphere [*Heelis and Hairston*, 1990; *Hairston and Heelis*, 1993]. In this case, V_z is positive for flows in the upward spacecraft zenith direction (Figure 6.7b). The net number flux is derived from the product of the velocity (V_z) and ion density (N_i) (Figure 6.7c). The positive vertical ion number flux in the Northern Hemisphere for the period between 12:35:25 UT and 12:39:00 UT and the negative one in the Southern Hemisphere from 12:30:00 UT to 12:36:00 UT and from 12:36:20 UT to 12:39:00 UT are the upward ion fluxes, shown shaded in Figure 6.7c. Figure 6.7d shows that the DMSP ion temperature measurements. The ion temperature (black line) in the Southern Hemisphere is much higher than that in the Northern Hemisphere when the upward ion fluxes are seen. The DMSP RPA and IDM data from 12:40:00 UT to 12:50:00 UT are not reliable.

The outward ionospheric fluxes in the Southern Hemisphere observed by F15 at 850 km, $-70°$ magnetic latitude (MLAT) are about 2.0×10^8 cm^{-2}s^{-1} around 1900 magnetic local time (MLT) (Figure 6.7c, right). The upflowing ion fluxes vary in MLT and in invariant latitude about a factor

of 4 [*Yau et al.*, 1985; *Delcourt et al.*, 1989]. The average ionospheric upflow flux estimated to be 6.0×10^8 cm^{-2}s^{-1}. Assuming all upflows have sufficient energy to become outflows, the total outflow can be derived by multiplying the mean value of the ionospheric flux with the outflow area, which is 2.1×10^{17} cm^2 assuming that the outflow area is bounded by $-70°$ MLAT in the Southern Hemisphere. Then the calculated total outflow is about 1.3×10^{26} ions/s. Approximately 50% of the total ion outflow of ionospheric origin reaches the dayside magnetosphere [*Cully et al.*, 2003a]. The average ion density of ionospheric origin in the dayside magnetosphere can be calculated using the equation, Density = (Ionospheric source flux × Residence time)/Volume [*Chappell et al.*, 1987]. The average residence time of 6 h (2.16×10^4 s), which determined by drift time for a flux tube across the dayside, is based on the typical convection models. The volume 5.65 $\times10^{29}$ was from *Lyons and Williams* [1984] and estimated using a dipolar magnetic field approximation. Therefore, the calculated ion density resulting from the ionospheric outflow in the dayside magnetosphere is about 2.5 ions/cm^3. The average ion densities (2.9 ions/cm^3 and 2.4 ions/cm^3) observed by C1 and C3, respectively, match with the calculated ion density given by an ionospheric source. This indicates that ionospheric outflows can contribute most of the volume of the dayside magnetosphere that is consistent with the estimation by *André and Cully* [2012], who showed that the ionospheric source is dominant in the dayside magnetosphere at least 50–70% of the time. However, there may be large error bars for estimating the ion density of the ionospheric origin due to the combination of several highly variable quantities.

It should be pointed out that these observed cold ion fluxes vary with the $\mathbf{E}\times\mathbf{B}$ drift with a period of 60–120 s, which is in the ULF wave range. A possible scenario is that ULF waves generated at the foreshock region [*Volwerk*, 2006] can be convected into the magnetopause region and further caused the flux modulations of the ionospheric origin cold ions. During the time of interest, the angle between the IMF and the bow shock normal is ∼180°, which is the favorable condition of the ULF wave generated in the foreshock region.

6.4 Summary and Conclusions

We have presented Cluster observations of the ionospheric outflows at the dayside magnetopause on 8 April 2008. The unidirectional low-energy (< 200 eV) ions with pitch angles from 0° to 75° were observed by C1 and C3 inside the magnetopause. The cold ion fluxes (< 200 eV) modulations were correlated with the plasma drift velocity ($\mathbf{E}\times\mathbf{B}$).

The main results of this chapter can be summarized as follows:

1. The observed cold ion fluxes that have a dominant form of parallel fluxes were much larger than those of the antiparallel fluxes. The cold ions that have 0°–75° pitch angle distributions can be coming directly from the ionosphere in the Southern Hemisphere and reached to the

dayside magnetopause.

2. The bidirectional pitch angle distributions of the low-energy electrons (up to 1.5 keV) confirms that magnetic field lines are closed.

3. The asymmetric ionospheric outflows observed at the dayside magnetopause can be caused by the seasonal magnetic field geometry effect.

4. The ionospheric outflow consists of two different species (possibly H^+ and He^+) since there are two ion flux peaks in the ion energy spectra from C1 to C3, and the energy of the second peak is about 4 times the first one.

5. The cold ion (< 200 eV) fluxes are modulated by the ULF wave at the period of 60–120 s.

A statistical study of the ionospheric outflows observed near the dayside magnetopause is presented in Chapter 7.

Chapter 7
A Statistical Study of Plasmaspheric Plumes and Ionospheric Outflows Observed at the Dayside Magnetopause

7.1 Introduction

There are two types of low-energy plasma populations that can dominate the dayside magnetosphere: plasma of plasmaspheric origin (plasmaspheric wind, blob and plume) and of ionospheric origin (ionospheric outflow and warm plasma cloak). The low-energy, dense plasma of these two origins supplies particles to the cavity of the magnetosphere and can extend to a distance near the magnetopause. Figure 7.1 shows a sketch of several low-energy plasma populations that can be observed near the dayside magnetopause.

The plasmaspheric plasma can expand beyond the plasmapause in the form of the blobs, the plume, and the plasmaspheric wind. The drainage plume is the extension of the outer region of the plasmasphere [*Chen and Wolf*, 1972; *Lemaire*, 2000; *Green et al.*, 2002; *O'Brien and Moldwin*, 2003]. When the interplanetary magnetic field (IMF) turns southward, the plasmapause that is formed by the combination of the corotational and solar wind driven convection electric fields moves inward across the nightside and a sunward bulge is out near the duskside. Since for southward IMF the sunward convection is enhanced across the dayside magnetosphere, a distinct plasmaspheric plume can be formed at the duskside [*Goldstein et al.*, 2003]. The blobs are formed when the plasmaspheric plasma is detached from the plasmasphere [*Chappell*, 1974]. *Goldstein et al.* [2004] suggested that a blob of plasmaspheric plasma could be formed when the plume moved outward and became isolated. The plasmaspheric wind is a continuous plasmaspheric plasma release from the plasmasphere to the magnetosphere across the geomagnetic field lines during quiet and moderately active geomagnetic conditions (K_p <3) [*Dandouras*, 2013].

There are four possible source regions of the ionospheric outflow: the auroral region, the cleft ion fountain, the polar cap, and the polar wind, which are classified based on their locations and energy distribution functions. The ionospheric ions can be accelerated by the ambipolar electric field arising from a pressure gradient of thermal electron or by the electric field caused by the spatial separation between the electrons and heavy ions so that the light ions can escape from the polar ionosphere. This is one of the possible mechanisms that can generate the ionospheric ion outflow from the polar cap regions [*Yau and André*, 1997; *Yau et al.*, 2007]. There are two types of plasma of the ionospheric origin: the ionospheric outflow and the warm plasma cloak. The ionospheric outflow is directly from one or both hemispheres. The warm plasma cloak is formed when the ionospheric outflow is transported toward the nightside and then brought back to the dayside magnetosphere by $\mathbf{E}\times\mathbf{B}$ convection. The warm plasma cloak has an intermediate energy (a

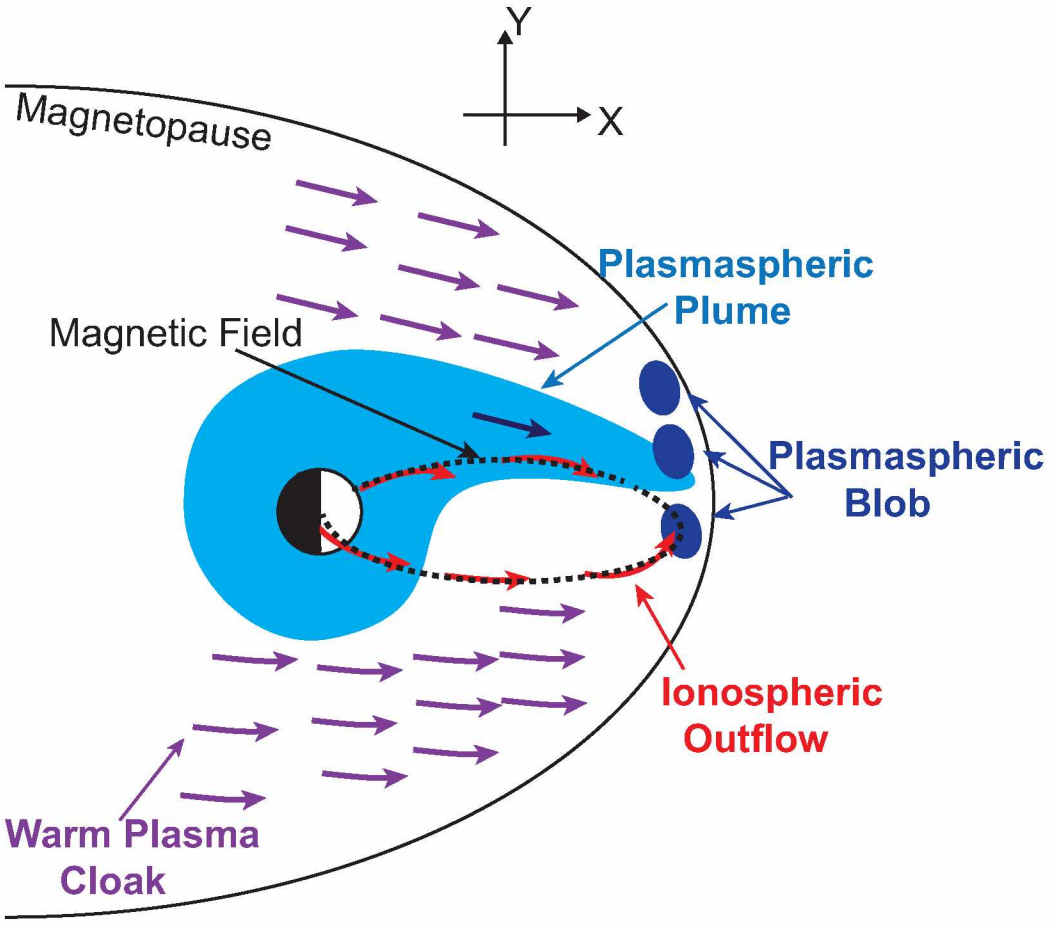

Figure 7.1. A sketch of the major low-energy ion populations that can be observed in the dayside magnetosphere [*Lee et al.*, 2015b].

few eV to hundreds of eV), which is greater than the energy of a direct upward outflow and lower than that of the populations in the plasma sheet or ring current [*Chappell et al.*, 2008]. Both the ionospheric outflow and the warm plasma cloak have unidirectional or bidirectional field-aligned ion pitch angle distributions.

The plasmaspheric plumes have been identified using several methods. The plumes were identified when their densities were beyond the model values at different L shells using the empirical models of *Sheeley et al.* [2001] with the CRRES data set at the geosynchronous orbit [*Moldwin et al.*, 2004] and with the THEMIS measurements at the dayside magnetopause [*Walsh et al.*, 2013]. *Chen and Moore* [2006] identified the plasmaspheric drainage plume when its peak energy is above the spacecraft potential (a few eV) and below the upper energy limit of the instrument (~400 eV), and when the flow is perpendicular to the magnetic field. They used the measurements from the Thermal Ion Dynamics Experiment on the Polar spacecraft (TIDE/Polar) orbiting in the dayside outer magnetosphere beyond geosynchronous distances. *Darrouzet et al.* [2008] characterized the plume crossings when the electron density, which is derived from the electron plasma frequency, is greater than the background electron density. The electron plasma frequency is obtained by the WHISPER instrument onboard Cluster. *André and Cully* [2012] identified the plasmaspheric drainage region where high density (up to a few tens cm^{-3}) low-energy ions were observed while the Cluster spacecraft crossed the magnetopause.

The ionospheric outflows have been observed by several satellites [*Yau et al.*, 1986; *Peterson et al.*, 2001; *Andersson et al.*, 2005; *Cully et al.*, 2003b; *Redmon et al.*, 2012]. *Peterson et al.* [2006] identified the ionospheric outflows when the peak fluxes were greater than 10^{10} ions/m^2·s·sr and their ion distributions had less than 90° pitch angle distributions from the Southern Hemisphere. The data was recorded by the Toroidal Ion Mass-Angle Spectrograph (TIMAS) instrument on the Polar satellite with a mean altitude of about 7500 km during solar minimum. The ionospheric outflows can be classified in terms of their pitch angle distributions: beam, conic, and upflowing ions (UFI) [*Peterson et al.*, 2006]. An ion beam is defined as an ion distribution which has a peak flux along the upward direction of the local magnetic field (from 0° to 30° pitch angle distributions) and an ion conic that has pitch angles with peaks in the range of 30° to 75°. The UFI is defined as the combination of beams and conics so that it has a peak flux in the range of 0° to 75° pitch angle distributions. The warm plasma cloak has been observed in the dayside magnetosphere by the ATS, ISEE, SCATHA, DE, and Polar satellites [*Lennartsson and Reasoner*, 1978; *Baugher et al.*, 1980; *Nagai et al.*, 1983; *Fennell et al.*, 1981; *Kaye et al.*, 1981; *Sagawa et al.*, 1987; *Giles et al.*, 1994; *Chappell et al.*, 2008].

Density ranges with both the plumes and outflows; their spatial distribution and the dependence of their occurrence rates on the geomagnetic activities and solar wind/IMF conditions have been

studied. Density of the plumes varies from a few to a few hundred cm^{-3}, depending on their locations (L shell and latitude) [*Chappell*, 1972; *Sauvaud et al.*, 2001; *Walsh et al.*, 2013]. *Chen and Moore* [2006] found that significantly more plasmaspheric plume events, observed by TIDE/Polar near polar apogee (> 5 R_E), occurred at the duskside than at the dawnside. *Darrouzet et al.* [2008] showed that the plasmaspheric plume events were observed mostly for moderate K_p (= 3–6) and not for small D_{st}.

The densities range of the warm plasma cloak ions is from 0.5 to 3 cm^{-3}, observed by TIDE near Polar apogee [*Sagawa et al.*, 1987; *Chappell et al.*, 2008]. These ions are found more often at the dawnside than the duskside. *Nagai et al.* [1983] found that the occurrence rate of the ionospheric outflows (< 100 eV), measured by the Plasma Composition Experiment on board ISEE in the range of $L = 3$–10, increased with decreasing K_p. *Cully et al.* [2003b] showed that the ionospheric outflow rates were strongly correlated with the solar wind dynamic pressure, the solar wind electric field, and variation in the IMF.

Observations of plasmaspheric plume and ionospheric outflow at different locations in the magnetosphere using various spacecraft data have been reported [e.g., *Chen and Moore*, 2006; *Chappell et al.*, 2008; *Walsh et al.*, 2013]. However, there is no study on the characteristics of both plumes and outflows near the magnetopause. These low-energy populations can play an important role in the magnetospheric dynamics, such as magnetic reconnection. In this chapter, we use Cluster in situ measurements to identify low-energy ions of ionospheric origin (called "ionospheric outflow" in this chapter) and plasmaspheric origin (called "plasmaspheric plume" in this chapter) observed at the dayside magnetopause. We compare their densities, spatial distributions and dependences of the occurrence rates on the solar wind/IMF conditions and geomagnetic activity.

7.2 Identifications of the Plume and Outflow Events

The low-energy (< 1 keV) ion events observed near the magnetopause were selected on the basis of two criteria. (1) We only selected the events when the low-energy ion particle energy flux was greater than 10^5 keV/(cm^2s·sr·keV). To be detected, the energy of the cold ions must be larger than the threshold of the HIA/CIS instrument (5 eV). (2) The cold ions were present for longer than 2 min. The plasmaspheric plumes can be distinguished from the ionospheric outflows by using the ion pitch angle distribution. The plasmaspheric plume ions have ~90° pitch angle distributions (perpendicular to the magnetic field). The plume is formed when the strength of the convection electric field suddenly increases. Increasing convection causes the duskside bulge of the plasmasphere along the open-drift paths [*Goldstein et al.*, 2005]. Thus, a large amount of cold ions drift to the dayside magnetopause. The drift associated with the enhanced convection electric field is perpendicular to the magnetic field. In contrast, the pitch angle distributions for the outflows

from one or both hemispheres are mostly 0° and/or 180° peaked (unidirectional or bidirectional pitch angle distributions), i.e., the ionospheric outflows are field-aligned flows [*Horwitz et al.*, 1982; *Chappell et al.*, 2008].

Figure 7.2 represents data for a plume case (left) and an outflow case (right) observed by C3 from 03:00 to 05:00 UT on 10 February 2007 and from 05:00 to 07:00 UT on 06 March 2008, respectively. The C3 satellite was located at (X, Y, Z)$_{GSM}$ = (9.86, 6.10, 4.75) R_E for the plume event at 03:00 UT and (X, Y, Z)$_{GSM}$ = (10.27, 2.94, 2.70) R_E for the outflow event at 05:00 UT. From top to bottom, the ion energy spectrum, the ion (< 1 keV) pitch angle distribution, ion density, electron density derived from the spacecraft potential, the ion velocity moments V_x (blue), V_y (green) and V_z (red) (km/s), and the three magnetic field components B_x (blue), B_y (green) and B_z (red) (nT) in geocentric solar magnetospheric (GSM) coordinates are shown during two-hour time intervals.

The low-energy (< 1 keV) ions were observed in the magnetosphere by C3 for both plume and outflow events (Figure 7.2a). There are large ion energy spectra fluctuations in the plume event and the energy-dispersion signature in the outflow event. Figure 7.2(b) shows that the plume has a 90° pitch angle distribution and the outflow has a bidirectional field-aligned pitch angle distribution. The average ion densities are 0.8 cm^{-3} for the plumes and 0.4 cm^{-3} for the outflows (Figure 7.2c). There are large ion density variations in the plume event. The average electron densities are 5.0 cm^{-3} for the plumes and 4.1 cm^{-3} for the outflows (Figure 7.2d). The ion densities are lower than the electron densities because the cold ions with energy lower than 5 eV (threshold of HIA) cannot be detected by the instrument. The ion and electron densities for the plumes are higher than those for the outflows.

Figure 7.2(e) shows that the accelerated plasma flows V_z (plume) and V_y (outflow) reach about 300 km/s and 200 km/s in the boundary layer, respectively, which are the typical signature of magnetic reconnection. For the plume event, the accelerated ion jet V_z switched direction at 04:05 UT, indicating that C3 crossed the reconnection site to the other side of the X-line. The plume occurred during southward IMF condition. The average IMF B_z was −1.7 nT, which was obtained from the 5-min averaged OMNI data set available at OMNIWeb. For the outflow event, the averaged IMF B_z was 0.9 nT (northward IMF condition) and the y component of the magnetic field changed from positive (∼10 nT) to negative (∼ −15 nT) where the high-speed flow jet V_y was shown. The averaged IMF B_y for the outflow event was −1.0 nT.

While C3 encountered 442 dayside magnetopause crossings starting from January to May and December in 2007–2009, 43 plume events and 32 outflow events were observed based on the criteria listed at the beginning of this section. There were 7 events that consisted of both plume and outflow during each magnetopause crossing. We statistically examined the occurrence rate of the

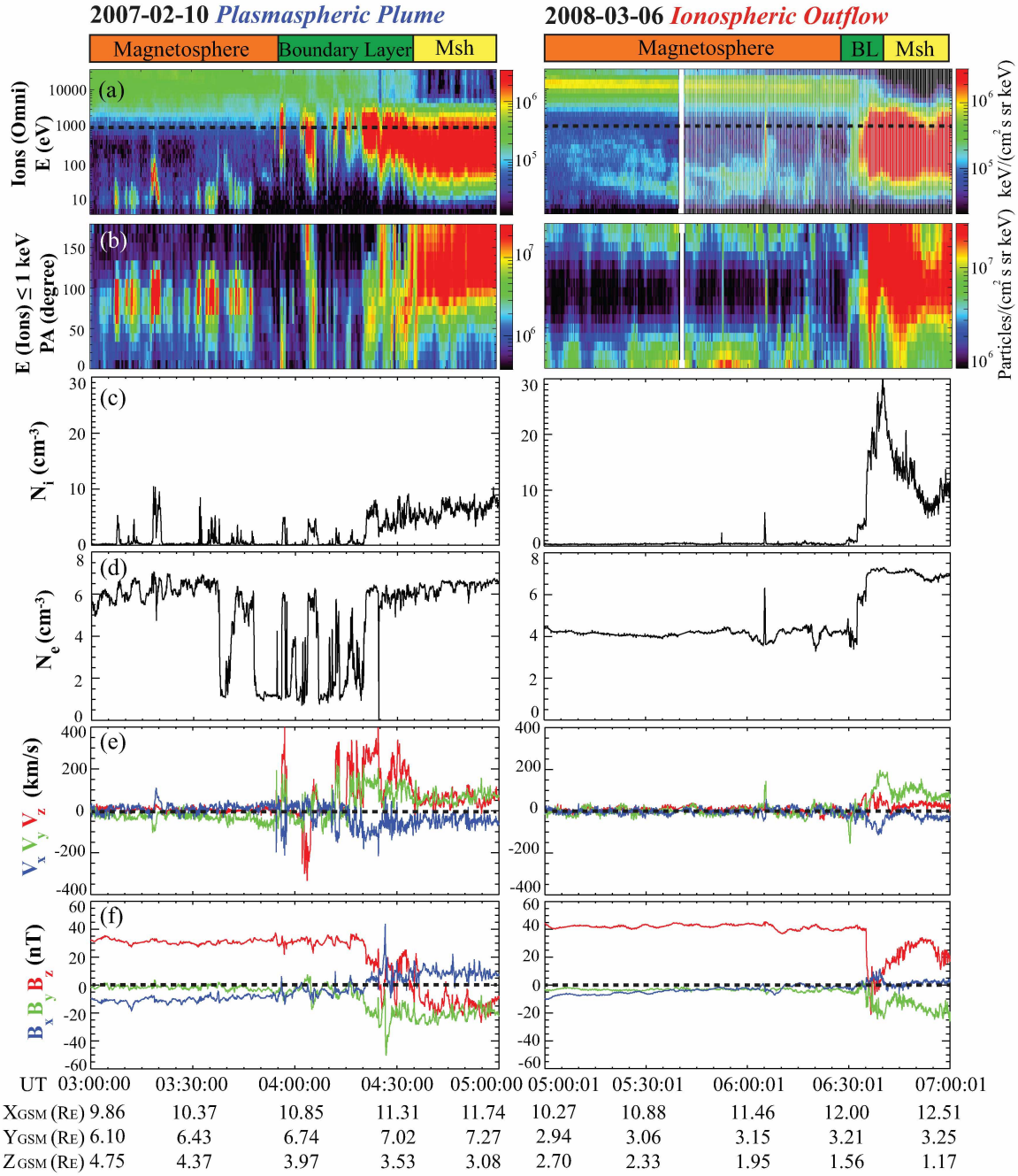

Figure 7.2. Examples of a plume case (left) and an outflow case (right) near the dayside magnetopause observed by C3. (a) HIA omnidirectional energy-time spectrogram in energy flux units (no mass discrimination), (b) the pitch angle distribution for low-energy ions (< 1 keV), (c) ion density, (d) electron density from the spacecraft potential, and (e) the three velocity and (f) magnetic field components in GSM coordinates, respectively [*Lee et al.*, 2015b].

plumes and the outflows and their dependence on the geomagnetic activities and solar wind/IMF conditions. We also compared the characteristics of the plasmaspheric plume and the ionospheric outflow.

7.3 Results

7.3.1 Occurrence Rate of the Plumes and the Outflows

Based on the C3 measurements from the 18 months of intermittent observation (from January to May and December) during 2007 to 2009, Figure 7.3 shows the distribution of the plasmaspheric plumes (blue) and the ionospheric outflows (red) in GSM coordinates. During those three years, we have identified 43 (10%) plasmaspheric plume events and 32 (7%) ionospheric outflow events when Cluster crossed the dayside magnetopause (442 magnetopause crossings). Low-energy ions were detected in 15% (68 of 442) of the dayside magnetopause crossings (both plume and outflow were observed for 7 magnetopause crossings).

The occurrence rates of the plume (10%) and the outflow (7%) are less than those from other statistical studies. *Walsh et al.* [2013] showed that 12.5% of the plumes were observed at the dayside magnetopause by THEMIS and *Darrouzet et al.* [2008] showed that 15% of the plasmasphere passes were observed by the Cluster spacecraft in between 4 and 11 R_E. 30% plasmaspheric-like plasma (169 of the 558 plasmapause crossings) were observed by CRRES outside the plasmapause [*Moldwin et al.*, 2004]. *André and Cully* [2012] showed that the outflow of low-energy ions can dominate 50–70% of the time on the dayside magnetosphere. In our study, the plasmaspheric plume and the ionospheric outflow were identified in the CIS/HIA data, which may lead to lower occurrence rates of the low-energy ions since the cold ions with energy lower than the threshold (5 eV) of the detector cannot be detected.

The plume and outflow events were detected in 15% of dayside magnetopause crossings and 76% (57 of 75) of these events were observed at the duskside. 91% of the plume events were detected at the duskside, while only 9% were observed at the dawnside. This is consistent with the predictions from the theoretical models and global empirical models showing that the plumes appear at the duskside as geomagnetic activity increases [*Chappell et al.*, 1970, 1971; *Carpenter et al.*, 1992]. The occurrence rate of the outflow (red) events at the duskside (18 events) is slightly higher than that at the dawnside (14 events), indicating that the outflow events have a weak dawn-dusk asymmetry.

7.3.2 Density Differences

Densities of plumes and outflows vary depending on where they were detected and on the geomagnetic activity or solar wind/IMF conditions. Here, we focus on the cold ion observations near the

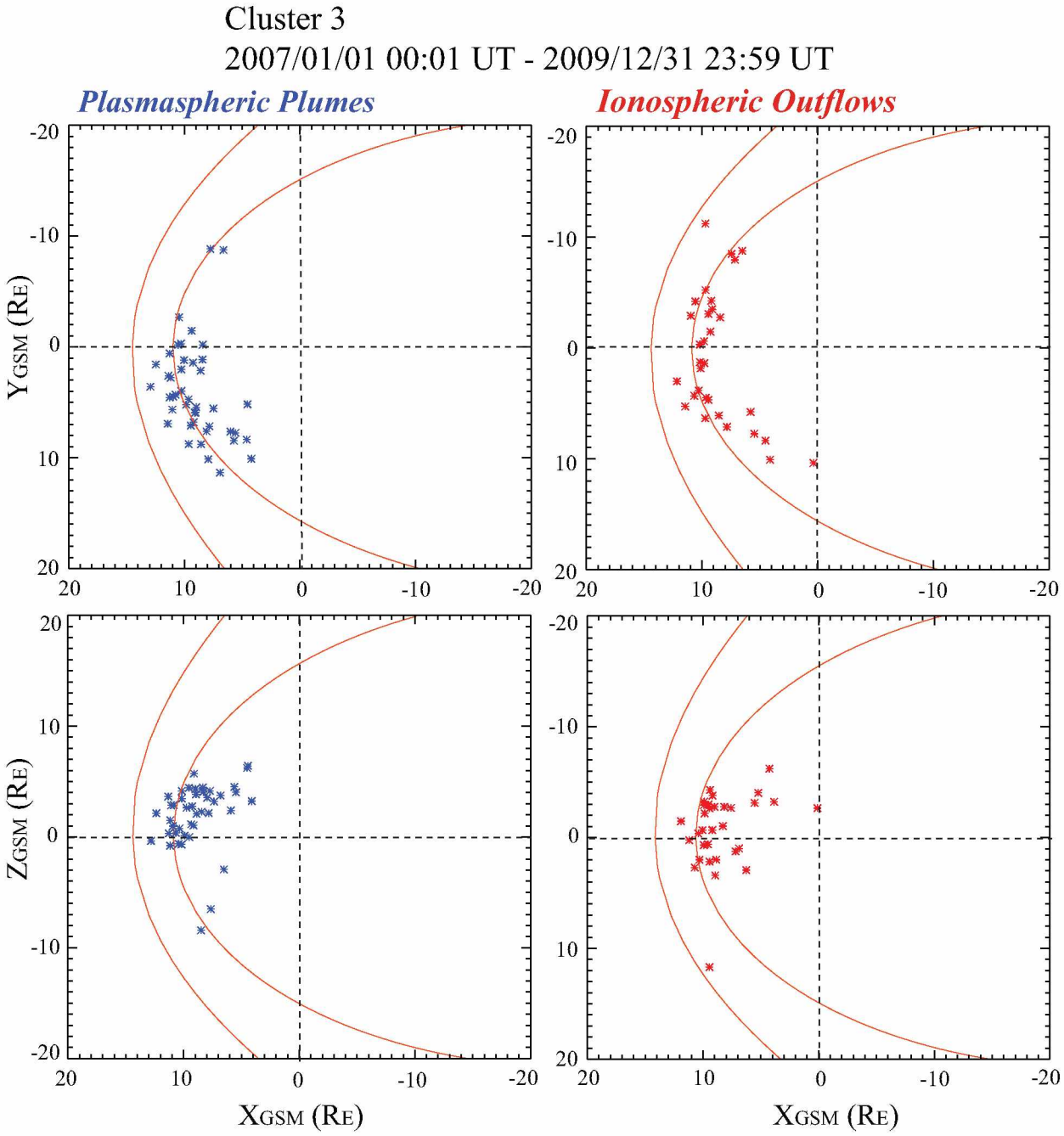

Figure 7.3. Distributions of plasmaspheric plumes (blue) and ionospheric outflows (red) as detected by Cluster 3 while crosses the dayside magnetopause. The data is plotted in the GSM coordinate system X-Y and X-Z planes. The red lines represent the bow shock (outer) and the magnetopause (inner), which are determined by the Fairfield model [*Lee et al.*, 2015b].

magnetopause and compare ion and electron densities of plumes and outflows. Figure 7.4 shows bar plots of the electron density (Figure 7.4a) obtained through the spacecraft potential measurements from the EFW experiment on Cluster and the ion density (Figure 7.4b) from the CIS/HIA ion spectrometer for the plumes (blue) and the outflows (red) observed by C3 from 2007 to 2009. We used the formula for 2001 observations in *Pedersen et al.* [2008] for a statistical study of the electron density. The densities were averaged during the time period when the low-energy ions were observed. The bin size in all bars is 0.5 cm^{-3}.

The median values of the electron density of plume and outflow events are 5.4 cm^{-3} and 5.2 cm^{-3}, respectively. This indicates that there is no clear difference in the electron density between the plume and the outflow events. The ion density distributions of both the plumes and the outflows peak at the density range from 0.5 to 1.0 cm^{-3}, and the plume ion density distribution only occasionally reaches the density range from 7 to 7.5 cm^{-3}. The median ion densities of the plumes and the outflows are 0.9 cm^{-3} and 0.7 cm^{-3}, respectively. The electron densities are higher than the ion densities because the cold ions with energy lower than the threshold (5 eV) of CIS/HIA instrument cannot be detected.

7.3.3 Dependence on Geomagnetic Activity

We examined the relationships between the low-energy ions of two different origins and geomagnetic disturbances. Figure 7.5 shows the occurrence rates of the plumes and the outflows with their corresponding magnetic activities as indicated by the three-hour index K Planetary (K_p) (left column) and the hourly index Disturbed Storm Time (D_{st}) (right column). The K_p index is expressed in (0, 1, 2, 3, etc.) and each of the index values contains a scale of thirds (0, 0+, 1−, 1. 1+, 2−, 2, 2+, etc.). We defined the K_p values 0 – 3 as quiet or moderately active magnetospheric conditions, and values greater than 4 as disturbed conditions. D_{st} values greater than 0 correspond to geomagnetically quiet periods, between 0 and −20 nT correspond to moderate periods, and below −20 nT to disturbed periods [*Li et al.*, 2012]. The maximum K_p in the previous 12 hours was selected and the minimum D_{st} value in the previous 24 hours was chosen when the plumes and the outflows were observed by C3 during magnetopause crossings [*Moldwin et al.*, 2004; *Darrouzet et al.*, 2008].

Figures 7.5(a) and 7.5(d) show the K_p and D_{st} distributions when C3 crossed the magnetopause (442 crossings) during selected periods, from January to May and December 2007, 2008, and 2009, respectively. The K_p and D_{st} distributions are shown from 0 to 4 and from +10 to −50, respectively. There are only a few magnetopause crossings observed by C3 with high K_p (> 4) and very low D_{st} (< -50) during the selected time intervals. Figures 7.5(b) and 7.5(e) show the distributions of plumes (blue) and outflows (red) as a function of K_p and D_{st}, respectively. Figures 7.5(c) and

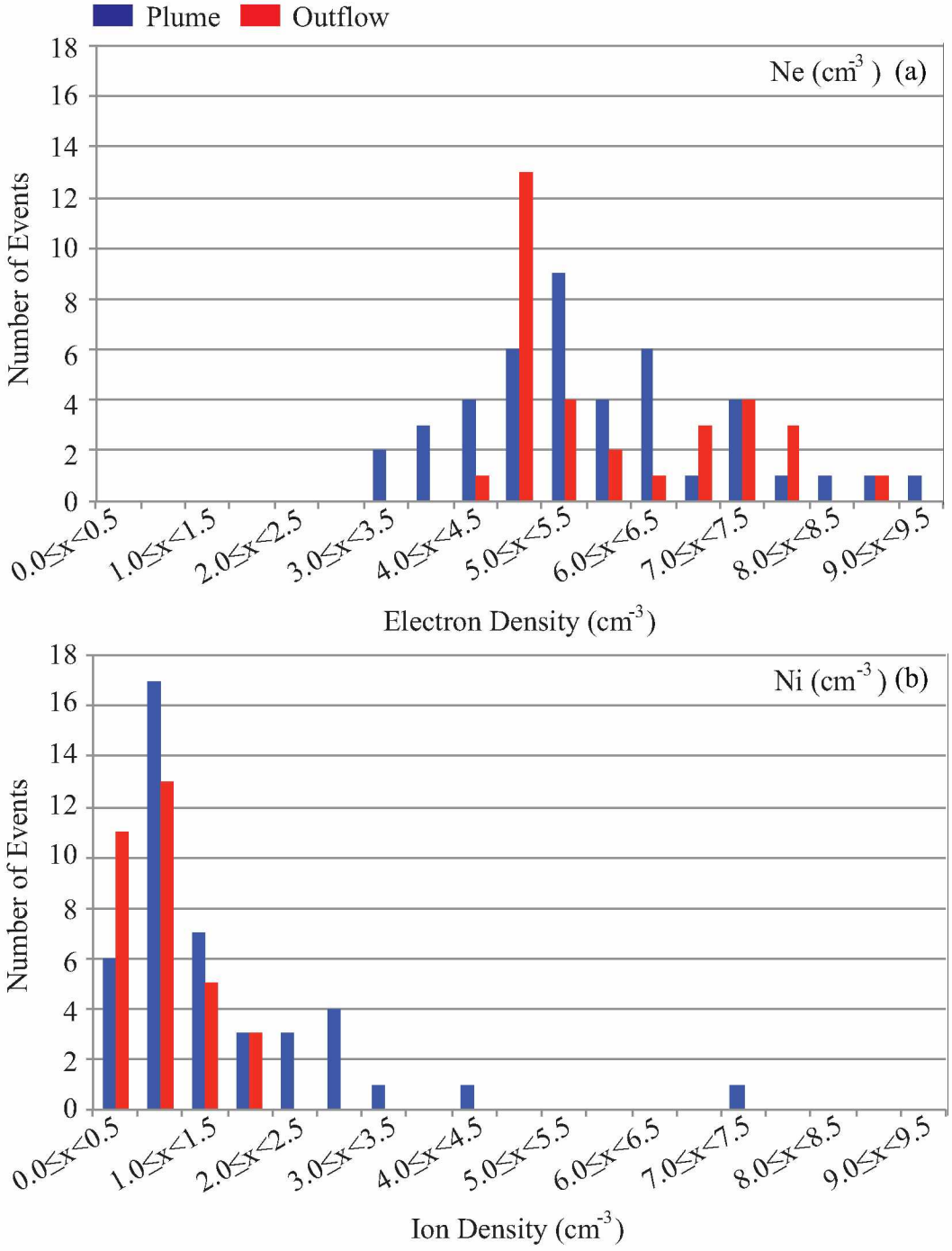

Figure 7.4. Distributions of plume and outflow events as a function of (a) electron density and (b) ion density [*Lee et al.*, 2015b].

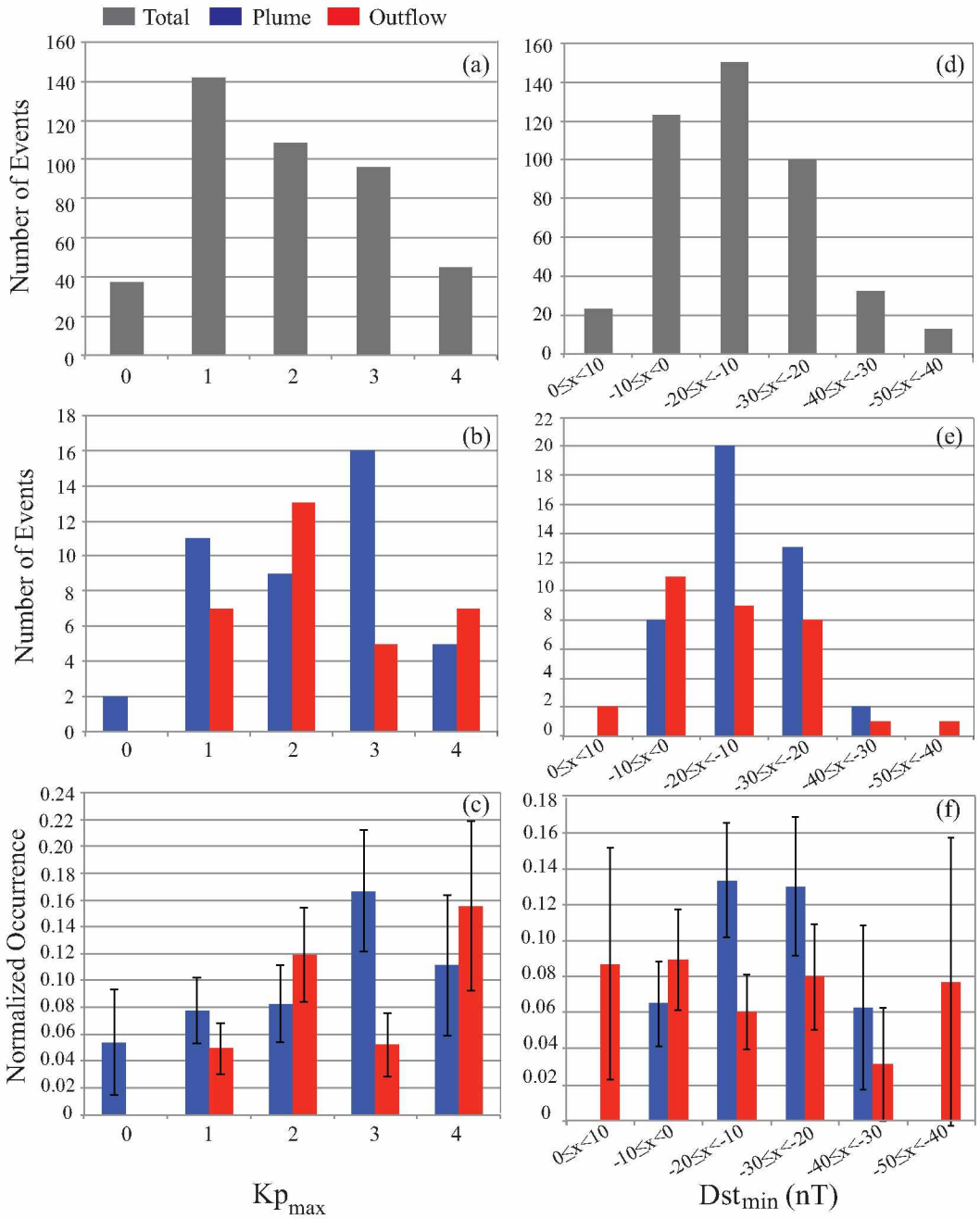

Figure 7.5. Distributions of geomagnetic activity as indicated by (a) maximum K_p in the previous 12 hours and (d) minimum D_{st} in the previous 24 hours for a total of 442 magnetopause crossings. Distributions of plume (blue) and outflow (red) events as a function of (b) K_p and (e) D_{st}. The normalized occurrence rates of plume (blue) and outflow (red) events as a function of (c) K_p and (f) D_{st} [*Lee et al.*, 2015b].

7.5(f) show the normalized distributions (taking into account the distributions of K_p and D_{st} for all 442 magnetopause crossings) of plumes (blue) and outflows (red) versus K_p and D_{st}, respectively.

We noted that no plumes and outflows were observed for the highest K_p (> 4) and the lowest D_{st} (< -50). The normalized distributions show that the plume events prefer to occur during moderate geomagnetic activity ($K_p = 3$ and $-30 \leq D_{st} < -10$ nT), which is consistent with statistical study results of *Darrouzet et al.* [2008], who showed that more plasmaspheric plume events were observed during moderate activity (K_p between 3+ and 6) from 1 February 2001 to 1 February 2006. The ionospheric outflow events do not occur when $K_p = 0$ and the occurrence rate of the ionospheric outflows does not have clear D_{st} dependence. *Li et al.* [2012], however, showed that the elevated ionospheric outflow fluxes were observed near the dayside cusp region and the nightside auroral region during disturbed magnetospheric conditions ($D_{st} < -20$ nT). This difference may be caused by the different locations where the low-energy ions were observed.

7.3.4 Dependence on Solar Wind Parameters

In order to investigate the dependence of the occurrence rates of the plumes and outflows on different solar wind parameters, we used the 5-min averaged multi-spacecraft OMNIweb data during the selected time period. The OMNIWeb (http://omniweb.gsfc.nasa.gov) combines data from multiple spacecraft (WIND, Geotail, IMP, and ACE) and provides a high resolution database of IMF and solar wind conditions. The OMNI data sets are time-shifted taking into account the solar wind propagation time from the spacecraft to the Earth's bow shock. Figures 7.6(a) and 7.6(d) show the distributions of the IMF B_z and derived E_y (= -$v_{sw} \times B_z$) for all the dataset from 2007 through 2009, respectively. Figures 7.6(b) and 7.6(e) show the distributions of the plumes (blue) and outflows (red) as a function of IMF B_z and the derived solar wind electric field (E_y), respectively. The normalized occurrence rates of the plumes (blue) and outflows (red) as a function of IMF B_z and E_y are shown in Figures 7.6(c) and 7.6(f), respectively.

The normalized occurrence rate of the plumes rises slowly with increasing negative values of IMF B_z, whereas the one for the outflow events tends to rise as the positive IMF B_z values increase (Figure 7.6c). The normalized occurrence rates of the plume and outflow events increase as positive and negative values of E_y increase, respectively (Figure 7.6f). These indicate that the plume events tend to occur during southward IMF (duskward solar wind electric field), whereas the outflow events prefer to occur during northward IMF (dawnward solar wind electric field).

Figure 7.7 shows the distribution of the plumes (blue) and outflows (red) when (a) IMF $B_y > 0$ and (b) IMF $B_y < 0$ in the GSM X-Y plane. About 65% of the low-energy ion (plume and outflow) events were observed during positive IMF B_y, while only 35% were observed during negative IMF B_y. Notably, significantly more outflows (red) were observed during positive IMF B_y (24 of 32,

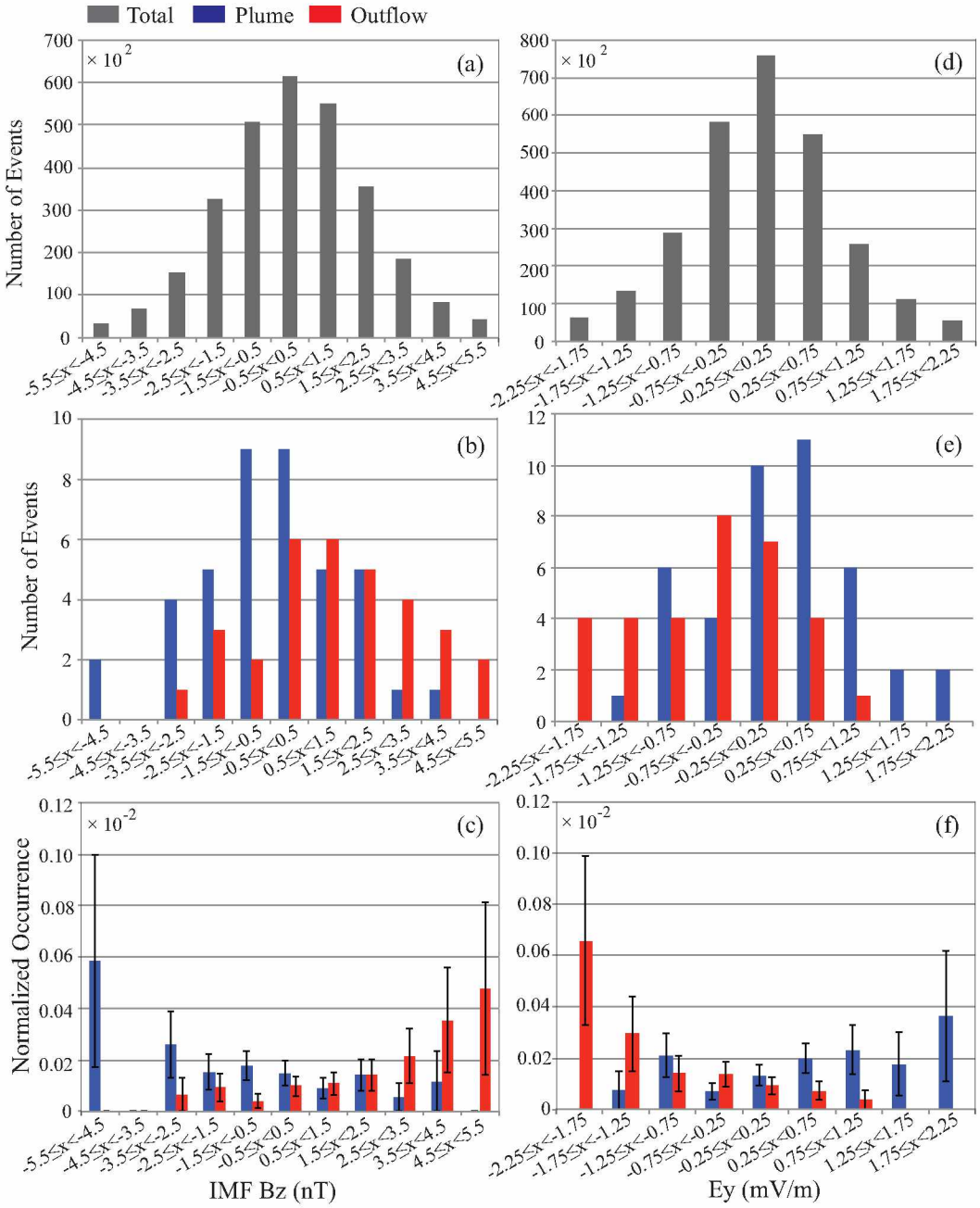

Figure 7.6. Distributions of (a) IMF B_z and (d) E_y data obtained from 2007 through 2009. Distributions of plumes (blue) and outflows (red) as a functions of (b) IMF B_z and (e) E_y. Normalized occurrence rates of plume (blue) and outflow (red) events as a function of (c) IMF B_z and (f) E_y [*Lee et al.*, 2015b].

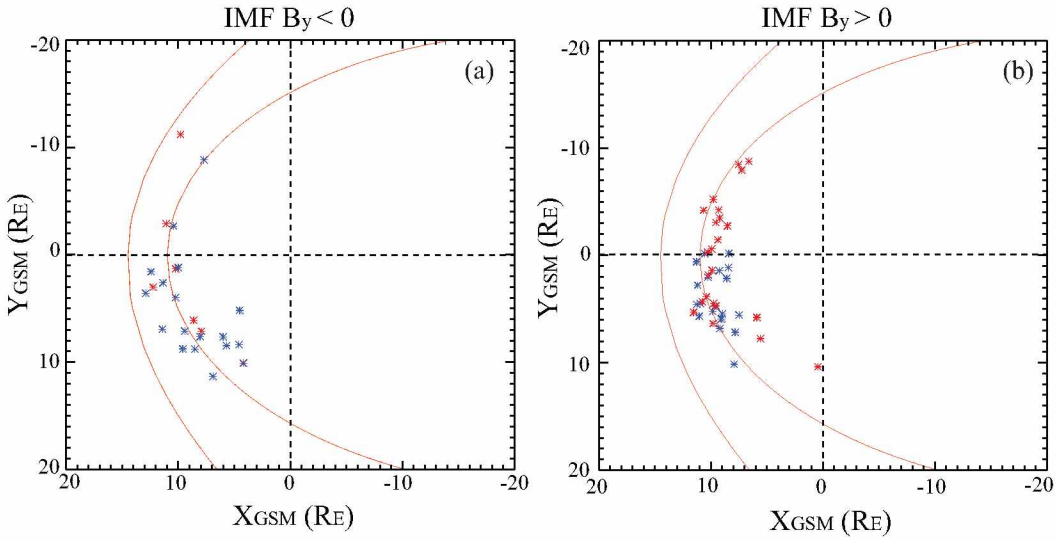

Figure 7.7. Distributions of plumes (blue) and the outflows (red) when the (a) IMF $B_y < 0$ and (b) IMF $B_y > 0$ in the X-Y GSM plane [*Lee et al.*, 2015b].

75%) than during negative IMF B_y (8 of 32, 25%). 75% (25%) of the outflows were observed at the duskside (dawnside) when the IMF B_y is negative, while 46% (54%) of the outflow events were observed at the duskside (dawnside) during positive IMF B_y. These results showed the IMF B_y effect on the occurrence rate of the outflows. This is consistent with the results from *Chen and Moore* [2006], who showed that the peak occurrence rate of the plumes shifts to the dawnside when IMF B_y is positive.

In contrast to the occurrence rate of the outflow events, more plume events were found at the duskside whether IMF $B_y > 0$ or IMF $B_y < 0$. The occurrence rate of plume at the duskside (39 of 43, 91%) is much higher than that at the dawnside (9%). This is consistent with the results from the previous statistical studies [*Walsh et al.*, 2013; *Darrouzet et al.*, 2008; *Chen and Moore*, 2006].

The distribution of the solar wind dynamic pressure from 2007 through 2009 obtained from OMNIweb is shown in Figure 7.8(a). The most common solar wind pressure is between 1 and 2 nPa. Figure 7.8(b) shows the distributions of the plumes (blue) and outflows (red) as a function of the solar wind dynamic pressure. A majority of the plume and outflow events occurs when the solar wind dynamic pressure is between 1 and 2 nPa. The normalized occurrence rates of both plume (blue) and outflow (red) events increase along with the dynamic pressure (Figure 7.8c). Strong magnetospheric compression causes the dayside magnetopause to move inward so that the plume associated with plasmaspheric erosion can appear near the magnetopause [*Elphic et al.*, 1996; *Kim et al.*, 2007]. Many observational studies have shown that strong ionospheric outward flux was correlated with solar wind dynamic pressure since it is one of the driving parameters [*Cully et al.*, 2003b; *Lennartsson et al.*, 2004; *Engwall et al.*, 2009].

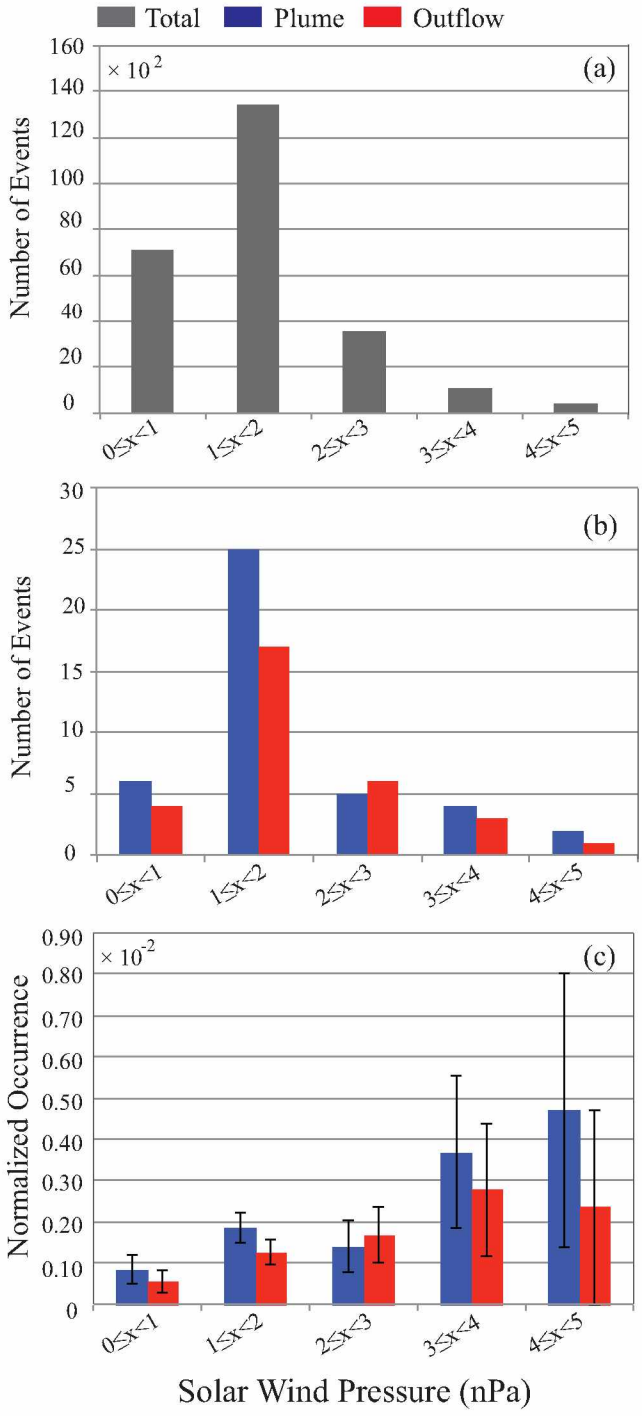

Figure 7.8. (a) Distribution of the solar wind pressure using three years of data from OMNIweb, (b) distributions of the plume (blue) and the outflow (red) events as a function of the solar wind dynamic pressure and (c) the normalized occurrence rates of the plume (blue) and the outflow (red) events as a function of the solar wind dynamic pressure [*Lee et al.*, 2015b].

7.4 Discussion

7.4.1 IMF B_z Effects on the Occurrence Rates of the Plasmaspheric Plume and Ionospheric Outflow

67% (29 of 43) of the plume events were observed during southward IMF, while only 33% were observed during northward IMF. Significantly more plume events were observed at the duskside (91%, 39 of 43) than those at the dawnside (See Figure 7.7).

The occurrence rate of the plasmaspheric plume is strongly correlated with high geomagnetic activity as well as intervals of southward IMF [*Carpenter et al.*, 1993; *Horwitz et al.*, 1990; *Moldwin et al.*, 2003; *Goldstein et al.*, 2003]. For southward IMF, dayside magnetopause reconnection occurs and primarily drives antisunward flow in the ionospheric polar cap, with a return sunward convection at lower latitudes [*Dungey*, 1961; *Heppner*, 1972]. This sunward convection in the inner magnetosphere causes the erosion of the outer portion of the rotating plasmasphere. The plasmaspheric drainage plume can be formed during intervals of enhanced magnetospheric convection. Many observations [*Chen and Moore*, 2006; *Chappell*, 1972; *Walsh et al.*, 2013; *Darrouzet et al.*, 2008; *Kim et al.*, 2007] have shown that plumes are more often found at the duskside than at the dawnside, which is consistent with the dawn-dusk asymmetry of the occurrence rate of the plume found in this chapter.

The higher occurrence rate of the ionospheric outflow was observed for the northward IMF (IMF $B_z > 0$, dawnward solar wind electric field) (Figure 7.6c). *Ridley et al.* [1998] have shown that the changes of the IMF orientation determine the shape of the residual potential pattern. For northward IMF, the ionospheric convection pattern is more complicated than that for southward IMF. For strongly northward IMF, the two-cell convection pattern forms in the high-latitude ionosphere with the counter-clockwise duskside cell and the clockwise dawnside cell. This pattern indicates the magnetic flux being convected from the tail to the dayside (sunward-flowing) in the high-latitude ionosphere [*Ridley et al.*, 1998; *Reiff and Burch*, 1985]. The ionospheric outflow can be convected toward dayside along with the magnetic flux. Thus, the occurrence rate of the ionospheric outflows observed at the dayside magnetopause gets high when the IMF is strongly northward.

7.4.2 IMF B_y Effects on the Occurrence Rate of the Ionospheric Outflow

54% (or 13 of 24) of the outflow events were observed at the dawnside when IMF B_y is positive, while only 25% (2 of 8) were observed during negative IMF B_y. Conversely, 75% of the outflow events were observed at the duskside during negative IMF B_y, while 46% were observed when IMF B_y is positive.

The effects of IMF B_y on the dawn-dusk asymmetry of the convection pattern, auroral oval

and electric field in the ionosphere have been studied [*Reiff and Burch*, 1985; *Cowley et al.*, 1991; *Lu et al.*, 1989; *Mozer and Lucht*, 1974; *Raitt et al.*, 1977; *Holzworth and Meng*, 1984]. The two convection cells in the high-latitude ionosphere are symmetric for strongly northward IMF with negligible B_y [*Reiff and Burch*, 1985; *Ridley et al.*, 1998]. In the presence of IMF B_y, these two convection cells become asymmetric. For positive (negative) IMF B_y, both convection cells are clockwise (counter-clockwise) and the dawnside (duskside) cell is larger than the duskside (dawnside) cell in the Northern Hemisphere [*Reiff and Burch*, 1985]. These convection patterns indicate that the plasma flows sunward at the dawnside (duskside) in the high-latitude ionosphere during strongly northward IMF with a positive (negative) B_y component.

The auroral oval is shifted toward dawn in the Northern Hemisphere for positive IMF B_y and toward dusk for negative IMF B_y [*Holzworth and Meng*, 1984]. The auroral zone is one of the source regions of the ionospheric outflow so that the shift toward dawnside for positive IMF B_y can lead to a higher occurrence rate of the ionospheric outflow at the dawnside.

The dawn-dusk asymmetry of the electric field in the ionosphere was related to the sign and magnitude of IMF B_y. The electric field near local dawn in the Northern Hemisphere was enhanced when the IMF $B_y > 0$, whereas the electric field near local dusk increased in the Northern Hemisphere when the IMF $B_y < 0$ [*Mozer and Lucht*, 1974]. This convection electric field can significantly increase the proton temperature and cause a high outward flux of proton for average ionospheric conditions at high altitudes [*Raitt et al.*, 1977].

The dawn-dusk asymmetries in the Southern Hemisphere is in the opposite sense to the asymmetries in the Northern Hemisphere [*Cowley et al.*, 1991; *Mozer and Lucht*, 1974; *Raitt et al.*, 1977]. However, the observational dawn-dusk asymmetries in the Southern Hemisphere were found to be less strong [*Lu et al.*, 1989]. This is consistent with our results that the enhanced occurrence rate of the ionospheric outflows were observed at the dawnside when IMF $B_y > 0$.

7.5 Summary and Conclusions

We presented a statistical study of the plasmaspheric plumes and the ionospheric outflows observed by C3 near the dayside magnetopause from 2007 to 2009. We identified 43 plume events with perpendicular pitch angle distributions and 32 outflow events with unidirectional or bidirectional field-aligned pitch angle distributions during 442 dayside magnetopause crossings. The characteristics between the plumes and outflows were compared, and we also investigated the relations between the occurrence rates of the plume and outflow events and their locations, their dependences on the geomagnetic activity and the solar wind/IMF conditions. The main results of this chapter can be summarized as follows:

1. The occurrence rate of the plumes is significantly higher at the duskside than that at the

dawnside. However, the occurrence rate of the outflow shows a weak dawn-dusk asymmetry.

2. The median values of the electron (ion) density of plume and outflow events are 5.4 cm^{-3} and 5.2 cm^{-3} (0.9 cm^{-3} and 0.7 cm^{-3}), respectively.

3. Plume events prefer to occur during moderate conditions ($K_p = 3$ and $-30 \leq D_{st} < -10$ nT). The ionospheric outflows do not occur when $K_p = 0$ and the occurrence rate of the ionospheric outflows does not have clear D_{st} dependence.

4. The plume events tend to occur during southward IMF (duskward solar wind electric field), whereas the outflow events prefer to occur during northward IMF (dawnward solar wind electric field).

5. 75% (25%) of the outflows were observed at the duskside (dawnside) when the IMF B_y is negative, while 46% (54%) of the outflow events were observed at the duskside (dawnside) during positive IMF B_y.

6. The occurrence rates of both plumes and outflows increase as the solar wind dynamic pressure increases.

Chapter 8
Conclusions and Future Work

8.1 Conclusions

Magnetic reconnection is a fundamental process that operates within the heliosphere and throughout the universe. The reconnection process at the dayside magnetopause plays an essential role for the transfer of mass, momentum and energy from the solar wind to the Earth's magnetosphere. Magnetic reconnection at the dayside magnetopause is usually asymmetric since the properties of the plasma and magnetic field are quite different in the magnetosphere and the magnetosheath. The plasma density on the magnetosheath side is much higher than that on the magnetospheric side and the magnetic field strength on the magnetosheath side is usually smaller than that on the magnetospheric side. Cold dense plasmas, originating either directly from the ionosphere or from the plasmasphere, has often been observed near the dayside magnetopause. These cold plasmas may affect reconnection since they modify the plasma properties on the magnetospheric side significantly. We investigate characteristics of cold dense ions observed near the dayside magnetopause and the role they play in reconnection dynamics at the dayside magnetopause based on case and statistical studies using the Cluster spacecraft datasets. We also examine a controlling factor that leads to the asymmetric reconnection geometry at the magnetopause.

The main results of this dissertation can be summarized as follows:

Characteristics of the Cold Dense Ions Observed near the Dayside Magnetopause

Case and statistical studies have been done to investigate characteristics of the cold dense ions observed near the magnetopause using the datasets from the Cluster spacecraft. The event presented in Chapter 5 is a plasmaspheric plume case and the event presented in Chapter 6 is an ionospheric outflow case. For the plume case, cold ions (5–30 eV) with 90° pitch angle distributions were observed outside the reconnection region. Once the cold ions were energized, three cold ion populations (probably H^+, He^+ and O^+) appeared in the energy spectrum since they have different masses and were accelerated to the same velocity. Helium (He^+) and oxygen (O^+) ions were energized 4 and 16 times higher than that of the proton (H^+). For the ionospheric outflow case, cold ions (< 200 eV) which have 0°–75° pitch angle distributions were observed by both C1 and C3 while passing the magnetopause on 8 April 2008. The observation of the unidirectional cold ions indicates that these cold ions can be directly coming from the ionosphere in the Southern Hemisphere and reached the dayside magnetopause. The low-energy (up to 1.5 keV) electrons with bidirectional pitch angle distributions were detected, confirming that the magnetic field lines are closed. The asymmetric ionospheric outflows at the dayside magnetopause can be caused by the seasonal magnetic field geometry effect. During this event, the Southern Hemisphere was in winter

and the Northern Hemisphere was in summer. The winter hemisphere has a lower conductivity that drives an enhancement in the perpendicular electric field. The stronger electric field increases the ion temperature which may causes asymmetric ionospheric outflows coming from only the Southern Hemisphere. The DMSP observations may provide some clues on the cause of the asymmetric ionospheric outflow. The DMSP observations show that the ion temperature in the Southern Hemisphere is much higher than that in the Northern Hemisphere. The ionospheric outflows consist of two different species (possibly H^+ and He^+) since there are two ion flux peaks in the ion energy spectra. The energy of the second peak (He^+) is about 4 times the first one (H^+). The observed cold ion fluxes are modulated by the ULF wave at the period of 60–120 s.

From the statistical study, dayside magnetopause crossings from 2007 to 2009 were inspected. The plasmaspheric plumes and ionospheric outflows were identified based on the following criteria. The low-energy ion particle energy flux was greater than 10^5 keV/(cm^{2}s sr keV) and the energy of the cold ions must be larger than the threshold (5 eV) of the HIA/CIS instrument to be detected. The plasmaspheric plumes are characterized by 90° pitch angle distributions, whereas the ionospheric outflows feature unidirectional or bidirectional field-aligned pitch angle distributions. There are energy-dispersion signatures in the ionospheric outflow events. We investigated the occurrence rates of the plumes and ionospheric outflows and how the plume and outflow occurrence rates depend on geomagnetic activity and the solar wind/IMF conditions. 43 (10%) plasmaspheric plume events and 32 (7%) ionospheric outflow events were detected while C3 crossed dayside magnetopause 442 times from 2007 to 2009. It is found that the occurrence rate of the plume at the duskside is significantly higher than that at the dawnside, whereas the occurrence rate of the outflow shows a weak dawn-dusk asymmetry. This indicates that the plasmaspheric plumes may lead to a dawn-dusk asymmetry of dayside reconnection. The plume events prefer to occur during moderate geomagnetic activity ($K_p = 3$, $-20 \leq D_{st} < -10$ nT), whereas the ionospheric outflow events do not occur when $K_p = 0$ and their occurrence rate does not have a clear D_{st} dependence. The plasmaspheric plumes tend to occur during southward IMF (duskward solar wind electric field), whereas the ionospheric outflows prefer to occur during northward IMF (dawnward solar wind electric field). For southward IMF, dayside magnetopause reconnection occurs and drives sunward convection at low latitudes which causes the erosion of the outer portion of the rotating plasmasphere. Thus, the plasmaspheric plume can be formed during intervals of enhanced magnetospheric convection. For northward IMF, the two-cell convection pattern leads the larger amount of magnetic flux being convected from the tail to the dayside. The occurrence rate of ionospheric outflows depends on the effect of IMF B_y. 54% (46%) of the outflow events were observed at the dawnside (duskside) during positive IMF B_y, whereas 25% (75%) of the outflows were observed at the dawnside (duskside) during negative IMF B_y. The dayside reconnection in the presence of the

positive IMF B_y (negative IMF B_y) results in the dawnward (duskward) exerted forces that may affect the high occurrence rate of the ionospheric outflow at the dawnside (duskside). The auroral oval, which is one of the source regions of the ionospheric outflow, is shifted toward dawn (dusk) for positive (negative) IMF B_y. Finally, the occurrence rates of both plumes and outflows increase as the solar wind dynamic pressure increases. Strong magnetospheric compression causes the dayside magnetopause to move inward so that the plume can appear near the magnetopause. The solar wind dynamic pressure is one of the driving parameters of the outward flux from the ionosphere.

Behavior of the Cold Dense Ions during Magnetic Reconnection

In Chapter 5, we investigated the behavior of the cold dense plasma during magnetic reconnection and the role of the cold plasma in the reconnection process. We found that the motion of cold plasmaspheric ions entering the reconnection region differs from that of warmer magnetosheath and magnetospheric ions. In contrast to the warmer ions, which are probably accelerated by reconnection near the subsolar magnetopause, the colder ions are simply entrained by $\mathbf{E}\times\mathbf{B}$ drift at high latitudes on the recently reconnected magnetic field lines. This indicates that plasmaspheric ions can sometimes play only a very limited role in asymmetric reconnection.

Asymmetric Reconnection Geometry

We investigated the controlling factor that leads to the asymmetric reconnection geometry. We identified the separatrices and the flow boundaries on the magnetosheath and magnetospheric sides of the magnetopause by sharp changes in the electromagnetic wave spectrogram, particle differential flux, plasma flow, magnetic field, and density gradients. We estimated the separatrix angle (θ_s) by taking the ratio of the local magnetic fields at the separatrix, $\theta_s \approx tan^{-1}(B_N/B_L)$, in the boundary normal coordinate system. It is found that the separatrix and flow boundary angles on the magnetosheath side are larger than those on the magnetospheric side. Acceleration of a higher-density plasma requires a larger $\mathbf{J}\times\mathbf{B}$ force density, which is proportional to the square root of density, magnetic field and tangent of the separatrix angle, $\mathbf{J}\times\mathbf{B} \propto \sqrt{n}\mathbf{B}$ and $\mathbf{J}\times\mathbf{B} \propto tan(\theta_s)$. The stronger plasma density asymmetry (~13) of the magnetosheath to the magnetospheric side than magnetic field asymmetry (~1.2) of the magnetospheric to the magnetosheath side at this boundary causes the separatrix angle on the magnetosheath side to be larger than that on the magnetospheric side and thus leads the asymmetric reconnection geometry.

In summary, this dissertation presents case and statistical studies on the characteristics of the cold ions observed at the dayside magnetopause by using the Cluster spacecraft datasets. The plasmaspheric plumes have been distinguished from the ionospheric outflows using ion pitch angle distributions. The ionospheric outflows are featured by unidirectional or bidirectional field-aligned

pitch angle distributions, whereas the plasmaspheric plumes are characterized with 90° pitch angle distributions. The occurrence rates of the plasmaspheric plumes and ionospheric outflows and their dependence on the solar wind/IMF conditions have been investigated. It is found that the occurrence rate of plasmaspheric plume or ionospheric plasma strongly depends on the solar wind/IMF conditions. In particular, plasmaspheric plumes tend to occur during southward IMF while ionospheric outflows tends to occur during northward IMF. The occurrence rate of the plasmaspheric plumes is significantly higher on the duskside than that on the dawnside, indicating that the plasmaspheric plumes may lead to a dawn-dusk asymmetry of the dayside reconnection.

Furthermore, this dissertation investigates the behavior of the cold dense plasma of ionospheric origin during magnetic reconnection at the dayside magnetopause. The motion of cold plasmaspheric ions entering the reconnection region differs from that of warmer magnetosheath and magnetospheric ions. In contrast to the warmer ions, which are probably accelerated by reconnection near the subsolar magnetopause, the colder ions are simply entrained by $\mathbf{E}\times\mathbf{B}$ drifts at high latitudes on the recently reconnected magnetic field lines. This indicates that plasmaspheric ions can sometimes play a very limited role in magnetic reconnection process.

Finally, this dissertation examines a controlling factor that leads to the asymmetric reconnection geometry at the magnetopause. It is demonstrated that the separatrix and flow boundary angles are greater on the magnetosheath than on the magnetospheric side of the magnetopause, probably due to the stronger density asymmetry rather than magnetic field asymmetry at this boundary.

8.2 Future Work

In Chapter 5, we showed that the energetic ions ($>$ 10 keV) that observed in the boundary layer participate the reconnection process and then were accelerated together with other populations in the outflow region. Are these particles coming from the reconnection process or somewhere else? If the energetic ions are accelerated by the reconnection, how are they accelerated (the acceleration mechanisms)? Magnetic reconnection is the dominant mechanism for converting magnetic energy into high-velocity flows and energetic particles (kinetic energy), the acceleration mechanism for these remains an outstanding question. It would be helpful to further study on the acceleration mechanisms for understanding the behavior of energetic particles in the boundary layer.

In Chapter 6 and Chapter 7, we showed that different characteristics of between the plasmaspheric plume and the ionospheric outflow observed near the dayside magnetopause from the Cluster spacecraft (C3). It would be important to understand and quantify the effects of the low-energy and dense plasma on the dynamics of the Earth's magnetopause such as magnetic reconnection. Numerical and analytic studies also predicted the dense and/or heavy plasma reduces the dayside reconnection rate as the mass loading the reconnection site [*Cassak and Shay*, 2007; *Borovsky et al.*,

2013]. *Walsh et al.* [2014] showed that the plasmaspheric plume reduces the the reconnection jet outflow velocities which scales with the hybrid Alfvén speed,

$$V_A = \sqrt{\frac{B_{sh}B_{sp}(B_{sh} + B_{sp})}{\mu_0(\rho_{sh}B_{sp} + \rho_{sp}B_{sh})}} \tag{8.1}$$

where the subscript sh (sp) denotes the magnetosheath (magnetospheric) side of the magnetopause, by comparing the simultaneous observations by THEMIS-A and THEMIS-D at the dayside magnetopause. However, the lower bulk flow (reconnection outflow speed), which comes from an inadvertent moment calculation, does not represent the velocity of either populations when two distinct populations, cold plume and hotter magnetosheath populations, coexist in phase space. Therefore, we can further investigate the reconnection rate using the outflow jet velocity in the HT frame by performing a Kappa distribution fit as separating the different behaviors of the cold dense plasma and hotter magnetosheath plasma.

Developing an in-depth understanding of the effect of the cold dense plasmaspheric plume and/or ionospheric outflow on the reconnection and identifying the acceleration mechanisms require a synthesized approach using in situ observations and numerical simulations, together with analytic efforts in order to answer the following outstanding questions:

(1) How are the energetic particles getting accelerated during magnetic reconnection?

(2) How do the cold dense plasmas (the plasmaspheric plumes and ionospheric outflows) participate in the reconnection?

(3) How do the plasmaspheric plumes and ionospheric outflows alter merging rates at the dayside magnetopause as a function of the imposed external (solar wind/IMF) and local (reconnection current sheet layer) conditions?

First, ample dayside reconnection events in the presence of the cold plasma and/or energetic particles need to be identified. Cluster/THEMIS datasets and the most advanced datasets from the Magnetospheric MultiScale (MMS) mission can be used. Second, the characteristics of the low-energy dense plasma and the energetic particles need to be determined and then the different predictions from previously proposed theories and simulation results need to be tested by comparing with the observations in order to estimate the effects of the cold dense plumes and outflows on the reconnection process.

References

Andersson, L., W. K. Peterson, and K. M. McBryde (2005), Estimates of the suprathermal O^+ outflow characteristic energy and relative location in the auroral oval, *Geophys. Res. Lett.*, *32*, L09104, doi:10.1029/2004GL021434.

André, M., and C. M. Cully (2012), Low-energy ions: A previously hidden solar system particle population, *Geophys. Res. Lett.*, *39*, L03101, doi:10.1029/2011GL050242.

André, M., A. Vaivads, Y. V. Khotyaintsev, T. Laitinen, H. Nilsson, G. Stenberg, A. Fazakerley, and J. G. Trotignon (2010), Magnetic reconnection and cold plasma at the magnetopause, *Geophys. Res. Lett.*, *37*, L22108, doi:10.1029/2010GL044611.

Balogh, A., et al. (1997), The Cluster Magnetic Field Investigation, *Space Sci. Rev.*, *79*, 65–91.

Balogh, A., et al. (2001), The Cluster Magnetic Field Investigation: overview of in-flight performance and initial results, *Ann. Geophys.*, *19*, 1207–1217, doi:10.5194/angeo-19-1207-2001.

Baugher, C. R., C. R. Chappell, J. L. Horwitz, E. G. Shelley, and D. T. Young (1980), Initial thermal plasma observations from ISEE-1, *Geophys. Res. Lett.*, *7*, 657–660, doi:10.1029/GL007i009p00657.

Baumjohann, W., and R. A. Treumann (1996), *Basic space plasma physics*.

Biermann, L. (1951), Kometenschweife und solare Korpuskularstrahlung, *Zeit. Astrophys*, *29*, 274.

Birn, J., J. E. Borovsky, and M. Hesse (2008), Properties of asymmetric magnetic reconnection, *Phys. Plasmas*, *15*(3), 032,101, doi:10.1063/1.2888491.

Borg, A. L., et al. (2005), Cluster encounter of a magnetic reconnection diffusion region in the near-Earth magnetotail on September 19, 2003, *Geophys. Res. Lett.*, *32*, L19105, doi:10.1029/2005GL023794.

Borovsky, J. E., and M. H. Denton (2006), Effect of plasmaspheric drainage plumes on solar-wind/magnetosphere coupling, *Geophys. Res. Lett.*, *33*, L20101, doi:10.1029/2006GL026519.

Borovsky, J. E., and M. Hesse (2007), The reconnection of magnetic fields between plasmas with different densities: Scaling relations, *Phys. Plasmas*, *14*(10), 102,309, doi:10.1063/1.2772619.

Borovsky, J. E., and J. T. Steinberg (2006), The "calm before the storm" in CIR/magnetosphere interactions: Occurrence statistics, solar wind statistics, and magnetospheric preconditioning, *Journal of Geophysical Research (Space Physics)*, *111*, A07S10, doi:10.1029/2005JA011397.

Borovsky, J. E., M. Hesse, J. Birn, and M. M. Kuznetsova (2008), What determines the reconnection rate at the dayside magnetosphere?, *J. Geophys. Res.*, *113*, A07210, doi:10.1029/2007JA012645.

Borovsky, J. E., M. H. Denton, R. E. Denton, V. K. Jordanova, and J. Krall (2013), Estimating the effects of ionospheric plasma on solar wind/magnetosphere coupling via mass loading of dayside reconnection: Ion-plasma-sheet oxygen, plasmaspheric drainage plumes, and the plasma cloak, *J. Geophys. Res.*, *118*, 5695–5719, doi:10.1002/jgra.50527.

Cairns, R. A. (1999), Space Physics. An Introduction to Plasmas and Particles in the Heliosphere and Magnetospheres, by May-Britt Kallenrode. Springer-Verlag, Berlin-Heidelberg-New York-London-Paris-Tokyo-Hong Kong, 1998, 375 pages. ISNB 3 540 64126 2. *Â£45.50.*, *J. Plasma Phys.*, *61*, 365–365, doi:10.1017/S0022377899009976.

Carpenter, D. L., A. J. Smith, B. L. Giles, C. R. Chappell, and P. M. E. Décréau (1992), A case study of plasma structure in the dusk sector associated with enhanced magnetospheric convection, *J. Geophys. Res.*, *97*, 1157–1166, doi:10.1029/91JA01546.

Carpenter, D. L., B. L. Giles, C. R. Chappell, P. M. E. Décréau, R. R. Anderson, A. M. Persoon, A. J. Smith, Y. Corcuff, and P. Canu (1993), Plasmasphere dynamics in the duskside bulge region: A new look at old topic, *J. Geophys. Res.*, *98*, 19,243, doi:10.1029/93JA00922.

Cassak, P. A., and M. A. Shay (2007), Scaling of asymmetric magnetic reconnection: General theory and collisional simulations, *Phys. Plasmas*, *14*(10), 102,114, doi:10.1063/1.2795630.

Cassak, P. A., and M. A. Shay (2008), Scaling of asymmetric Hall magnetic reconnection, *Geophys. Res. Lett.*, *35*, L19102, doi:10.1029/2008GL035268.

Cassak, P. A., and M. A. Shay (2009), Structure of the dissipation region in fluid simulations of asymmetric magnetic reconnection, *Phys. Plasmas*, *16*(5), 055,704, doi:10.1063/1.3086867.

Cattell, C., et al. (2005), Cluster observations of electron holes in association with magnetotail reconnection and comparison to simulations, *J. Geophys. Res.*, *110*, A01,211, doi:10.1029/2004JA010,519.

Chapman, S., and V. C. A. Ferraro (1931), A new theory of magnetic storms, part 1, the initial phase, *Terr. Magn. Atmos. Elect.*, *36*, 77–97,171–186.

Chappell, C. R. (1972), Recent satellite measurements of the morphology and dynamics of the plasmasphere., *Reviews of Geophysics and Space Physics*, *10*, 951–979, doi:10.1029/RG010i004p00951.

Chappell, C. R. (1974), Detached plasma regions in the magnetosphere., *J. Geophys. Res.*, *79*, 1861–1870, doi:10.1029/JA079i013p01861.

Chappell, C. R., K. K. Harris, and G. W. Sharp (1970), The morphology of the bulge region of the plasmasphere., *J. Geophys. Res.*, *75*, 3848–3861, doi:10.1029/JA075i019p03848.

Chappell, C. R., K. K. Harris, and G. W. Sharp (1971), The dayside of the plasmasphere, *J. Geophys. Res.*, *76*, 7632, doi:10.1029/JA076i031p07632.

Chappell, C. R., T. E. Moore, and J. H. Waite, Jr. (1987), The ionosphere as a fully adequate source of plasma for the Earth's magnetosphere, *J. Geophys. Res.*, *92*, 5896–5910.

Chappell, C. R., M. M. Huddleston, T. E. Moore, B. L. Giles, and D. C. Delcourt (2008), Observations of the warm plasma cloak and an explanation of its formation in the magnetosphere, *J. Geophys. Res.*, *113*, A09206, doi:10.1029/2007JA012945.

Chen, A. J., and R. A. Wolf (1972), Effects on the plasmasphere of a time-varying convection electric field, *Planet. Space Sci.*, *20*, 483–509, doi:10.1016/0032-0633(72)90080-3.

Chen, S.-H., and T. E. Moore (2006), Magnetospheric convection and thermal ions in the dayside outer magnetosphere, *J. Geophys. Res.*, *111*, A03215, doi:10.1029/2005JA011084.

Comisso, L., and F. A. Asenjo (2014), Thermal-Inertial Effects on Magnetic Reconnection in Relativistic Pair Plasmas, *Phys. Rev. Lett.*, *113*(4), 045001, doi:10.1103/PhysRevLett.113.045001.

Cornilleau-Wehrlin, N., et al. (1997), The Cluster Spatio-Temporal Analysis of Field Fluctuations (STAFF) Experiment, *Space Sci. Rev.*, *79*, 107–136, doi:10.1023/A:1004979209565.

Cowley, S. W. H. (1982), The causes of convection in the Earth's magnetosphere: A review of developments during the IMS, *Rev. Geophys.*, *20*, 531–565.

Cowley, S. W. H., J. P. Morelli, and M. Lockwood (1991), Dependence of convective flows and particle precipitation in the high-latitude dayside ionosphere on the X and Y components of the interplanetary magnetic field, *J. Geophys. Res.*, *96*, 5557–5564, doi:10.1029/90JA02063.

Cully, C. M., E. F. Donovan, A. W. Yau, and H. J. Opgenoorth (2003a), Supply of thermal ionospheric ions to the central plasma sheet, *J. Geophys. Res.*, *108*, 1092, doi:10.1029/2002JA009457.

Cully, C. M., E. F. Donovan, A. W. Yau, and G. G. Arkos (2003b), Akebono/Suprathermal Mass Spectrometer observations of low-energy ion outflow: Dependence on magnetic activity and solar wind conditions, *J. Geophys. Res.*, *108*, 1093, doi:10.1029/2001JA009200.

Dandouras, I. (2013), Detection of a plasmaspheric wind in the Earth's magnetosphere by the Cluster spacecraft, *Ann. Geophys.*, *31*, 1143–1153, doi:10.5194/angeo-31-1143-2013.

Darrouzet, F., J. de Keyser, P. M. E. Décréau, F. El Lemdani-Mazouz, and X. Vallières (2008), Statistical analysis of plasmaspheric plumes with Cluster/WHISPER observations, *Ann. Geophys.*, *26*, 2403–2417, doi:10.5194/angeo-26-2403-2008.

Davis, T. N., and M. Sugiura (1966), Auroral electrojet activity index AE and its universal time variations, *J. Geophys. Res.*, *71*, 785–801, doi:10.1029/JZ071i003p00785.

de Hoffman, F., and E. Teller (1950), Magneto-hydrodynamic shocks, *Phys. Rev.*, *80*, 692.

Décréau, P. M. E., et al. (2001), Early results from the Whisper instrument on Cluster: an overview, *Ann. Geophys.*, *19*, 1241–1258, doi:10.5194/angeo-19-1241-2001.

Delcourt, D. C., C. R. Chappell, T. E. Moore, and J. H. Waite, Jr. (1989), A three-dimensional numerical model of ionospheric plasma in the magnetosphere, *J. Geophys. Res.*, *94*, 11,893–11,920, doi:10.1029/JA094iA09p11893.

Drake, J. F. (1995), Magnetic Reconnection: A Kinetic Treatment, in *Physics of the Magnetopause, Geophys. Monogr. Ser.,* vol. 90, edited by P. Song, B. U. Ö. Sonnerup, and M. F. Thomsen, pp. 155–165, AGU, Washington, D. C.

Drake, J. F., M. Swisdak, T. D. Phan, P. A. Cassak, M. A. Shay, S. T. Lepri, R. P. Lin, E. Quataert, and T. H. Zurbuchen (2009), Ion heating resulting from pickup in magnetic reconnection exhausts, *Journal of Geophysical Research (Space Physics)*, *114*, A05111, doi:10.1029/2008JA013701.

Dungey, J. W. (1961), Interplanetary magnetic field and the auroral zones, *Phys. Rev. Letters*, *6*, 47–48.

Elphic, R. C. (1990), Observations of flux transfer events: Are FTEs flux ropes, islands, or surface waves?, *Washington DC American Geophysical Union Geophysical Monograph Series*, *58*, 455–471, doi:10.1029/GM058p0455.

Elphic, R. C., and C. T. Russell (1979), ISEE-1 and 2 magnetometer observations of the magnetopause, in *Magnetospheric Boundary Layers*, *ESA Special Publication*, vol. 148, edited by B. Battrick, J. Mort, G. Haerendel, and J. Ortner, pp. 43–50.

Elphic, R. C., L. A. Weiss, M. F. Thomsen, D. J. McComas, and M. B. Moldwin (1996), Evolution of plasmaspheric ions at geosynchronous orbit during times of high geomagnetic activity, *Geophys. Res. Lett.*, *23*, 2189–2192, doi:10.1029/96GL02085.

Engwall, E., A. I. Eriksson, C. M. Cully, M. André, P. A. Puhl-Quinn, H. Vaith, and R. Torbert (2009), Survey of cold ionospheric outflows in the magnetotail, *Ann. Geophys.*, *27*, 3185–3201, doi:10.5194/angeo-27-3185-2009.

Escoubet, C. P., C. T. Russell, and R. Schmidt (1997), The Cluster and Phoenix Missions, in *reprinted from Space Science Reviews*, vol. 79, pp. Nos1–2, Kluwer Academic.

Escoubet, C. P., M. Fehringer, and M. Goldstein (2001), IntroductionThe Cluster mission, *Ann. Geophys.*, *19*, 1197–1200, doi:10.5194/angeo-19-1197-2001.

Fairfield, D. H. (1971), Average and unusual locations of the Earth's magnetopause and bow shock, *J. Geophys. Res.*, *76*, 6700–6716.

Farris, M. H., and C. T. Russell (1994), Determining the standoff distance of the bow shock: Mach number dependence and use of models, *J. Geophys. Res.*, *99*, 17,681, doi:10.1029/94JA01020.

Fazakerley, A. N., A. D. Lahiff, R. J. Wilson, I. Rozum, C. Anekallu, M. West, and H. Bacai (2010), *PEACE Data in the Cluster Active Archive*, pp. 129–144, doi:10.1007/978-90-481-3499-1_8.

Fennell, J. F., D. R. Croley, Jr., and S. M. Kaye (1981), Low-energy ion pitch angle distributions in the outer magnetosphere - Ion zipper distributions, *J. Geophys. Res.*, *86*, 3375–3382, doi: 10.1029/JA086iA05p03375.

Ferraro, V. C. A. (1952), O the Theory of the First Phase of a Geomagnetic Storm: a New Illustrative Calculation Based on AN Idealised (plane not Cylindrical) Model Field Distribution, *J. Geophys. Res.*, *57*, 15–+.

Frey, H. U., T. D. Phan, S. A. Fuselier, and S. B. Mende (2003), Continuous magnetic reconnection at Earth's magnetopause, *Nature*, *426*, 533–537, doi:10.1038/nature02084.

Fuselier, S. A., D. M. Klumper, W. K. Peterson, and E. G. Shelley (1989), Direct injection of ionospheric O^+ into the dayside low latitude boundary layer, *Geophys. Res. Lett.*, *16*, 1121–1124.

Fuselier, S. A., D. M. Klumper, and E. G. Shelley (1991), Ion reflection and transmission during reconnection at the earth's subsolar magnetpause, *Geophys. Res. Lett.*, *16*, 139–142.

Giles, B. L., C. R. Chappell, T. E. Moore, R. H. Comfort, and J. H. Waite, Jr. (1994), Statistical survey of pitch angle distributions in core (0-50 eV) ions from Dynamics Explorer 1: Outflow in the auroral zone, polar cap, and cusp, *J. Geophys. Res.*, *99*, 17,483, doi:10.1029/94JA00864.

Goldstein, J., B. R. Sandel, M. R. Hairston, and P. H. Reiff (2003), Control of plasmaspheric dynamics by both convection and sub-auroral polarization stream, *Geophys. Res. Lett.*, *30*, 2243, doi:10.1029/2003GL018390.

Goldstein, J., B. R. Sandel, M. F. Thomsen, M. Spasojević, and P. H. Reiff (2004), Simultaneous remote sensing and in situ observations of plasmaspheric drainage plumes, *J. Geophys. Res.*, *109*, A03,202, doi:10.1029/2003JA010281.

Goldstein, J., B. R. Sandel, W. T. Forrester, M. F. Thomsen, and M. R. Hairston (2005), Global plasmasphere evolution 22-23 April 2001, *J. Geophys. Res.*, *110*, A12218, doi: 10.1029/2005JA011282.

Gombosi, T. I. (Ed.) (1998), *Physics of the space environment.*

Gosling, J. T., M. F. Thomsen, S. J. Bame, T. G. Onsager, and C. T. Russell (1990a), The electron edge of the low latitude boundary layer during accelerated flow events, *Geophys. Res. Lett.*, *17*, 1833–1836.

Gosling, J. T., M. F. Thomsen, S. J. Bame, R. C. Elphic, and C. T. Russell (1990b), Cold ion beams in the low latitude boundary layer during accelerated flow events, *Geophys. Res. Lett.*, *17*, 2245–2248, doi:10.1029/GL017i012p02245.

Gosling, J. T., et al. (2007), Five spacecraft observations of oppositely directed exhaust jets from a magnetic reconnection X-line extending ¿ 4.26×10^6 km in the solar wind at 1 AU, *Geophys. Res. Lett.*, *34*, L20108, doi:10.1029/2007GL031492.

Grebowsky, J. M. (1970), Model study of plasmapause motion, *J. Geophys. Res.*, *75*, 4329–4333, doi:10.1029/JA075i022p04329.

Green, J. L., B. R. Sandel, S. F. Fung, D. L. Gallagher, and B. W. Reinisch (2002), On the origin of kilometric continuum, *J. Geophys. Res.*, *107*, 1105, doi:10.1029/2001JA000193.

Greenspan, M. E., C.-I. Meng, and D. H. Fairfield (1986), Simultaneous polar cap and magnetotail observations of intense polar rain, *J. Geophys. Res.*, *91*, 11,123–11,132, doi: 10.1029/JA091iA10p11123.

Gurnett, D. A., and A. Bhattacharjee (2005), *Introduction to Plasma Physics.*

Gustafsson, G., et al. (1997), The Electric Field and Wave Experiment for the Cluster Mission, *Space Sci. Rev.*, *79*, 137–156.

Gustafsson, G., et al. (2001), First results of electric field and density observations by CLUSTER EFW based on initial months of operation, *Ann. Geophys.*, *19*, 1219–1240.

Haerendel, G., G. Paschmann, N. Sckopke, H. Rosenbauer, and P. C. Hedgecock (1978), The frontside boundary layer of the magnetopause and the problem of reconnection, *J. Geophys. Res.*, *83*, 3195–3216.

Hairston, M. R., and R. A. Heelis (1993), High-latitude electric field studies using DMSP data, *Tech. rep.*

Heelis, R. A., and M. R. Hairston (1990), Studies of ionospheric dynamics utilizing data from DMSP, *Tech. rep.*

Heikkila, W. J., and J. D. Winningham (1971), Penetration of magnetosheath plasma to low altitudes through the dayside magnetospheric cusps, *J. Geophys. Res.*, *76*, 883–.

Heppner, J. P. (1972), Polar-cap electric field distributions related to the interplanetary magnetic field direction, *J. Geophys. Res.*, *77*, 4877–4887, doi:10.1029/JA077i025p04877.

Holzworth, R. H., and C.-I. Meng (1984), Auroral boundary variations and the interplanetary magnetic field, *Planet. Space Sci.*, *32*, 25–29, doi:10.1016/0032-0633(84)90038-2.

Horwitz, J. L., C. R. Baugher, C. R. Chappell, E. G. Shelley, and D. T. Young (1982), Conical pitch angle distributions of very low-energy ion fluxes observed by ISEE 1, *J. Geophys. Res.*, *87*, 2311–2320, doi:10.1029/JA087iA04p02311.

Horwitz, J. L., R. H. Comfort, and C. R. Chappell (1990), A statistical characterization of plasmasphere density structure and boundary locations, *J. Geophys. Res.*, *95*, 7937–7947, doi:10.1029/JA095iA06p07937.

Johnstone, A. D., et al. (1997), Peace: A plasma electron and current experiment, *Space Sci. Rev.*, *79*, 351–398.

Kallenrode, M.-B. (2004), *Space physics : an introduction to plasmas and particles in the heliosphere and magnetospheres.*

Kamide, Y., et al. (1998), Current understanding of magnetic storms: Storm-sunstorm relationships, *J. Geophys. Res.*, *103*, 17,705–17,728.

Karlsson, T. (2001), On electric field patterns associated with night-side discrete auroral arcs : A generalization of an auroral arc classification scheme, *Tech. Rep. 2001:01*, KTH, Alfvén Laboratory, qC 20100624.

Kavanagh, L. D., Jr., J. W. Freeman, Jr., and A. J. Chen (1968), Plasma flow in the magnetosphere, *J. Geophys. Res.*, *73*, 5511–5519, doi:10.1029/JA073i017p05511.

Kaye, S. M., E. G. Shelley, R. D. Sharp, and R. G. Johnson (1981), Ion composition of zipper events, *J. Geophys. Res.*, *86*, 3383–3388, doi:10.1029/JA086iA05p03383.

Khrabrov, A. V., and B. U. Ö. Sonnerup (1998), DeHoffmann-Teller Analysis, *ISSI Scientific Reports Series*, *1*, 221–248.

Kim, K.-H., J. Goldstein, and D. Berube (2007), Plasmaspheric drainage plume observed by the Polar satellite in the prenoon sector and the IMAGE satellite during the magnetic storm of 11 April 2001, *J. Geophys. Res.*, *112*, A06237, doi:10.1029/2006JA012030.

Kivelson, M. G., and C. T. Russell (1995), *Introduction to Space Physics*, Introduction to Space Physics, Edited by Margaret G. Kivelson and Christopher T. Russell, pp. 586. ISBN 0521451043. Cambridge, UK: Cambridge University Press, April 1995.

Laundal, K. M., and N. Østgaard (2009), Asymmetric auroral intensities in the Earth's Northern and Southern hemispheres, *Nature*, *460*, 491–493, doi:10.1038/nature08154.

Lee, S. H., H. Zhang, Q.-G. Zong, A. Otto, D. G. Sibeck, Y. Wang, K.-H. Glassmeier, P. W. Daly, and H. Rème (2014), Plasma and energetic particle behaviors during asymmetric magnetic reconnection at the magnetopause, *J. Geophys. Res.*, *119*, 1658–1672, doi:10.1002/2013JA019168.

Lee, S. H., H. Zhang, Q.-G. Zong, Y. Wang, A. Otto, H. Rème, and K.-H. Glassmeier (2015a), Asymmetric ionospheric outflow observed at the dayside magnetopause, *J. Geophys. Res.*, *120*(5), 3564–3573, doi:10.1002/2014JA020943, 2014JA020943.

Lee, S. H., H. Zhang, Q.-G. Zong, A. Otto, H. Rème, and E. Liebert (2015b), A Statistical Study of Plasmaspheric Plumes and Ionospheric Outflows Observed at the Dayside Magnetopause, *J. Geophys. Res.*

Lemaire, J. (2000), The formation plasmaspheric tails, *Physics and Chemistry of the Earth*, *25*, 9–17, doi:10.1016/S1464-1917(99)00026-4.

Lemaire, J., and R. W. Schunk (1992), Plasmaspheric wind, *J. Atmos. Terr. Phys.*, *54*, 467–477.

Lennartsson, O. W., H. L. Collin, and W. K. Peterson (2004), Solar wind control of Earth's H^+ and O^+ outflow rates in the 15-eV to 33-keV energy range, *J. Geophys. Res.*, *109*, A12212, doi:10.1029/2004JA010690.

Lennartsson, W., and D. L. Reasoner (1978), Low-energy plasma observations at synchronous orbit, *J. Geophys. Res.*, *83*, 2145–2156, doi:10.1029/JA083iA05p02145.

Li, K., et al. (2012), On the ionospheric source region of cold ion outflow, *Geophys. Res. Lett.*, *39*, L18102, doi:10.1029/2012GL053297.

Lin, R. P., et al. (2003), RHESSI Observations of Particle Acceleration and Energy Release in an Intense Solar Gamma-Ray Line Flare, *apjl*, *595*, doi:10.1086/378932.

Lindstedt, T., Y. V. Khotyaintsev, A. Vaivads, M. André, R. C. Fear, B. Lavraud, S. Haaland, and C. J. Owen (2009), Separatrix regions of magnetic reconnection at the magnetopause, *Ann. Geophys.*, *27*, 4039–4056, doi:10.5194/angeo-27-4039-2009.

Liou, K., P. T. Newell, and C.-I. Meng (2001), Seasonal effects on auroral particle acceleration and precipitation, *J. Geophys. Res.*, *106*, 5531–5542, doi:10.1029/1999JA000391.

Lockwood, M., J. H. Waite, Jr., T. E. Moore, J. F. E. Johnson, and C. R. Chappell (1985), A new source of suprathermal O^+ near the dayside polar cap boundary, *J. Geophys. Res.*, *90*, 4099–4116.

Love, J. J., and K. J. Remick (2007), Magnetic indices, in *Encyclopedia of Geomagnetism and Paleomagnetism*, edited by D. Gubbins and E. Herrero-Bervera, pp. 509–512, Springer Netherlands.

Lu, G., P. H. Reiff, J. L. Karty, M. R. Hairston, and R. A. Heelis (1989), Distribution of convection potential around the polar cap boundary as a function of the interplanetary magnetic field, *J. Geophys. Res.*, *94*, 13,447–13,461, doi:10.1029/JA094iA10p13447.

Lyons, L. R., and D. Williams (1984), *Quantitative Aspects of Magnetospheric Physics*, D. Reidel Publishing Company, Dordrecht.

Matsumoto, H., X. H. Deng, H. Kojima, and R. R. Anderson (2003), Observation of Electrostatic Solitary Waves associated with reconnection on the dayside magnetopause boundary, *Geophys. Res. Lett.*, *30*(6), 1326, doi:10.1029/2002GL016319.

McFadden, J. P., C. W. Carlson, D. Larson, J. Bonnell, F. S. Mozer, V. Angelopoulos, K.-H. Glassmeier, and U. Auster (2008), Structure of plasmaspheric plumes and their participation in magnetopause reconnection: First results from THEMIS, *Geophys. Res. Lett.*, *35*, L17S10, doi:10.1029/2008GL033677.

McPherron, R. L. (1979), Magnetospheric substorms, *Reviews of Geophysics and Space Physics*, *17*, 657–681, doi:10.1029/RG017i004p00657.

McPherron, R. L., and R. H. Manka (1985), Dynamics of the 1054 UT March 22, 1979, substorm event - CDAW 6, *J. Geophys. Res.*, *90*, 1175–1190, doi:10.1029/JA090iA02p01175.

Moldwin, M. B., B. R. Sandel, M. F. Thomsen, and R. C. Elphic (2003), Quantifying Global Plasmaspheric Images With in situ Observations, *Space Sci. Rev.*, *109*, 47–61, doi: 10.1023/B:SPAC.0000007512.69979.8f.

Moldwin, M. B., J. Howard, J. Sanny, J. D. Bocchicchio, H. K. Rassoul, and R. R. Anderson (2004), Plasmaspheric plumes: CRRES observations of enhanced density beyond the plasmapause, *J. Geophys. Res.*, *109*, A05,202, doi:10.1029/2003JA010320.

Moore, T. E. (1991), Origin of magnetospheric plasma, *U.S. Natl. Rep. Int. Union Geod. Geophys. 1987-1991, Rev. Geophys.*, *29*, 1039–1048.

Mozer, F. S., and P. Lucht (1974), The average auroral zone electric field, *J. Geophys. Res.*, *79*, 1001–1006, doi:10.1029/JA079i007p01001.

Mozer, F. S., and P. L. Pritchett (2009), Regions associated with electron physics in asymmetric magnetic field reconnection, *Geophys. Res. Lett.*, *36*, L07102, doi:10.1029/2009GL037463.

Mozer, F. S., S. Bale, and T. D. Phan (2002), Evidence of diffusion regions at a subsolar magnetopause crossing, *Phys. Rev. Lett.*, *89*, DOI: 10.1103/PhysRevLett.89.015,002.

Mozer, F. S., P. L. Pritchett, J. Bonnell, D. Sundkvist, and M. T. Chang (2008), Observations and simulations of asymmetric magnetic field reconnection, *J. Geophys. Res.*, *113*, A00C03, doi: 10.1029/2008JA013535.

Nagai, T., J. F. E. Johnson, and C. R. Chappell (1983), Low-energy (<100 eV) ion pitch angle distributions in the magnetosphere by ISEE 1, *J. Geophys. Res.*, *88*, 6944–6960, doi: 10.1029/JA088iA09p06944.

Newell, P. T., C.-I. Meng, and K. M. Lyons (1996), Suppression of discrete aurorae by sunlight, *Nature*, *381*, 766–767, doi:10.1038/381766a0.

O'Brien, T. P., and M. B. Moldwin (2003), Empirical plasmapause models from magnetic indices, *Geophys. Res. Lett.*, *30*, 1152, doi:10.1029/2002GL016007.

Øieroset, M., T. D. Phan, , M. Fujimoto, R. P. Lin, and R. P. Lepping (2001), In situ detection of collisionless reconnection in the Earth's magnetotail, *Nature*, *412*, 414–417.

Øieroset, M., R. P. Lin, T. D. Phan, D. E. Larson, and S. D. Bale (2002), Evidence for Electron Acceleration up to 300 keV in the Magnetic Reconnection Diffusion Region of Earth's Magnetotail, *Phys. Rev. Lett.*, *89*, doi:10.1103/PhysRevLett.89.195001.

Owen, C. J., et al. (2001), Cluster PEACE observations of electrons during magnetospheric flux transfer events, *Ann. Geophys.*, *19*, 1509–1522, doi:10.5194/angeo-19-1509-2001.

Parker, E. N. (1957), Newtonian development of the dynamical properties of ionized gases of low density, *Physical Rev.*, *107*, 924–933.

Parker, E. N. (1958), Dynamics of the Interplanetary Gas and Magnetic Fields., *Astrophys. J.*, *128*, 664C676.

Parks, G. K. (2004), *Physics of space plasmas : an introduction*, Physics of space plasmas : an introduction / George K Parks. Boulder, Colo. : Westview Press, Advanced Book Program, c2004.

Paschmann, G., et al. (1979), Plasma acceleration at the earth's magnetopause: Evidence for reconnection, *Nature*, *282*, 243–246.

Pedersen, A., et al. (2008), Electron density estimations derived from spacecraft potential measurements on Cluster in tenuous plasma regions, *J. Geophys. Res.*, *113*, A07S33, doi: 10.1029/2007JA012636.

Peterson, W. K., H. L. Collin, A. W. Yau, and O. W. Lennartsson (2001), Polar/Toroidal Imaging Mass-Angle Spectrograph observations of suprathermal ion outflow during solar minimum conditions, *J. Geophys. Res.*, *106*, 6059–6066, doi:10.1029/2000JA003006.

Peterson, W. K., H. L. Collin, O. W. Lennartsson, and A. W. Yau (2006), Quiet time solar illumination effects on the fluxes and characteristic energies of ionospheric outflow, *J. Geophys. Res.*, *111*, A11S05, doi:10.1029/2005JA011596.

Petschek, H. E. (1964), Magnetic Field Annihilation, in *The Physics of Solar Flares*, edited by W. N. Hess, p. 425.

Priest, E., and T. Forbes (2000), *Magnetic Reconnection*, Magnetic Reconnection, by Eric Priest and Terry Forbes, pp. 612. ISBN 0521481791. Cambridge, UK: Cambridge University Press, June 2000.

Pritchett, P. L., and F. S. Mozer (2009), Asymmetric magnetic reconnection in the presence of a guide field, *J. Geophys. Res.*, *114*, A11210, doi:10.1029/2009JA014343.

Raitt, W. J., R. W. Schunk, and P. M. Banks (1977), The influence of convection electric fields on thermal proton outflow from the ionosphere, *Planet. Space Sci.*, *25*, 291–301, doi:10.1016/0032-0633(77)90139-8.

Redmon, R. J., W. K. Peterson, L. Andersson, and P. G. Richards (2012), Dawnward shift of the dayside O^+ outflow distribution: The importance of field line history in O^+ escape from the ionosphere, *J. Geophys. Res.*, *117*, A12222, doi:10.1029/2012JA018145.

Reiff, P. H., and J. L. Burch (1985), Imf by-dependent plasma flow and birkeland currents in the dayside magnetosphere: 2. a global model for northward and southward imf, *Journal of Geophysical Research (Space Physics)*, *90*(A2), 1595–1609, doi:10.1029/JA090iA02p01595.

Rème, H., et al. (2001), First multispacecraft ion measurements in and near the earth's magnetosphere with the identical cluster ion spectrometry (CIS) experiment, *Ann. Geophys.*, *19*, 1303–1354.

Retinò, A., et al. (2006), Structure of the separatrix region close to a magnetic reconnection X-line: Cluster observations, *Geophys. Res. Lett.*, *33*, L06101, doi:10.1029/2005GL024650.

Retinò, A., D. Sundkvist, A. Vaivads, F. Mozer, M. André, and C. J. Owen (2007), In situ evidence of magnetic reconnection in turbulent plasma, *Nature Physics*, *3*, 236–238, doi:10.1038/nphys574.

Rich, F. J., and M. Hairston (1994), Large-scale convection patterns observed by DMSP, *J. Geophys. Res.*, *99*, 3827–3844, doi:10.1029/93JA03296.

Ridley, A. J., G. Lu, C. R. Clauer, and V. O. Papitashvili (1998), A statistical study of the ionospheric convection response to changing interplanetary magnetic field conditions using the assimilative mapping of ionospheric electrodynamics technique, *J. Geophys. Res.*, *103*, 4023–4040, doi:10.1029/97JA03328.

Robert, P., M. W. Dunlop, A. Roux, and G. Chanteur (1998), Accuracy of current determination, in *Analysis Methods for Multi Spacecraft Data*, edited by G. Paschmann and P. W. Daly, p. 395, ESA, Bern, Switzerland.

Rosenbauer, H., H. Gruenwaldt, M. D. Montgomery, G. Paschmann, and N. Skopke (1975), HEOS 2 plasma observations in the distant polar magnetosphere: the plasma mantle, *J. Geophys. Res.*, *80*, 2723–2737.

Rostoker, G., S.-I. Akasofu, J. Foster, R. A. Greenwald, A. T. Y. Lui, Y. Kamide, K. Kawasaki, R. L. McPherron, and C. T. Russell (1980), Magnetospheric substorms - Definition and signatures, *J. Geophys. Res.*, *85*, 1663–1668, doi:10.1029/JA085iA04p01663.

Russell, C. T., and R. C. Elphic (1978), Initial ISEE magnetometer results: Magnetopause observations, *Space Sci. Rev.*, *22*, 681–715.

Russell, C. T., and R. C. Elphic (1979), Observation of magnetic flux ropes in the Venus ionosphere, *Nature*, *279*, 616–618.

Sagawa, E., A. W. Yau, B. A. Whalen, and W. K. Peterson (1987), Pitch angle distributions of low-energy ions in the near-earth magnetosphere, *J. Geophys. Res.*, *92*, 12,241–12,254, doi: 10.1029/JA092iA11p12241.

Sandel, B. R., J. Goldstein, D. L. Gallagher, and M. Spasojevic (2003), Extreme Ultraviolet Imager Observations of the Structure and Dynamics of the Plasmasphere, *Space Sci. Rev.*, *109*, 25–46, doi:10.1023/B:SPAC.0000007511.47727.5b.

Sauvaud, J.-A., et al. (2001), Intermittent thermal plasma acceleration linked to sporadic motions of the magnetopause, first Cluster results, *Ann. Geophys.*, *19*, 1523, doi:10.5194/angeo-19-1523-2001.

Schwartz, S. J. (1998), Shock and Discontinuity Normals, Mach Numbers, and Related Parameters, *ISSI Scientific Reports Series*, *1*, 249–270.

Shay, M. A., J. F. Drake, B. N. Rogers, and R. E. Denton (1999), The scaling of collisionless, magnetic reconnection for large systems, *Geophys. Res. Lett.*, *26*, 2163–2166.

Sheeley, B. W., M. B. Moldwin, H. K. Rassoul, and R. R. Anderson (2001), An empirical plasmasphere and trough density model: CRRES observations, *J. Geophys. Res.*, *106*, 25,631–25,642, doi:10.1029/2000JA000286.

Sibeck, D. G., et al. (1999), Plasma transfer processes at the magnetopause, in *Magnetospheric Plasma Sources and Losses*, edited by B. Hultqvist and M. Øieroset, pp. 207–283, Kluwer Acade., Norwell, Mass.

Sonnerup, B. U. Ö., and D.-J. Wang (1987), Structure of reconnection boundary layers in incompressible mhd, *J. Geophys. Res.*, *92*, 8621–8633.

Sonnerup, B. U. Ö., G. Paschmann, I. Papamastorkis, N. Sckopke, G. Haerendel, S. J. Bame, J. R. Asbridge, J. T. Gosling, and C. T. Russell (1981), Evidence for magnetic field reconnection at the earth's magnetopause, *J. Geophys. Res.*, *86*, 10,049–10,067.

Sonnerup, B. U. Ö., I. Papamastorakis, G. Paschmann, and H. Lühr (1987), Magnetopause properties from AMPTE/IRM observations of the convection electric field: Method development, *J. Geophys. Res.*, *92*, 12,137–12,159.

Sonnerup, B. U. O., I. Papamastorakis, G. Paschmann, and H. Luehr (1990), The magnetopause for large magnetic shear - Analysis of convection electric fields from AMPTE/IRM, *J. Geophys. Res.*, *95*, 10,541–10,557.

Speiser, T. W., D. J. williams, and H. A. Garcia (1981), Magnetospherically trapped ions as a source of magnetosheath energetic ions, *J. Geophys. Res.*, *86*, 723–732.

Strangeway, R. J., R. E. Ergun, Y.-J. Su, C. W. Carlson, and R. C. Elphic (2005), Factors controlling ionospheric outflows as observed at intermediate altitudes, *J. Geophys. Res.*, *110*, A03221, doi:10.1029/2004JA010829.

Su, Y.-J., J. E. Borovsky, M. F. Thomsen, R. C. Elphic, and D. J. McComas (2000), Plasmaspheric material at the reconnecting magnetopause, *J. Geophys. Res.*, *105*, 7591–7600, doi: 10.1029/1999JA000266.

Sweet, P. A. (1958), The neutral point theory of solar flares, in *Electromagnetic Phenomena in Cosmical Pysics*, edited by B. Lehnert, pp. 123–134, Cambridge Univeristy Press, New York.

Vaivads, A., A. Retinò, Y. V. Khotyaintsev, and M. André (2010), The Alfvén edge in asymmetric reconnection, *Ann. Geophys.*, *28*, 1327–1331, doi:10.5194/angeo-28-1327-2010.

Volwerk, M. (2006), Multi-Satellite Observations of ULF Waves, in *Magnetospheric ULF Waves – Synthesis and New Directions*, edited by K. Takahashi, P. J. Chi, R. E. Denton, and R. L. Lysak, pp. 109–135, AGU, AGU, Washington, D.C.

Wahlund, J.-E., H. J. Opgenoorth, I. Häggström, K. J. Winser, and G. O. L. Jones (1992), EISCAT observations of topside ionospheric ion outflows during auroral activity: Revisited, *J. Geophys. Res.*, *97*, 3019–3037.

Walén, C. (1944), On the Theory of Sunspots, *Arkiv for Astronomi*, *30*, 1–87.

Walsh, B. M., D. G. Sibeck, Y. Nishimura, and V. Angelopoulos (2013), Statistical analysis of the plasmaspheric plume at the magnetopause, *J. Geophys. Res.*, *118*, 4844–4851, doi: 10.1002/jgra.50458.

Walsh, B. M., J. C. Foster, P. J. Erickson, and D. G. Sibeck (2014), Simultaneous Ground- and Space-Based Observations of the Plasmaspheric Plume and Reconnection, *Science*, *343*, 1122–1125, doi:10.1126/science.1247212.

Weimer, D. R., J. R. Kan, and S.-I. Akasofu (1992), Variations of the polar cap potential measured during magnetospheric substorms, *J. Geophys. Res.*, *97*, 3945–3951, doi:10.1029/91JA03159.

Wilken, B., et al. (2001), First results from the rapid imaging energetic particle spectrometer on board cluster, *Ann. Geophys.*, *19*, 1355–1366.

Xiao, C. J., et al. (2007), A Cluster measurement of fast magnetic reconnection in the magnetotail, *Geophys. Res. Lett.*, *34*, L01101, doi:10.1029/2006GL028006.

Yau, A. W., and M. André (1997), Sources of ion outflow in the high latitude ionosphere, *Space Sci. Rev.*, *80*, 1–25.

Yau, A. W., P. H. Beckwith, W. K. Peterson, and E. G. Shelley (1985), Long-term (solar cycle) and seasonal variations of upflowing ionospheric ion events at DE-1 altitudes, *J. Geophys. Res.*, *90*, 6395–6407.

Yau, A. W., E. G. Shelley, and W. K. Peterson (1986), Accelerated auroral and polar-cap ions : Outflow at DE-1 altitudes, *Washington DC American Geophysical Union Geophysical Monograph Series*, *38*, 72–76, doi:10.1029/GM038p0072.

Yau, A. W., T. Abe, and W. K. Peterson (2007), The polar wind: Recent observations, *J. Atmos. Terr. Phys.*, *69*, 1936–1983, doi:10.1016/j.jastp.2007.08.010.

Zhang, H., Q.-G. Zong, T. A. Fritz, S. Y. Fu, S. Schaefer, K. H. Glassmeier, P. W. Daly, H. Rème, and A. Balogh (2008), Cluster observations of collisionless Hall reconnection at high-latitude magnetopause, *J. Geophys. Res.*, *113*, A03204, doi:10.1029/2007JA012769.

Zheng, Y., T. E. Moore, F. S. Mozer, C. T. Russell, and R. J. Strangeway (2005), Polar study of ionospheric ion outflow versus energy input, *J. Geophys. Res.*, *110*, A07210, doi: 10.1029/2004JA010995.

Zhou, X. W., C. T. Russell, G. Le, S. A. Fuselier, and J. D. Scudder (2000), Solar wind control of the polar cusp at high-altitude, *J. Geophys. Res.*, *105*, 245–251.

Zong, Q.-G., and B. Wilken (1998), Layered structure of energetic oxygen ions in the magnetosheath, *Geophys. Res. Lett.*, *25*, 4121–4124.

Zong, Q.-G., and B. Wilken (1999), Bursty energetic oxygen events in dayside magnetosheath: Geotail observation, *Geophys. Res. Lett.*, *26*, 3349–3352.

Zong, Q.-G., B. Wilken, S.-Y. Fu, T. A. Fritz, Z.-Y. Pu, N. Hasebe, and D. J. Williams (2001), Ring current oxygen ions in the magnetosheath caused by magnetic storm, *J. Geophys. Res.*, *106*, 25,541–25,556.

Appendix
Coordinate System

Many different coordinate systems are used in space physics such as satellite trajectories, boundary locations, and plasma-field measurements. The transformation from one or anther of the coordinate systems is necessary to easily calculate and understand the various physical processes and to better order the experimental data. The transformation can be derived by using the trigonometric relations between angles measured in each coordinate system by means of the spherical trigonometry method.

The Geocentric Solar Ecliptic (GSE) System is is defined that the x-axis is pointing from the earth toward the sun, the y-axis lies in the ecliptic plane pointing toward dusk (opposing the Earth's motion). Its z-axis completes the right-hand rule ($z = x \times y$) which is parallel to the ecliptic north pole. The ecliptic plane is coplanar with both the orbit of the Earth around the Sun and the orbit of the Sun around the Earth, which is an apparent annual path of the Sun on the celestial sphere. The origin of the system is at the center of the Earth. This system rotates about the z axis in one year relative to an inertial system. The GSE coordinate is used to better display the solar wind data since the aberration of the solar wind data caused by the Earth's orbital motion can easily be removed in this system.

The Geocentric Solar Magnetic (GSM) System x-axis is directed towards the Sun, which is the same sense as the GSE system, the y-axis is chosen to be perpendicular to the Earth's magnetic dipole, and the positive z-axis is parallel to the northern magnetic pole. The GSM system can be transformed from GSE by rotating about the x-axis (Figure A.1). The GSM conversion can be described in terms of the rotation angle (ψ) in degree. The GSM z axis is towards the positive y (dusk side) in the GSE system when the rotation angle is positive.

$$\begin{pmatrix} x \\ y \\ z \end{pmatrix}_{GSM} = \begin{pmatrix} 1 & 0 & 0 \\ 0 & cos\psi & -sin\psi \\ 0 & sin\psi & cos\psi \end{pmatrix} \cdot \begin{pmatrix} x \\ y \\ z \end{pmatrix}_{GSE} \tag{9.1}$$

In addition to the annual rotation, there is a diurnal variation of the GSM coordinates since the rotation axis and magnetic dipole axis are offset. At the solstices the rotational axis is in the $x - z_{GSE}$ plane so that the component of the rotational axis perpendicular to x_{GSE} (sunward) is identical to the z_{GSE} (normal to the ecliptic). This occurs only twice a day during this time period because the magnetic north dipole has a diurnal variation (11°). At the equinoxes the rotational axis is perpendicular to the x_{GSE} and deviates by 23° from the z_{GSE}. Therefore the maximum deviation between GSM and GSE is a rotation of about 34° in the $y - z$ plane and occurs at

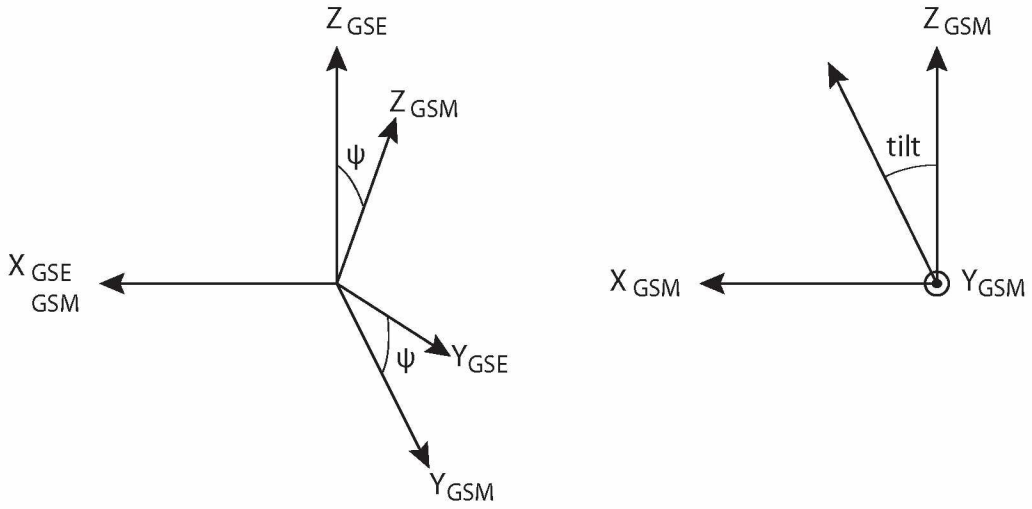

Figure 9.1. The GSM conversion from the GSE in terms of the rotational angle (ψ) and the dipole tilt angle.

once during the day at the equinoxes. The GSM coordinate is useful for displaying the boundary locations (magnetopause and shock-boundary position), magnetic fields in the magnetosheath and magnetotail, and the flow velocities in the magnetosheath, since the magnetic dipole axis changes depending on the solar wind flow. The dipole tilt angle (Figure A.1) indicates the inclination of the north magnetic pole towards the Sun from the GSM z-axis and is positive.